

A WAVEGUIDE-BASED LENS-LESS X-RAY MICROSCOPE

DISSERTATION

zur Erlangung des Doktorgrades
der Mathematisch-Naturwissenschaftlichen Fakultäten
der Georg-August-Universität zu Göttingen

vorgelegt von

CHRISTOPH GERMAN JOSEF OLLINGER

aus Dillingen (Saar)

Göttingen 2006

D7

Referent: Prof. Dr Tim Salditt

Koreferent: Prof. Dr. Werner Lauterborn

Tag der mündlichen Prüfung: 11. Juli 2006

CONTENTS

Contents

Introduction	9
1 Theory of waveguide based imaging	11
1.1 X-ray waveguides	11
1.1.1 Helmholtz equation	12
1.1.2 Parabolic wave equation	15
1.2 Scalar diffraction theory	17
1.3 The phase problem and phase retrieval	19
1.3.1 Hybrid Input-Output Algorithm	20
1.3.2 Holography	23
2 Waveguide and sample fabrication	29
2.1 Waveguide fabrication	29
2.1.1 Thin film spincoating	29
2.1.2 Electron beam lithography	31
2.1.3 Focussed ion beam	32
2.2 Sample fabrication	33
3 A mobile and modular waveguide imaging setup	37
3.1 General considerations	37
3.2 Positioning System	39
3.2.1 Positioning Control system	39
3.2.2 Positioning tables	40
3.2.3 Accuracy, precision, trueness and stability	43
3.3 Hard x-ray photon detection	48
3.3.1 Two dimensional detection	48
3.3.2 Energy dispersive detection	52
3.3.3 Point detection	57

3.4	Implementation	58
3.4.1	Computer network	58
3.4.2	CCD - Motor synchronization	59
3.4.3	SDD implementation	60
3.5	In-House setup	61
4	Experiments	63
4.1	General beamline layout	63
4.2	Considerations for alignment	68
4.2.1	Pivot-point	68
4.2.2	Waveguide preparation	69
4.2.3	Waveguide choice	69
4.3	Hard x-ray beam compression to nanometer size	72
4.4	Hard x-ray waveguide scanning fluorescence	78
4.5	Hard X-ray in-line holography	83
4.6	Hard X-ray reference beam holography	87
4.6.1	Waveguide design	87
4.6.2	Experiment	88
4.7	Object localization with 10nm accuracy by x-ray in-line holographic imaging	90
4.7.1	Simulation	92
4.8	Conclusions	97
	Summary	99
A	MoWaSt implementation	101
A.1	CCD client-server application	101
A.1.1	Server application	101
A.1.2	Client SPEC macro	106
A.2	Roentec implementation	117
B	Implementation of the Hybrid-Input-Output algorithm	133
C	Simulation of the holograms of point scatterers	141
	Bibliography	153
	Acknowledgements	157
	List of Publications	161

Curriculum Vitae 165

CONTENTS

Introduction

A lot of effort is currently invested to realize phase contrast imaging with hard x-rays. For specimen consisting of light elements, e.g. biological samples, the induced phase shift of the x-ray wave is much higher than the absorption. Thus, phase sensitive x-ray imaging methods could pave the way for enhanced contrast and resolution. Making use of the coherence properties of third generation synchrotron sources, applications like Fourier transform holography [ELS⁺04] and iterative reconstruction methods [MCKS99, WPVR03] become possible. These techniques allow to obtain a phase image of the object with a resolution in the nanometer range and without any a-priori knowledge on the sample, as is the case for classical x-ray diffraction. Except for experimental problems, convergence and uniqueness of these algorithms are in discussion. X-ray microscopy [SJe02] using Fresnel zone plates [CBL⁺05], mainly in the soft x-ray regime, and compound refractive lenses [SKP⁺05] for higher energy x-rays allow to image samples directly, i.e. without the need of image reconstruction. The quality of these focusing lenses is poor compared to visible light, since the refractive index in the x-ray range is close to unity. Thus the resolution in x-ray microscopy is far from the wavelength limit.

X-ray waveguides consist of a guiding core embedded in a cladding material with adequate refractive index [SS73]. Upon shining an x-ray beam onto the guiding channel, a discrete number of modes propagate in the waveguide, leading to a nanometer-sized, slightly divergent and highly coherent x-ray beam [PDB⁺02]. Provided, that the intensity in the waveguided beam is sufficient, imaging experiments become possible [LCC⁺97b]. Using the small beam dimensions behind the guide, scanning fluorescence experiments with a resolution comparable to the size of the guiding core can be performed. Using illumination by waveguides it becomes possible to adapt in-line holography [Gab48] as well as reference beam holography [LU62] to the hard x-ray wavelength range ($\lambda \approx 1 \text{ \AA}$).

The aim of this thesis is i) to fabricate and characterize two dimensionally con-

fining hard x-ray waveguides and test-samples, meeting the demands for imaging, ii) to provide the instrumental and experimental prerequisites to allow for scanning fluorescence and holographic imaging with one setup and iii) to realize these imaging techniques using x-ray waveguides in proof-of-principle experiments.

In the first chapter of this thesis, a brief overview is given over the theoretical background of waveguide based imaging. Starting from the properties of x-ray wave propagation in a two dimensionally confining waveguide, further propagation is described by means of scalar diffraction theory. The phase problem is described as well as possibilities to overcome its limitations. Here, the hybrid-input-output algorithm, a method to reconstruct the phase information from coherent diffraction data, and the holographic illumination and reconstruction methods used in waveguide based imaging are presented.

The second chapter presents on the fabrication of two dimensionally confining x-ray waveguides and the samples used in this thesis. A brief description of the fabrication techniques is given, including thin film spin-coating, electron beam lithography, focused ion beam milling and lift-off procedures to produce these waveguides and samples.

Chapter three presents the description of the instrumental efforts, which were made to realize waveguide based lens-less imaging. Starting from a general description of the requirements for the instrument, the design and setup of the motorized stages is described. It is followed by a description of different detection schemes. In the end of the chapter, details on the implementation of the hardware are given.

In the last chapter the experiments performed with the build instrument are described. Starting from the first experiment with the instrument, where two dimensional beam confinement with an x-ray waveguide and sufficient flux in the far-field was achieved. This instrumentation enables to perform imaging experiments using the waveguided beam, in particular: Waveguide based scanning x-ray fluorescence and in-line holography. In the first case a resolution in the sub-100nm range was achieved, were as in the second case the reconstructed images are slightly blurred by the presence of a twin image. X-ray reference beam holography experiments, overcome the twin image restrictions and demonstrating a resolution on the order of the waveguide diameter were thus performed. Finally the localization accuracy of an object in the waveguided beam on the order of 10nm is demonstrated.

Chapter 1

Theory of waveguide based imaging

In this chapter a mathematical description of hard x-ray waveguiding is given. Different schemes of coupling an x-ray beam into a waveguide optic have been studied in recent years [PDB⁺02, LCC⁺97b]. Here we focus on the front coupling scheme, which is used in this thesis. Two different approaches of making use of coherent x-rays to overcome the phase problem of x-ray scattering are discussed. First the so-called oversampling method is described, where a non-periodic object is illuminated by a coherent x-ray beam and an iterative algorithm is used to reconstruct the real space image of an object. In the last section of this chapter image formation through holographic projection is discussed, as well as reconstruction of the respective real space images.

1.1 X-ray waveguides

Hard x-ray waveguides are a key device to produce coherent x-ray nano-beams. Because of their wave propagation properties the incoming x-rays are 'filtered', such that highly coherent and slightly divergent radiation is transmitted. A coherent illumination of an object is achieved. X-ray waveguides were first described by Spiller and Segmüller 1973 [SS73] for the case of one dimensional beam confinement. In 2002 Pfeiffer et. al. demonstrated two dimensional x-ray beam confinement [PDB⁺02]. In this thesis only two dimensionally confining waveguides are used. The optical properties of these x-ray waveguides are described in the following section.

1.1.1 Helmholtz equation

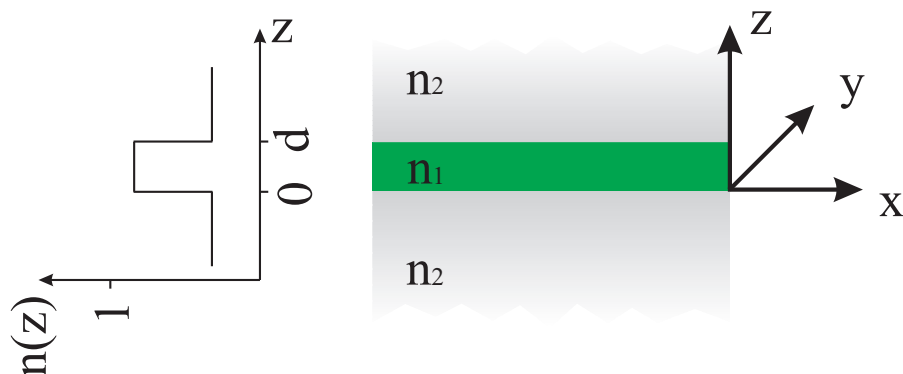


Figure 1.1: Sketch of a front coupling waveguide. The guiding layer with refractive index n_1 is surrounded by a cladding layer with refractive index n_2 .

Let us assume a structure as sketched in Figure 1.1: A material with a refractive index n_1 and thickness d is surrounded by a (semi-infinite thick) material with refractive index n_2 . To describe the propagation of a plane wave impinging onto the layered structure, we start from the Maxwell's equations (in a nonconducting medium and in absence of currents):

$$\nabla \times \mathbf{H} = \varepsilon_0 n^2 \frac{\partial \mathbf{E}}{\partial t} \quad (1.1)$$

and

$$\nabla \times \mathbf{E} = -\mu_0 \frac{\partial \mathbf{H}}{\partial t} \quad (1.2)$$

with the dielectric permittivity of vacuum ($\varepsilon_0 = 8.85 \cdot 10^{-12} \text{As/Vm}$), the magnetic permeability of vacuum $\mu_0 = 12.57 \cdot 10^{-7} \text{Vs/Am}$, the refractive index n and the electric \mathbf{E} and magnetic field \mathbf{H} respectively. From the Maxwell's equations (equations 1.1 and 1.2), with the speed of light $c = 2.99 \times 10^8 \text{m/s}$, the wave equation for the electric field can be written as:

$$\nabla^2 \mathbf{E} - \frac{n^2}{c^2} \frac{\partial^2 \mathbf{E}}{\partial t^2} = 0 \quad (1.3)$$

For further treatment we will discuss the one dimensionally confined case, i.e. the case without variation of n in y -direction. For linearly polarized light and omitting the time dependence $e^{i\omega t}$, Equation 1.3 can then be transformed into the *Helmholtz equation*:

$$\frac{\partial^2 E_y}{\partial z^2} + (n^2 k^2 - \beta^2) E_y = 0 \quad (1.4)$$

Here, β is the projection of the wavevector of the incident plane wave onto the x -direction, also known as propagation constant. With the ansatz

$$E_y(z) = \begin{cases} Ae^{\gamma z} & \text{for } z < 0 \\ B \cos(\kappa z) + C \sin(\kappa z) & \text{for } 0 \leq z \leq d \\ De^{-\gamma(z-d)} & \text{for } d < z \end{cases} \quad (1.5)$$

where $\gamma^2 = \beta^2 - n_2^2 k^2$ and $\kappa^2 = n_1^2 k^2 - \beta^2$, we find solutions for equation 1.4 if the transcendental eigenvalue equation

$$\tan(\kappa d) = \frac{2\kappa\gamma}{\underbrace{\kappa^2 - \gamma^2}_{=: \Gamma(\kappa d)}} \quad (1.6)$$

is fulfilled. This is only the case for a discrete number of supported modes, which can be visualized by plotting the left and right side of equation 1.6 (see figure 1.2). The intersections of $\tan(\kappa d)$ and $\Gamma(\kappa d)$ are limited since $\Gamma(\kappa d)$ get imaginary for $V := (n_1^2 - n_2^2)^{1/2} kd = \kappa d$. The number of supported modes N is then given by $N = V/\pi|_{int}$, where $|_{int}$ denotes the next integer lager than V/π [YPV95].

As example (fig. 1.2) a guiding layer with $d = 50nm$ and a refractive index $n_1 = 1 - 0.5 \cdot 10^{-5}$ is sandwiched between two layers with refractive index $n_2 = 1 - 1 \cdot 10^{-5}$. Equation 1.6 is plotted for a wavelength of 1\AA . Except for the ground mode, the equation is fulfilled for three more sets of parameters κ and γ . In this example the waveguide then supports four modes. The field distribution for these four modes can be plotted by using the parameter sets for κ and γ with equation 1.5. For the example discussed above the field distribution is shown in figure 1.2.

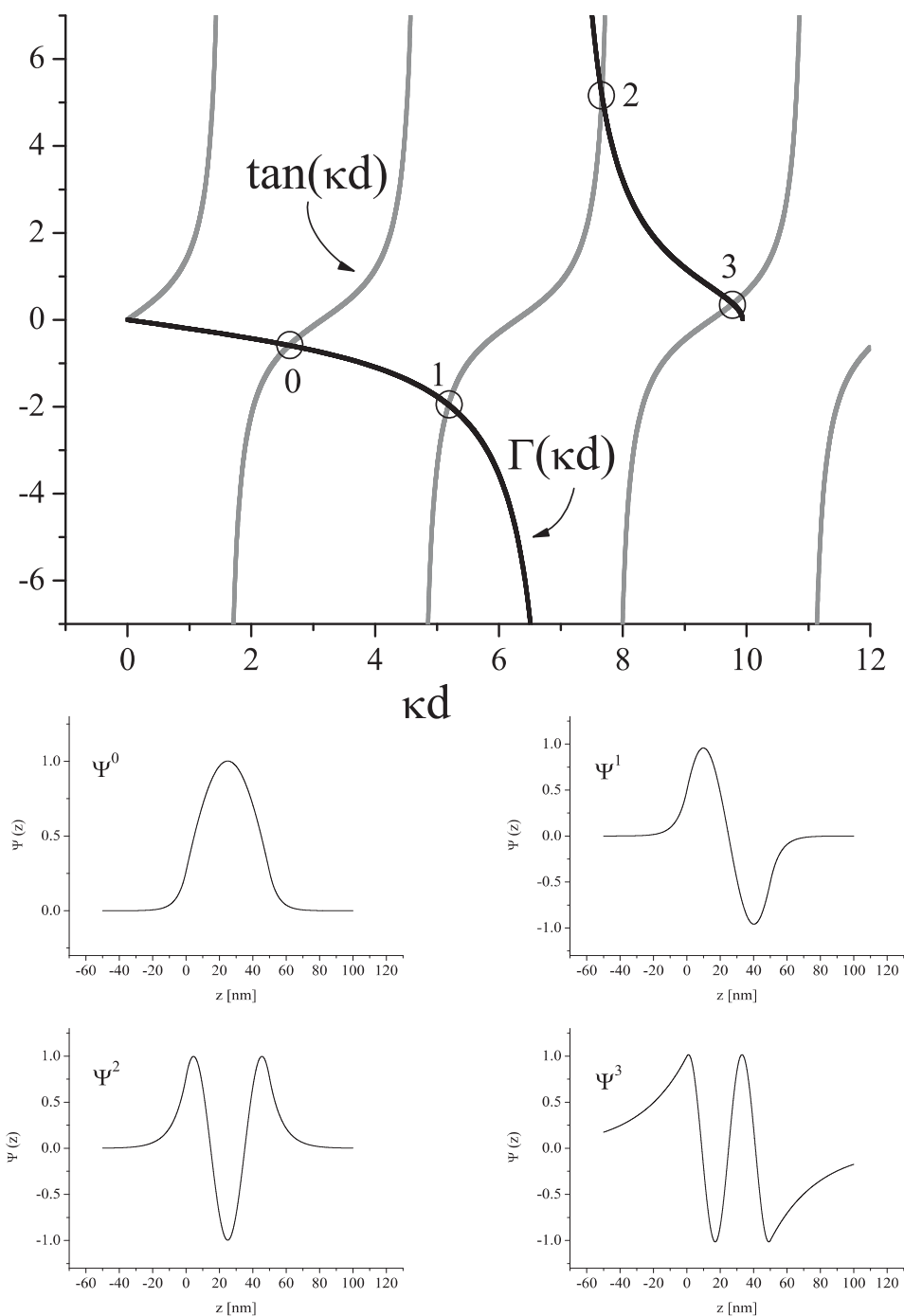


Figure 1.2: **top** Intersections of $\tan(\kappa d)$ and $\Gamma(\kappa d)$ are solutions of the transcendental eigenvalue equation (1.6) as calculated for a 50 nm thick waveguide layer with refractive index $n_1 = 1 - 0.5 \cdot 10^{-5}$ and a cladding with $n_2 = 1 - 1 \cdot 10^{-5}$. **bottom** Calculated normalized internal field distribution Ψ^j of a planar waveguide (refractive indices $n_1 = 1 - 0.5 \cdot 10^{-5}$ and $n_2 = 1 - 1 \cdot 10^{-5}$) for the four supported modes ($j \in [0, 1, 2, 3]$).

1.1.2 Parabolic wave equation

The Helmholtz equation, as given in equation 1.4, describes the wave propagation in an x-ray waveguide for the case of an one dimensionally confining guide. In case of two dimensional confinement, the Helmholtz equation cannot be solved analytically for every geometry [Mar74]. To calculate the field amplitude inside the waveguide the Helmholtz equation can be approximated by the parabolic wave equation. As is shown below, this equation can be used to simulate the internal field distribution numerically.

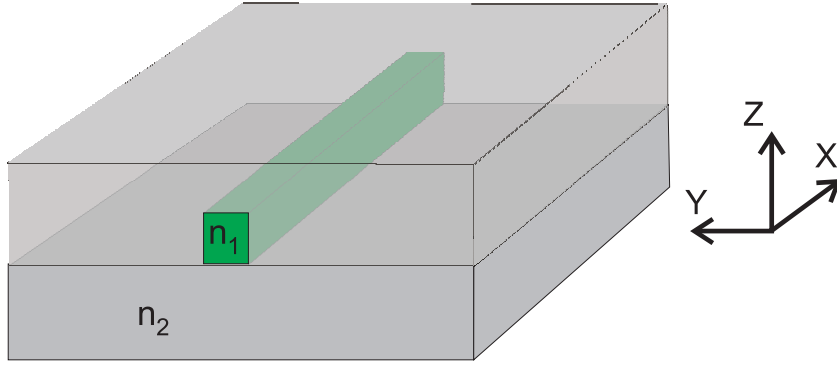


Figure 1.3: Sketch of a two dimensional confined waveguide. The guiding layer with refractive index n_1 is surrounded by a cladding layer with refractive index n_2 .

Assuming a plane wave ψ with wavevector \mathbf{k} incident onto a waveguide in x -direction, ψ oscillates fast in x and can be written as

$$\psi(x, y, z) = u(x, y, z) \exp(-ikx). \quad (1.7)$$

Thus the field is a superposition of a plane wave propagating in x direction and a waveguide modulated field $u(x, y, z)$ oscillating much slower in x direction than ψ . Inserting equation 1.7 in the Helmholtz equation for the two dimensionally confined case and neglecting the second order derivative of u leads to

$$-2ik \frac{\partial u}{\partial x} + \left(\frac{\partial^2}{\partial y^2} + \frac{\partial^2}{\partial z^2} \right) u + k^2(n^2 - 1)u = 0 \quad (1.8)$$

the parabolic wave equation [YPV95]. This allows to calculate the field amplitude distribution inside the waveguide. Applying a finite-differences algorithm

to the parabolic wave equation, the field inside the waveguides can be displayed [Fuh06, FS06].

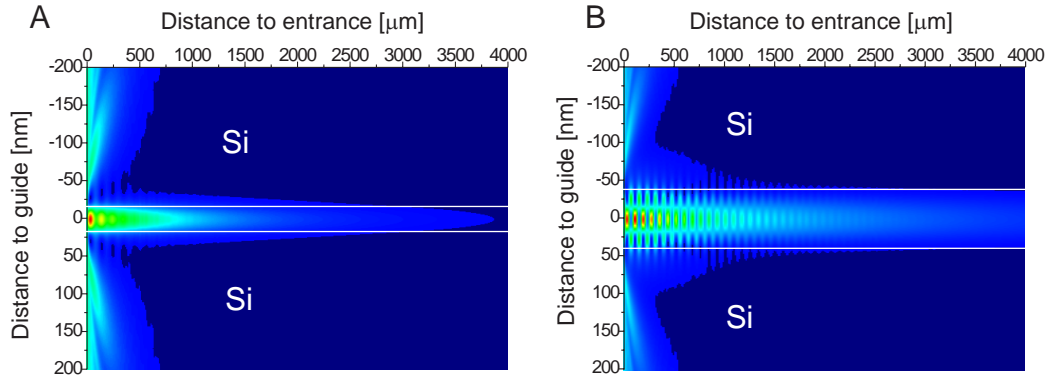


Figure 1.4: Comparison of the field intensity distribution inside a planar waveguide. The x-ray energy was set to 10.4keV, cladding material is silicon and the guiding core is made of the organic resist calixarene. In the left simulation the guiding core has a thickness of 30nm leading to the propagation of only a single mode. In the simulation of the right the guiding core is 70nm thick leading to the propagation of multiple modes.

In figure 1.4 the field distribution inside a waveguide structure is simulated for two different cases. In 1.4 **A** the guiding layer (thickness 30nm) made of calixarene (see also chapter 2) is confined between layers of silicon. A plane wave with an energy of $E = 10.4keV$ incidents onto the structure. In this case the waveguide only supports a single mode. In 1.4 **B**, the same waveguide structure is shown with a 70nm thick guiding layer. This geometry supports the propagation of up to four modes. Since a plane wave incidents onto the front side of the waveguide, only odd numbered modes are illuminated [BDD⁺02] and superpose coherently inside the guide.

1.2 Scalar diffraction theory

As has been shown above, it is possible to calculate field distributions inside an x-ray waveguide. Practically it is not possible to measure these field distributions directly, but one can deduce them from the intensity pattern detected far behind the waveguide. The propagation of x-rays downstream the waveguide exit is described by scalar diffraction theory [LK03].

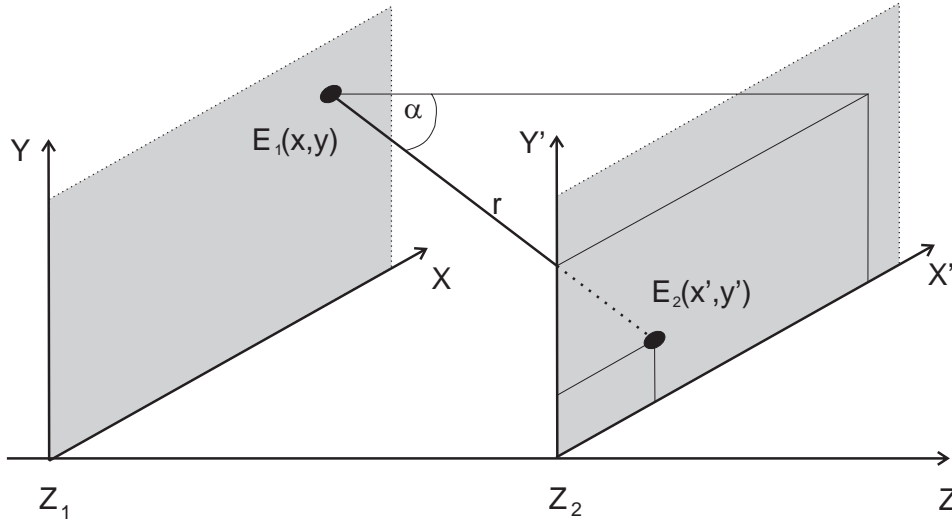


Figure 1.5: Sketch showing the geometry used in equation 1.9.

Assuming a given electric field $E_1(x, y)$ in a plane at position z_1 , the electric field further downstream can be described by the Huygens' principle, where each point in the plane at position z_1 is the source of a spherical wave. Thus the electric field $E_2(x', y')$ is a superposition of spherical waves originating from the plane at a distance $z := z_2 - z_1$ and modulated by the initial field distribution E_1 (see figure 1.5). This is described by the Fresnel-Kirchhoff-integral:

$$E_2(x', y') = \frac{1}{i\lambda} \int_{-\infty}^{+\infty} \int_{-\infty}^{+\infty} E_1(x, y) \frac{\exp(ikr)}{r} \cos(\alpha) dx dy \quad (1.9)$$

Fresnel approximation

Since the Fresnel-Kirchhoff-integral is not solvable for arbitrary $E_1(x, y)$ and thus a little unwieldy [LK03], approximations are helpful. In our case α is on the order of a few milliradians and thus $\cos(\alpha) \approx 1$ and $\frac{1}{r} \approx \frac{1}{z}$. Also, for $x, y \ll z_2 - z_1$, r in the exponent can be approximated:

$$\begin{aligned}
 r &= \sqrt{(x' - x)^2 + (y' - y)^2 + (z_2 - z_1)^2} \\
 &\approx z + \frac{(x' - x)^2}{2z} + \frac{(y' - y)^2}{2z} \quad \text{with } z := z_2 - z_1.
 \end{aligned} \tag{1.10}$$

The diffraction integral 1.9 can then be written in the so-called Fresnel approximation:

$$E_2(x', y') = \frac{\exp(ikz)}{i\lambda z} \int E_1(x, y) \exp\left(\frac{ik}{2z}[(x' - x)^2 + (y' - y)^2]\right) dx dy. \tag{1.11}$$

By defining the propagation kernel

$$h(x' - x, y' - y) = \frac{\exp(ikz)}{i\lambda z} \exp\left(\frac{ik}{2z}[(x' - x)^2 + (y' - y)^2]\right) \tag{1.12}$$

and making use of the fact, that a convolution in real space corresponds to a multiplication in Fourier space (convolution theorem), one is left with

$$\tilde{E}_2 = \tilde{h} \times \tilde{E}_1. \tag{1.13}$$

Here \tilde{E} and \tilde{h} denote the Fourier transform of E and h respectively. While a straight forward calculation of the Fresnel-Kirchhoff-integral would require time consuming calculations, making use of equation 1.13 can significantly reduce calculation time. For a typical pixel array (1024×1024 pixels) the propagation can thus be performed on a standard desktop computer within a few seconds.

Transmission function

As described e.g. in [Wei02, ANM00], the interaction of a wave with an object can be described using the distribution of the complex refractive index

$$n(x, y, z) = 1 - \delta(x, y, z) + i\beta(x, y, z). \tag{1.14}$$

The real part δ is responsible for the phase shift of the wave in the object, while the imaginary part β gives rise to absorption. Its distribution in the object is a consequence of the electron density distribution $\rho(x, y, z)$ in the object [ANM00]. Is a wave incident on an object of thickness ϵ , then

$$E(x, y, z) = \tau(x, y) \times E(x, y, z - \epsilon), \tag{1.15}$$

with

$$\tau(x, y) = \exp \left[-k \int_{z-\epsilon}^z i\delta(x, y, z) + \beta(x, y, z) dz \right]. \quad (1.16)$$

Combining equation 1.13 and equation 1.15, it is possible to calculate the field distribution behind an object illuminated by a plane wave, or vice versa, when calculating τ from the field distribution behind the object. This is in particular used for reconstructing the object transmission function from a measured hologram.

Fraunhofer approximation - the far-field

For distances $z \gg \frac{\pi}{\lambda}(x^2 + y^2)$, i.e. large distances behind the diffracting plane, one can approximate,

$$\exp \left(\frac{ik}{2z} [x^2 + y^2] \right) \approx 1 \quad (1.17)$$

in equation 1.11. By introducing new coordinates $k_x = \frac{x'}{\lambda z}$ and $k_y = \frac{y'}{\lambda z}$ the electric field expression from equation 1.11 then reads:

$$\tilde{E}(k_x, k_y) = \frac{\exp(ikz)}{i\lambda z} \int E(x, y) \exp(-2\pi i [k_x x + k_y y]) dx dy. \quad (1.18)$$

Thus the electric field pattern far behind the diffracting plane, i.e. in the far-field regime, has been reduced to a Fourier transformation. In our case, the measured intensity behind a waveguide structure thus corresponds to the squared modulus of the Fourier transformed field distribution at the exit of the guide.

1.3 The phase problem and phase retrieval

Measuring the far-field distribution behind a waveguide or behind an illuminated object, one would like to deduce the field distribution at the waveguide exit or the electron density at the position of the illuminated object. With the intensity I as the detected quantity,

$$I = \tilde{E} \times \tilde{E}^* = \left| \int E(\mathbf{r}) e^{-i \mathbf{k} \cdot \mathbf{r}} \right|^2, \quad (1.19)$$

the electric field distribution at the object position can not be uniquely determined, if there is no additional information available (as used e.g. in x-ray reflectiv-

ity measurements, where a model is fitted to the data). Assuming the illumination of an object with electron density ρ with a plane wave, the intensity can be written as:

$$I(\mathbf{q}_j) = \left| \sum_{r_j=0}^{N-1} \rho(\mathbf{r}_j) e^{-i \mathbf{q}_j \cdot \mathbf{r}_j} \right|^2. \quad (1.20)$$

To solve the under-determined equation 1.20, the number of unknown variables has to be reduced. In the following, two experimental methods are described, which allow to solve equation 1.20 uniquely without additional knowledge on ρ . The so-called 'Hybrid Input-Output Algorithm' originally developed from Fienup [Fie78] and experimentally realized by Miao and others [MCKS99, MIJ⁺02, WPVR03] uses extreme fine sampling of the diffraction pattern to overcome the under-determination. Holography instead uses the fact that the phase of the scattered wave can be measured by coherent interference with a known wave.

1.3.1 Hybrid Input-Output Algorithm

In equation 1.20 N^2 variables are unknown, but only $N^2/2$ equations are independent from each other, since the Fourier transform is centro symmetric. In other words: The complex phase of the electrical field at the detector cannot be measured directly. Following an approach suggested by [Fie78], the number of unknown variables can be reduced by placing the unknown object onto a support area of known electron density (without loss of generality $\rho(\mathbf{r}_j) = 0$ for $j > N$). In figure 1.6 an image of C. W. Roentgen represents an object sampled in N steps in each direction occupying an area S . Its Fourier transform then corresponds to a far-field diffraction pattern of the same object with coherent illumination (see. Eqn. 1.20). If the object is put on an area of constant electron density,

$$I(\mathbf{q}_j) = \left| \sum_{j=0}^{2N-1} \rho'(\mathbf{r}_j) e^{-i \mathbf{q}_j \cdot \mathbf{r}_j} \right|^2 \quad \rho' = \begin{cases} \rho(\mathbf{r}_j), & \mathbf{r}_j \in S \\ 0, & \mathbf{r}_j \notin S \end{cases} \quad (1.21)$$

then the N^2 unknown variables of the object can be determined, since $2N^2$ independent equation are provided. By increasing the real space size of the object with known electron density, the Fourier space sampling gets finer and thus the phase problem is solvable.

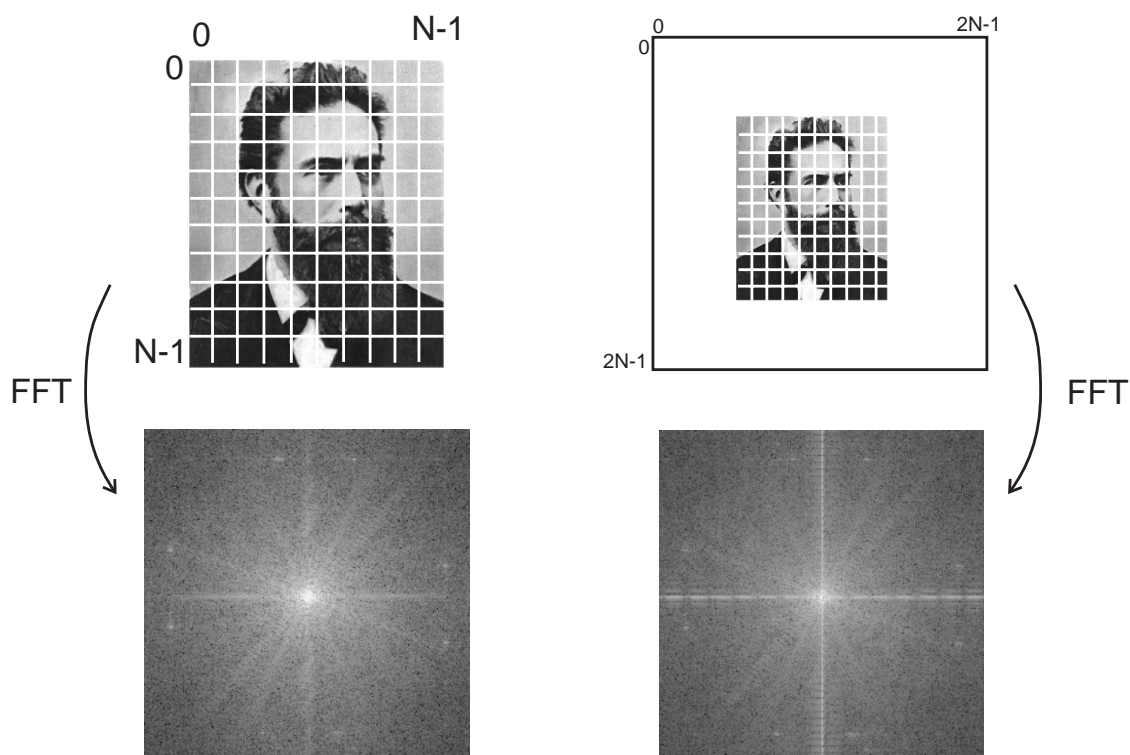


Figure 1.6: **left** Image of C.W. Roentgen sampled in N steps in each direction and the squared modulus of its Fourier amplitude is shown. **right** The object is put on a support with constant electron density, leading to a finer sampling in Fourier space.

In Figure 1.6 a hypothetical diffraction experiment is shown. The object (C. W. Roentgen) is discretized in N steps. On the left hand side of figure 1.6 the squared modulus of the Fourier amplitude of this object is shown using the fast Fourier transform (FFT) algorithm. It corresponds to the far-field diffraction pattern of the object illuminated with a fully coherent plane wave. On the right hand side the same diffraction pattern is shown, but the object was here put on a support of constant electron density before Fourier transformation. The diffraction pattern obtained from the object on the support is sampled at higher frequencies than the one from the not supported object. As long as the support size is big enough - for an object of size $N \times N$ a support of at least $2N \times 2N$ is necessary - it should be possible to reconstruct the object from its diffraction intensity. Suggested by Fienup [Fie78] and experimentally demonstrated by Miao and others [MCKS99, MIJ⁺02, WPVR03], this can be accomplished by the iterative hybrid-input-output algorithm. In figure 1.7 the iteration is sketched. Starting in the upper left corner, the detected intensity pattern is combined with an initial random phase, to obtain a complex valued

Fourier space pattern. An inverse fast Fourier transform¹ $(FFT)^{-1}$ is then used to obtain the first iteration of the real space electron density pattern ρ' . This electron density has to be positive in the sample area S , and has to converge to zero outside S . This real space constraint is applied, a factor $\beta \approx 0.85$ is used to adjust the convergence process [MIAH03], leading to a modified electron density pattern ρ . By calculating the FFT of the modified electron density, a new complex valued Fourier space array is obtained. Its amplitude is replaced by the square-root of the detected intensity pattern, and the iteration starts again. Depending on the size of the support and the image, the object is reconstructed after a few 100 iterations [MIAH03]. The algorithm has been implemented (using IDL) within the scope of this thesis (see Appendix C).

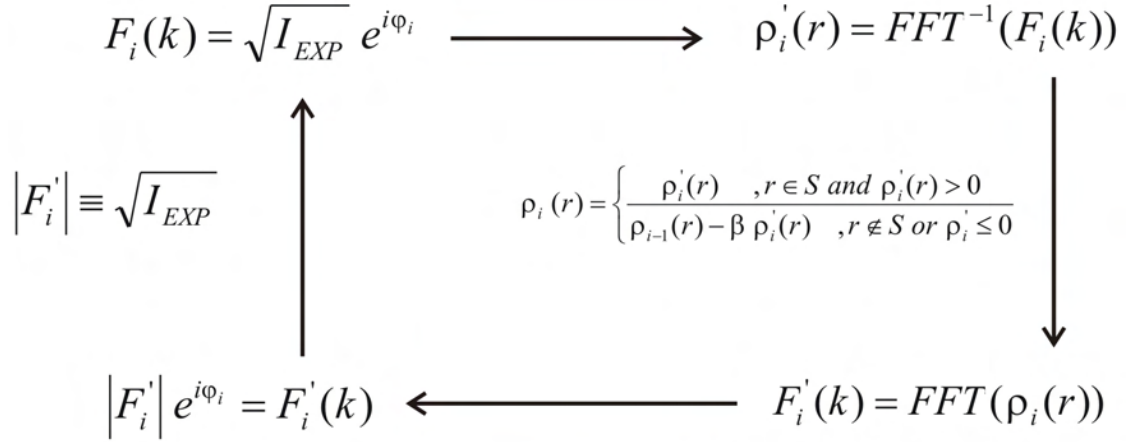


Figure 1.7: Iterative reconstruction loop for the hybrid-input-output method.

¹Only in case of an $2^N \times 2^N$ array; otherwise a discrete Fourier transform is used.

1.3.2 Holography

The principle of holography, introduced 1948 by Gabor [Gab48, LK03], allows to image phase information of an object wave O by coherently superposing a known reference wave R . Thus an electric field E at the detection plane is the coherent superposition of the object wave and the reference wave. The detected intensity can then be written as:

$$I = |E|^2 = |O + R|^2 \quad (1.22)$$

$$= OO^* + RR^* + RO^* + OR^* \quad (1.23)$$

To decode the object wave O from the intensity pattern, we can illuminate the detector image with the same reference wave ² and get the reconstructed field E_R

$$\begin{aligned} E_R &= I \times R \\ &= RR^*R + OO^*R + OR^*R + RO^*R \\ &= \underbrace{|R|^2 R}_1 + \underbrace{|O|^2 R^*}_2 + \underbrace{|R|^2 O}_3 + \underbrace{R^2 O^*}_4 \end{aligned} \quad (1.24)$$

with four terms representing:

1. zeroth diffraction order (primary beam) multiplied by constant factor R ,
2. primary beam modulated by object intensity (speckle pattern),
3. object wave enveloped by primary beam (direct image) and
4. complex conjugate of object wave enveloped by primary beam (twin image).

1.3.2.1 In-line holography

The illumination geometry introduced by Gabor [Gab48] to record a hologram behind an object is called inline holography. If we assume a geometry as depicted in figure 1.8 **A**, a sample is illuminated by a plane wave and the intensity pattern is detected at a position z behind the sample. Since both, waves stemming from the object (O) and waves passing the object without being disturbed (R), interfere at the detector position, a hologram is recorded. From the hologram the electric field at the object position can now be reconstructed.

²In our case the illumination is done numerically.

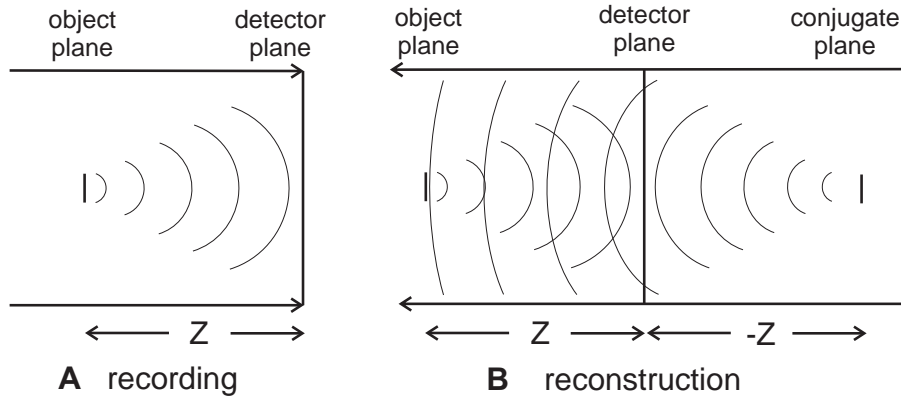


Figure 1.8: In-line geometry for holographic recording (**A**) and reconstruction (**B**). The reconstructed object wave at position z is superimposed by the reference beam shape and, more significantly decreasing the image quality, the (defocussed) twin image of the virtual object at position $-z$.

For visible light, the reconstruction is in most cases realized experimentally, by illuminating the object again with the reference wave [LK03]. In case of x-rays it is for practical reasons favorable to use a numerical reconstruction. During this reconstruction the sample is illuminated by the same plane wave and the electric field at position z in front of the hologram is considered the focussed object wave (see fig. 1.8 **B**). It is superimposed by its complex conjugate (the twin image) at position $-z$. Since both, direct image and twin image are on the same order of magnitude, the twin image can significantly decrease the image quality in reconstruction. Nevertheless, since in this type of geometry only one coherent beam source (i.e. one waveguide) is needed, it is the most simple setup to be realized for holographic imaging. Also, for objects with well defined shape, the image quality may not significantly be affected by the twin image (see chapter 4).

1.3.2.2 Reference beam holography

A possibility to separate twin image and direct image from each other is to separate reference wave and object wave from each other. This off-axis or reference beam geometry was first suggested by [LU62]. As sketched in figure 1.9 the hologram is again recorded at a distance z , but the object wave and reference wave are now spatially separated by each other. Again waves passing the object and waves propagating without being distorted by the object, interfere at the detector position and give rise to a holographic intensity pattern. In this geometry two wavefronts which are coherent to each other are necessary.

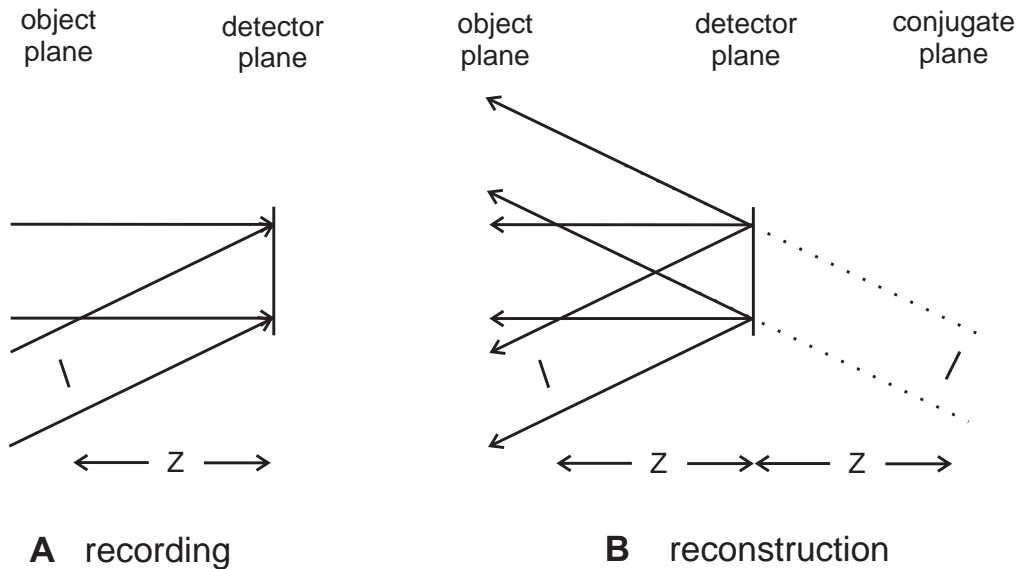


Figure 1.9: Geometry for reference beam holography recording and reconstruction. In contrast to the in-line geometry, direct image and twin image are spatially separated in the reconstruction.

The numerical reconstruction is again realized by illuminating the hologram with the reference wave. Since reference wave and object wave are spatially separated while recording the hologram, direct image and twin image are spatially separated in reconstruction. This geometry thus allows to reconstruct the wave at the object position without being intrinsically disturbed by the twin image. Using the transmission function described in section 1.2 the refractive index pattern in the object plane can be deduced. In chapter 4 the realization of the reference beam geometry for the case of hard x-rays is demonstrated.

1.3.2.3 Magnification

In order to allow for holographic microscopy applications, a magnification of the recorded sample is necessary. Without magnification, in the case of a plane wave illumination, the resolution in the image would be determined by the pixel size of the detector, which is on the order of some microns. In our case, the object is illuminated with divergent waveguided beams. As explained in [LCC⁺97b] the magnification of a sample in the waveguided beam is then given by the geometric magnification.

In figure 1.10 the beam geometry behind the waveguide is sketched. Let the distance between waveguide exit and sample be z_1 and the distance between sample

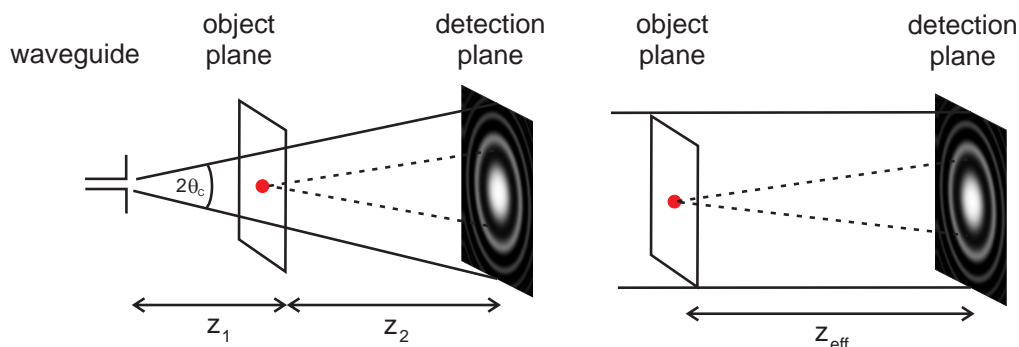


Figure 1.10: Sketch showing the magnification geometry. The hologram recorded in with the divergent waveguided beam at position z_1 behind the waveguide corresponds to a magnified image of the object recorded at position z_{eff} with a plane wave.

and detector be z_2 , then the geometric magnification M is defined as:

$$M = \frac{z_1 + z_2}{z_1}. \quad (1.25)$$

Illumination with a divergent beam sketched in figure 1.10 corresponds to a plane wave illumination with magnification M at an effective defocusing distance

$$z_{eff} = \frac{z_1 z_2}{z_1 + z_2}. \quad (1.26)$$

Using M and z_{eff} holography with a divergent beam can be transformed to the case of a plane wave illumination. It also enables the use of fast Fourier transformations when reconstructing the holograms. Thus a holographic reconstruction with a pixel array of 1024×1024 is performed within only a few seconds on a standard PC.

1.3.2.4 Resolution

As is the case for other optical systems, the imaging resolution Δ in the recorded image depends on the numerical aperture NA [LLT95]:

$$\Delta = \frac{\lambda}{2 \text{NA}} \quad (1.27)$$

In our case the sample is illuminated by a beam with divergence angle $2\theta_C$ (see figure 1.10), the width of the waveguide far-field, solely defining the numerical aperture. As described in section 1.2 the far-field of the waveguide is the Fourier transformation of the field at its exit. This implies, that θ_C increases while reducing

the guiding core dimensions. In other words: the resolution of the magnified hologram recorded with the waveguided beam is determined by the size of the guiding core.

Chapter 2

Waveguide and sample fabrication

To fabricate waveguides with guiding core sizes in the nm range and lengths of several millimeters, advanced lithographical methods are necessary. The fabrication of samples to test imaging applications presented in chapter 4 needs to be elaborate. In the following chapter the fabrication methods are briefly described.

2.1 Waveguide fabrication

All waveguides presented in this thesis consist of a small polymer core and a silicon cladding. They were prepared by spin coating a thin (30nm-100nm) polymer electron beam resist onto a silicon wafer. A structuring process with electron beam lithography (see 2.1.2) leads to two dimensional channels in the resist material. A subsequent evaporation of silicon onto these structures makes it possible to bury these low density resist structures in a silicon cladding. See also [See04, Jar05]. All these steps are sketched in figure 2.1.

2.1.1 Thin film spincoating

Two different types of resist materials were used: poly(methyl methacrylate) (PMMA), a positive electron beam resist (see section 2.1.2), and a calixarene type negative electron beam resist (see also 2.1.2). PMMA (Elvacite 2041, Leybold&Voss&Co, Germany) was dissolved in methoxyethylacetat and calixarene (XAR-N 7600/2, Allresist, Germany) was bought dissolved in chlorbezene.

As shown in Figure 2.2, the resists layer is prepared by depositing about 60 μ l of dissolved resist onto a 1 \times 1cm² silicon wafer and then rotating the wafer at a con-

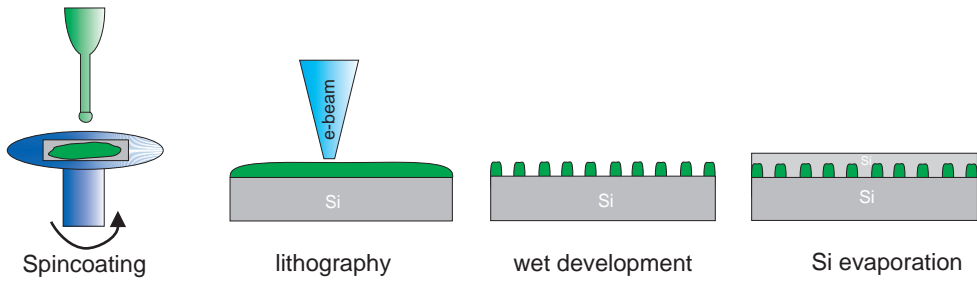


Figure 2.1: Waveguide fabrication: After deposition of a resist layer with defined thickness through spin coating, lateral structures are generated by electron beam lithography. In a subsequent step these structures are chemically developed. To create a symmetric refractive index contrast, a silicon layer is evaporated on top of the resist structures.

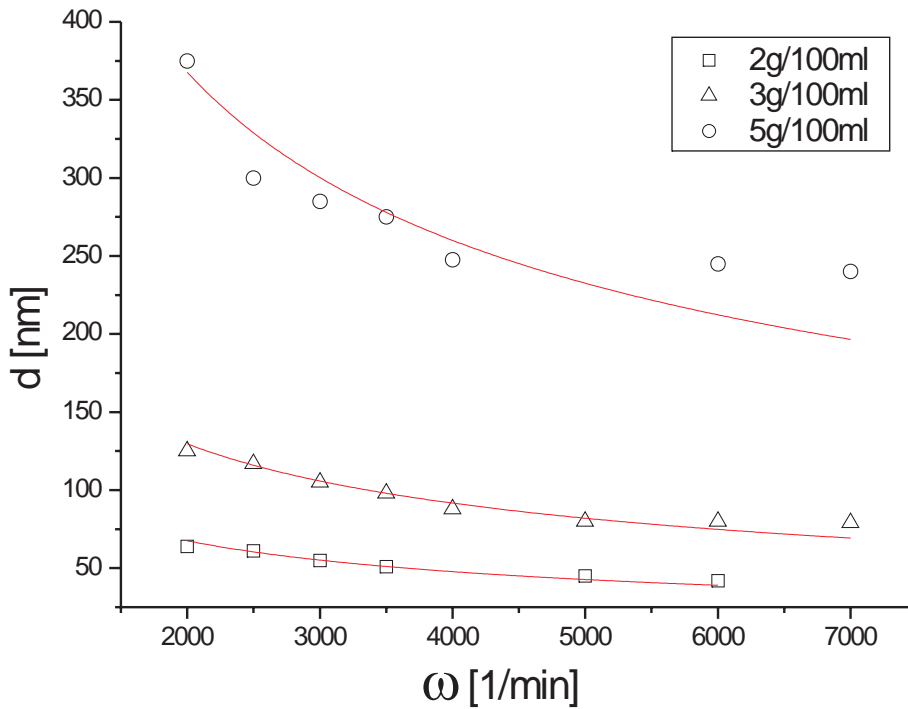


Figure 2.2: The dissolved resist is deposited onto the cleaned wafer which is then rotated at 2000 rpm to 7000 rpm. By changing the resist concentration in the solution and the rotational speed the layer thickness can be controlled. Shown here for the PMMA positive resist. The solid lines correspond to the theoretical $d \propto 1/\sqrt{\omega}$ behavior. (from [See04])

trolled speed of 2000rpm-7000rpm. By varying rotational speed and concentration of resist material in the solvent, the resists layer thickness can be controlled (see Figure 2.2). A detailed description can be found in [See04].

Depending on the resist type, by this method resist layer thicknesses between $10nm$ and $400nm$ can be achieved. These values are determined by x-ray reflectivity. To improve the sensitivity of the resist layer for the following e-beam lithography step, the samples were baked at temperatures of $\sim 150C$ for $30min-60min$ [FOOM96].

2.1.2 Electron beam lithography

Electron beam lithography (e-beam lithography) is a powerful technique to fabricate structures on a lengthscale of only a few nanometers. Derived from the scanning electron microscope (SEM), a focussed electron beam is scanned across a resist coated surface. Depending on the resist type, e-beam exposure either increases (positive resist) or decreases (negative resist) solubility of resist material for the liquid used in the subsequent development step. The minimal structural width depends on the used resist and the electron accelerating voltage. Using calixarene as negative resist, structure sizes of down to $10nm$ can be reached [FOOM96].

The lithography system used for structuring in the present thesis is a LION LV1 (Leica, Germany). It basically consists of a substrate stage with interferometric position encoders (resolution $\approx 2nm$), an electron optical column, a vacuum housing and control electronics for data processing and operating. Electron beam widths of $2nm - 5nm$ are reached at the sample. A detailed description of the e-beam lithography system can be found in [See04, Lei].

After exposure of the resist layer to the e-beam, the sample is developed in a solvent (ethylenglycolmonoethylether and ethylenglycolmonobuylether 4:1 for the PMMA and a methacrylacid based (XAR-600-59-2, Allresist, Germany) for calixarene) washing away the exposed (PMMA) or unexposed (calixarene) areas of the resist. After this development step, well defined resist structures are left on the silicon surface.

After the development process is finished, a $\geq 100nm$ thick silicon layer is evaporated on top. This is done with a Univex 450 (Leybold, Germany) evaporation system. As will be described in more detail in chapter 4 the waveguides are then cut to the desired length, depending on the incoming x-ray flux and energy. In figure 2.3 an SEM image of a single channel waveguide exit after cutting is shown. The cutting process leaves a rough edge and debris from this process may spuriously scatter the guided beam. Thus we decided to polish the cutting edges with a focussed ion beam.



Figure 2.3: Scanning electron micrograph of a single channel waveguide exit (red circle) after cutting but still unpolished.

2.1.3 Focussed ion beam

The focussed ion beam (FIB) workstation Nova Nanolab 600 (FEI, Netherlands) of the Institut für Materialphysik allows to polish waveguide entrance and exit after they have been broken to the desired length. This ensures that no spuriously scattered radiation is degrading the beam quality.

The FIB utilizes a *Ga* ion beam to sputter off material from a metallic surface. The up to 20nA ion beam is accelerated with up to 30kV and focussed onto the sample [FEI]. The nominal resolution is $\sim 7\text{nm}$ with a maximum horizontal field width of 2.5mm . With these parameters it is possible to polish up to 100 single channel waveguides on beam entrance and exit side within several hours only. To monitor the milling, an SEM is included in the FIB workstation. In figure 2.4 SEM images of a waveguide grating entrance are shown during different stages of FIB processing.

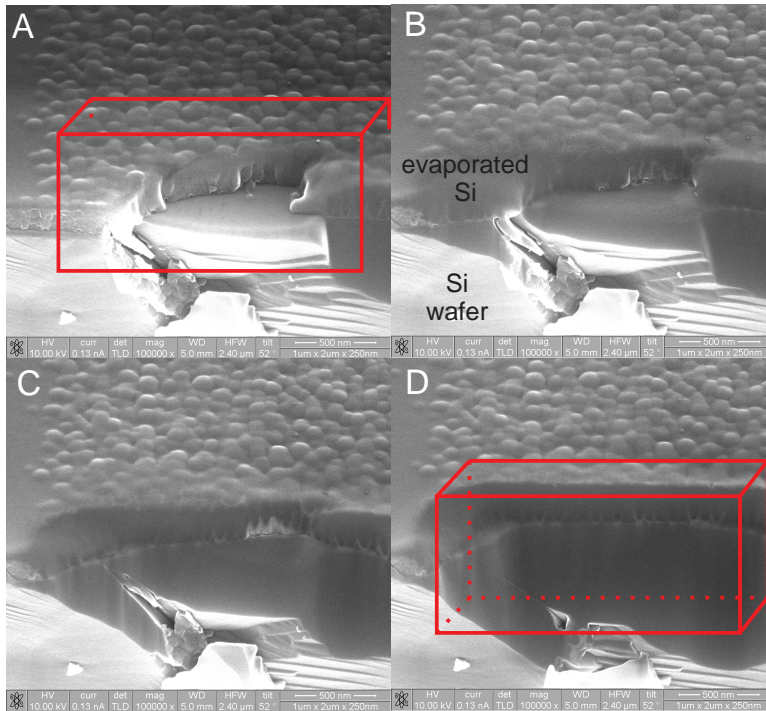


Figure 2.4: Scanning electron micrographs of a waveguide grating entrance during different stages of focused ion beam treatment. Debris and imperfections left from the cutting process from the entrance and exit of the waveguides are completely removed. In **A** the exit of a waveguide structure after cleaving is shown. **B-D** show the same region on the wafer during different steps of milling. The red box indicates the volume, which is removed during the process.

2.2 Sample fabrication

To demonstrate the potential of the methods discussed in chapter 1, test-samples were fabricated using a combination of e-beam lithography and lift-off techniques. The structures were prepared on thinned silicon wafers with a thickness of $\sim 150\text{nm}$. The fabrication of these structures is described in [Peu00], and is sketched in figure 2.5.

Starting point for the fabrication of ultra thin silicon foils are $200\mu\text{m}$ thick Si $\langle 100 \rangle$ wafers, with one surface doped with boron. The depth to which boron is doped into the silicon wafer surface defines the minimal thickness of the resulting silicon foil. Except for a small window on the bottom, the whole silicon wafer is covered with a layer of wax. The wax layer protects the silicon surface while a mixture of HNO_3 , HF and CH_3COOH isotropically etches through the wax window into the silicon. To remove most ($\sim 195\mu\text{m}$ of the $200\mu\text{m}$) of the silicon wafer,

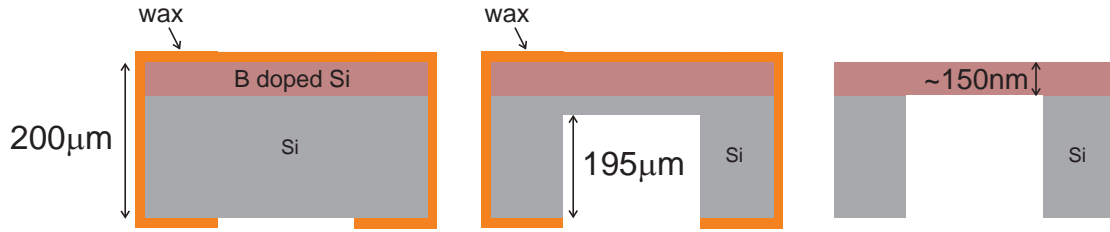


Figure 2.5: A doped silicon wafer is covered with wax leaving a window on the back. Etching with a mixture of HNO_3 , HF and CH_3COOH isotropically removes about $195\mu m$ of the $200\mu m$ thick silicon wafer. In the last step the wax is removed and a mixture of ethylenediamine and pyrocatechol selectively etches the silicon until it is slowed down by the boron doped layer. The window thickness is thus defined by the doping depth of the boron.

$\sim 30min$ etching is needed. In a final etching step a mixture of ethylenediamine, pyrocatechol and distilled water is used, to reach a thickness of about e.g. $150nm$ ¹ [Peu00]. The diameter of the silicon foil depends on the initial window size and is typically in the range of $2mm - 8mm$. In figure 2.6 **C** an image of such a silicon wafer foil glued onto a sample holder is shown.

These thinned silicon foils absorb less than 1% of the x-ray photons for the energy range used in this thesis ($8keV < E < 20keV$). Therefore they are perfectly suited as substrates for samples measured in transmission geometry. These transmission samples were prepared by a method called "lift-off" which is sketched in figure 2.6.

Comparable to the structuring process for the waveguides, an e-beam resist is spin-coated on top of the silicon foil surface. The used resist is PMMA, with a resist layer thickness of $\geq 200nm$. The structuring is carried out by e-beam lithography. The structured area defines the position of the metal on the foils. After the development step, metal is evaporated onto the sample. Fe layers can be evaporated directly onto the Si foils, while Au layers need a $\approx 4nm$ thick layer of Cr as adhesive layer. In a final step the remaining PMMA is removed by a 9 : 1 mixture of methylenchloride and acetone, washing away the metal layer on its top. This explains why the final thickness of the metal layer is limited by the initial thickness of the e-beam resist, since one has to avoid contact between metal in the ditch and on the resist. The typical metal layer thicknesses reached by this fabrication technique are about $150nm$. In figure 2.6 **B** a scanning electron micrograph of such a lift-off structure is shown.

¹The final thickness of the foil is defined by the etching time of the last step.

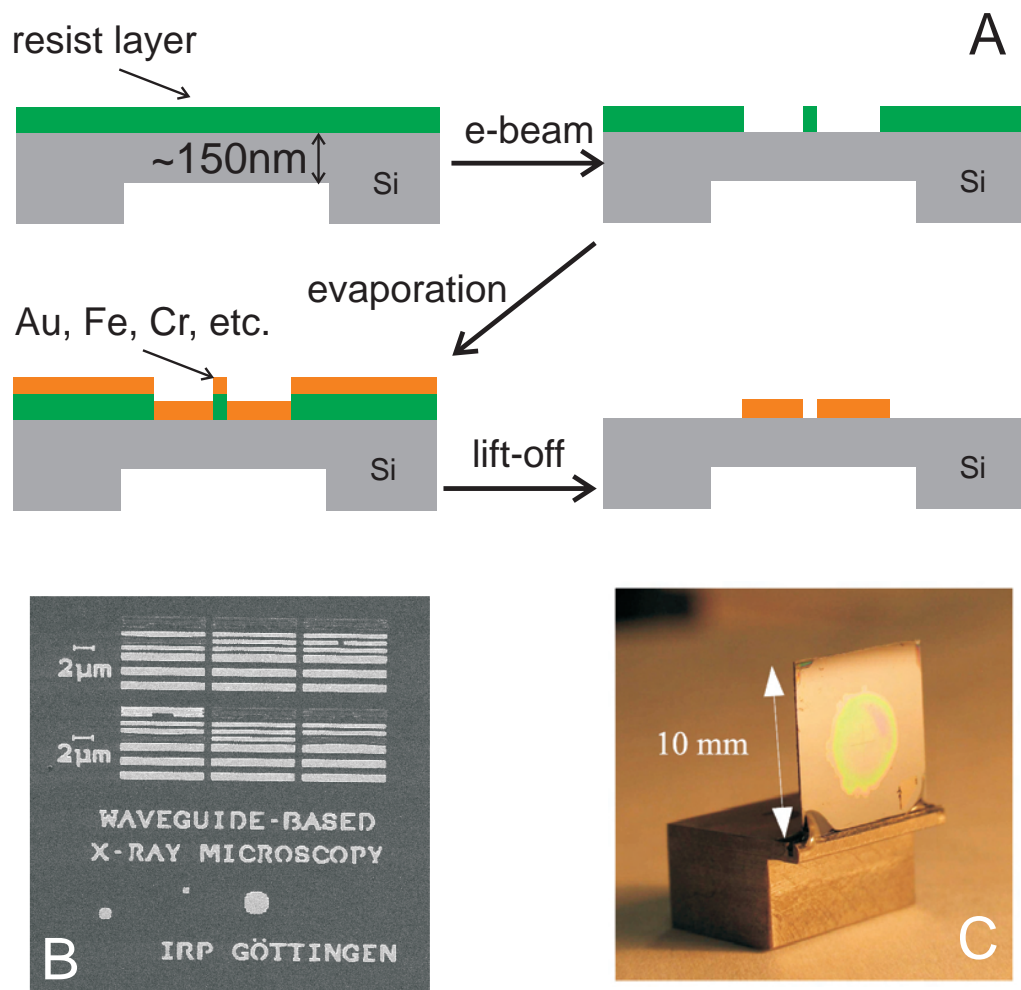


Figure 2.6: **A** For the lift-off preparation a resist is spin-coated and e-beam structured on a thinned silicon wafer substrate. After resist development, a metal (e.g.: Au, Fe, Cr) is evaporated. The metal layer thickness is kept smaller than that of the resist layer. Next, the resist is washed away together with the metal on its top. **B** Scanning electron micrograph of Au structures prepared by this lift-off technique. The lateral dimension is indicated by the $2\mu\text{m}$ scale bar. **C** Image of a sample glued on a holder ready for use in the MoWaSt setup.

Chapter 3

A mobile and modular waveguide imaging setup

In order to realize imaging with x-ray waveguides, numerous physical, technical and practical requirements and constraints have to be considered. A nan positioning system was designed and combined with a high efficiency detection system within the frame of this thesis. The aim was, to build up a motorized stage which can be installed at different beamlines, which enables the adjustment of a two dimensionally confining waveguide in a prefocussed beam and which allows for a high precision positioning of samples in the waveguided beam. In the following sections the realization of these aims is described. In the last section a layout for an in-house waveguide imaging setup is discussed.

3.1 General considerations

One major aim of this thesis was to realize an experimental setup with the following specifications: i) A prefocusing stage needs to fulfill all demands dictated by the respective optics ¹, i.e. translational and rotational degrees-of-freedom with sufficient precision. ii) The main stage is supposed to allow for alignment of 2D waveguides, i.e. translational precision corresponding to the cross-section of the prefocussed beam ² must be guaranteed. The angular resolution, is defined by the

¹e.g. Compound refractive lenses (CRL) [SKSL96] or Fresnel zone plates (FZP) or curved mirrors [OFS05]

²For the Kirkpatrick-Baez mirrors used in the experiments (chapter 4) the focal spot size is about $3\mu\text{m} \times 3\mu\text{m}$.

angular acceptance of the waveguide, which is in the range of $\sim 1\text{mrad}$ (see chapter 4). iii) A second stage must be implemented right behind the first one to allow for positioning of samples that are supposed to be illuminated by the waveguided hard x-ray beam. iv) The detection system has to be adapted to the enhanced requirements concerning flux and divergence of the guided beam.

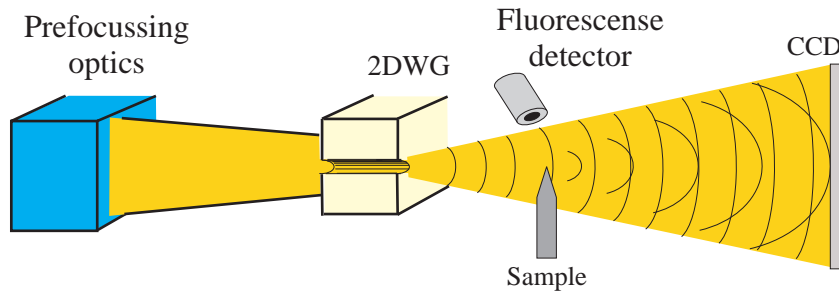


Figure 3.1: Sketch of waveguide imaging experiments. The waveguide entrance is positioned in the focal spot of the prefocusing optics. The sample is precisely positioned in the divergent beam downstream the waveguide exit. The detection system consists of i) a two dimensional detection array in the waveguide far-field for holographic imaging and ii) an energy dispersive detection system for scanning fluorescence positioned close to the sample.

The instrument enables two different experimental setups: a) Scanning fluorescence experiments, making use of the extremely small beam dimensions directly behind the guide, demanding highest resolution in sample positioning precision and b) holography experiments making use of the coherence and divergence of the hard x-ray beam. In case b) the sample must be positioned further downstream, when compared to case a).

Furthermore, it is necessary to equip the setup with stages that are transportable and that can sustain frequent mounting and dismounting at a beamline. Therefore we chose to separate the whole setup into three independent parts. One for the angular and translational alignment of the prefocusing optics (e.g. FZP or CRL), one for angular and translational alignment of waveguide and sample, and a motorized detector stage. With this modular approach the mobility of the setup is greatly enhanced and the user can choose a configuration, depending on the requirements of the experiment and the instrumentation provided by the beamline.

For compatibility with the ESRF beamlines, where most of the experiments were performed, SPEC (Certified Software, Cambridge, USA) is used as the instrument control software. It allows to include beamline motors in our setup and vice versa.

3.2 Positioning System

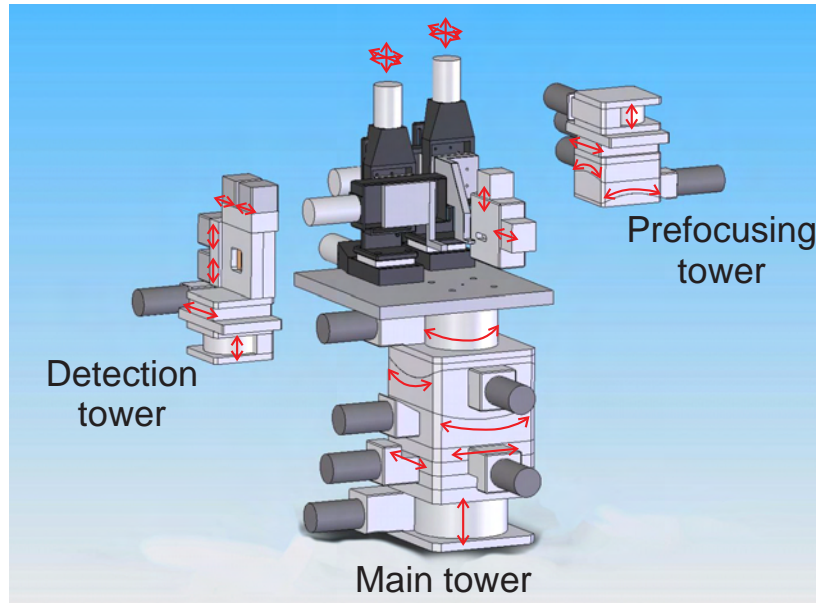


Figure 3.2: Sketch showing the arrangement of all motors in the MoWaSt setup. The prefocusing tower provides the necessary degrees of freedom for alignment of a prefocusing optics. The main tower allows for waveguide and sample alignment in the focal spot of the prefocusing optics. The detection stage is used to translate a point detector in the beam. The movement directions are indicated by the red arrows.

We chose to buy Huber (Huber Diffractionstechnik, Rimsting, Germany) stages for the rotations, most translations, the detector aperture and the pinhole mounting. Micos (Micos GmbH, Eschbach, Germany) microstep translation stages equipped with optical encoders were bought for the high resolution axes. All Huber axes are controlled by Huber SMC9300 controllers. A hardware driver for this type of controller was already available for SPEC. To be able to use the closed-loop mode on all Micos axes a Micos PEGASUS controller was installed. Since a SPEC driver for that controller was not available, it was developed in cooperation with CERTIFIED SOFTWARE (Cambridge, USA) and Micos within the frame of this thesis. It is now included in the standard distribution of SPEC as part of the hardware library. An arrangement of all three stages is sketched in Figure 3.2.

3.2.1 Positioning Control system

To guarantee mobility the intire computing and control electronics is mounted in a single 19" rack. It consists of one standard computer (Intel pentium 2.8GHz,

1GB RAM, 140GB Hard disk), three Huber SMC 9300, one Micos pegasus motor controller, a National Instruments NI-6602 acquisition board and a NIM crate. The control computer is additionally equipped with one IEEE 488 (GPIB) interface board, two additional serial ports and an additional ethernet card. As operating system a SuSe Linux 9.0 distribution with a customized 2.4.21 kernel is used. During an experiment this rack is placed in the experimental hutch, so that the cabling between the motors and the respective controllers is only necessary inside the hutch. To control the system the X window desktop is exported via network to a computer placed in the control room (see Fig. 3.17).

Making use of the powerful network capabilities of SPEC and Linux, beamline provided motors and detectors can be implemented into the MoWaSt setup. That allows for controlling all motors and detectors from one SPEC session, and logging their status continuously into one single datafile.

3.2.2 Positioning tables

Overall, 24 motorized stages are used for alignment of prefocusing optics, waveguide and sample. Depending on the function in the setup, the properties of the individual stage can vary. In table 3.1 all motors included in the setup are listed.

The main tower is responsible for alignment of the waveguide in the focal spot of the prefocusing optics and for the subsequent alignment of the sample in the waveguided beam. Two high precision XYZ stages are mounted on top of the main tower. One is necessary to align the waveguide into the pivot-point of the HUBER rotary stages and one for the alignment of the sample in the waveguided beam. These stages are highlighted in figure 3.3. An additional HUBER 5102.102 stage can be mounted upstream the pivot-point of the HUBER rotary stages to align a pinhole, in order to reduce spurious radiation from the prefocusing optics. The stepper motors in the Micos tables are Vexta (Germany) D4CL-5.0F. These high precision stages are controlled with a Micos PEGASUS controller with a standard closed-loop control system (see also section 3.2.3).

The detection stage (Fig. 3.4) is designed to use a scintillation point detector for alignment of the waveguide in the focal spot of the prefocusing optics. For energy dispersive experiments a silicon drift chamber detector (see section 3.3) can replace the scintillation detector.

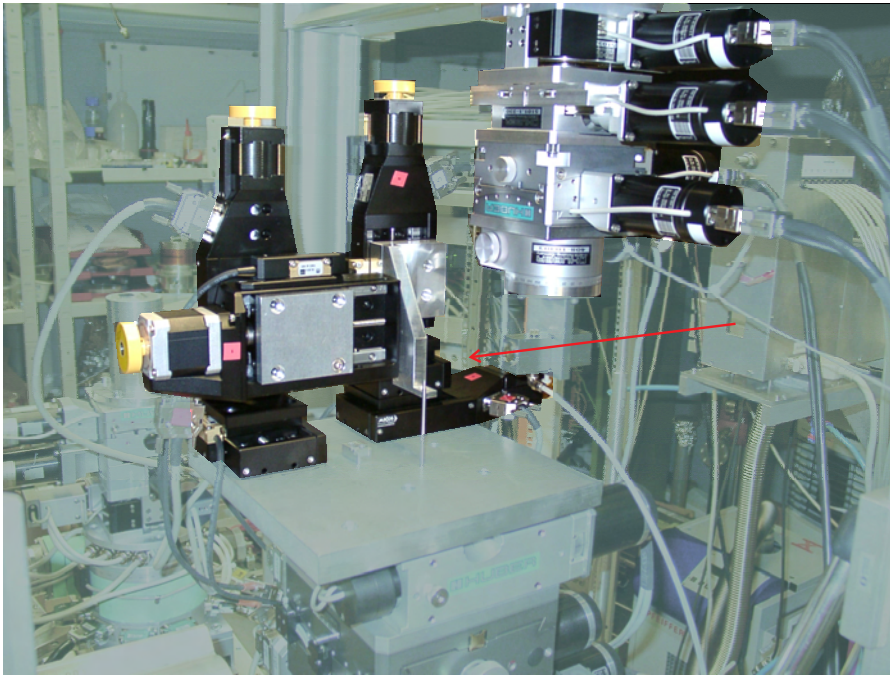


Figure 3.3: Prefocusing stage and main tower installed at the EDR beamline at Bessy II in December 2004. The beam is entering from the right and passing the focusing mirror attached to the prefocusing stage as indicated by the red arrow.

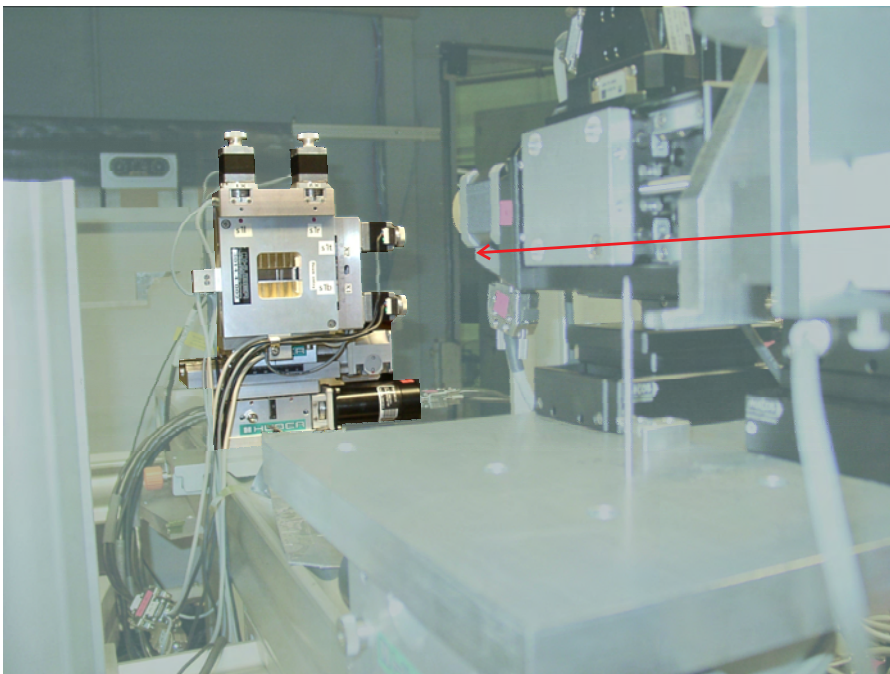


Figure 3.4: The detection stage recorded in beam direction. In the foreground the waveguide and sample stages are visible. The red arrow indicates the beam direction.

Mnemonic	Type	commercial name	travel range	step size
Prefocusing tower				
fz	translation	Huber 5103.1	15mm	20nm
fy	translation	Huber 5101.1	60mm	100nm
fxrot	rotation	Huber 5203.1	15	0.0001
fyrot	rotation	Huber 5203.1	15	0.0001
pv	translation	Huber 5102.1	15mm	625nm
ph	translation	Huber 5102.1	15mm	625nm
Main tower				
zgt	translation	Huber 5103.2	40mm	20nm
xgt	translation	Huber 5102.2	30mm	2 μ m
ygt	translation	Huber 5102.2	30mm	2 μ m
xrot	rotation	Huber 5203.210	40	0.0001
yrot	rotation	Huber 5203.210	40	0.0001
zrot	rotation	Huber 410	360	0.0001
Sample and Waveguide stages				
wgx	translation	Micos MT-65	25mm	3nm
wgy	translation	Micos MT-65	25mm	3nm
wgz	translation	Micos MT-65	25mm	3nm
sx	translation	Micos PLS-85	50mm	3nm
sy	translation	Micos MT-65	25mm	3nm
sz	translation	Micos MT-65	25mm	3nm
Detection tower				
detz	translation	Huber 5103.1	15mm	20nm
dety	translation	Huber 5101.1	60mm	100nm
s1l	slit	Huber 3014.4	25mm	1.25 μ m
s1r	slit	Huber 3014.4	25mm	1.25 μ m
s1b	slit	Huber 3014.4	25mm	1.25 μ m
s1t	slit	Huber 3014.4	25mm	1.25 μ m

Table 3.1: List of the motors included in the mobile and modular waveguide imaging setup.

3.2.3 Accuracy, precision, trueness and stability

In measurements, where the stepsize of a scan reaches the limit of the motor, positioning errors become important and have to be considered. In Figure 3.5 the intensity of a fluorescence scan of a tungsten tip in a waveguided beam as a function of the sample position is shown (see also chapter 4). Several 'jumps' in the displayed position are clearly visible for several points due to the precision of the positioning system. As is presented in chapter 4, beam widths of well below 100nm were measured in the present thesis (see also figure 3.5). To ensure that the instrumental precision is not spoiling these values, we will focus in this section on the concepts of measurement precision and motor control, following the approach given in [HAMX97].

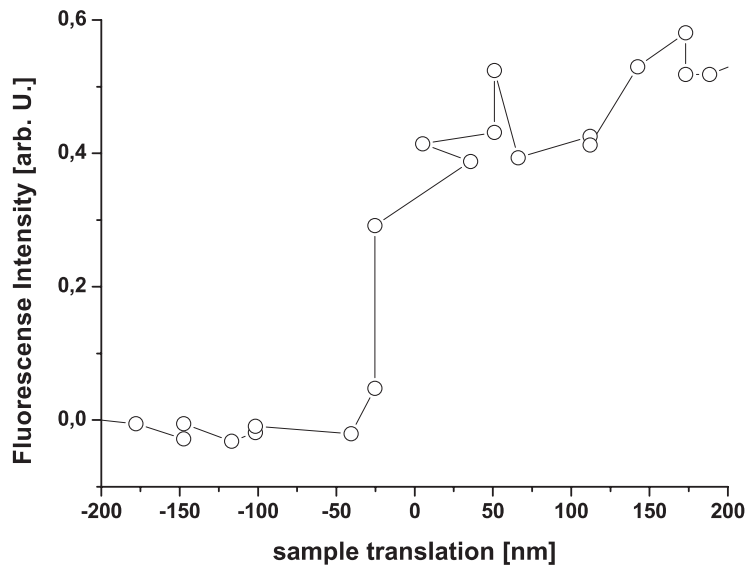


Figure 3.5: Fluorescence scan of a tungsten tip through a waveguided beam. Jumps in the position reading are clearly visible and are due to the precision of the translation system.

3.2.3.1 Static performance

Let us assume a movement of a translational stage from position 0 to a true position x_P (see Fig. 3.6 A). The position sensor measures the position x_M . The difference between x_P and x_M is called *trueness* with the systematic error δx_{MS} . The random error of the position measurement is δx_{MR} and is called *precision*. Thus, if δx_{MR}

is small and δx_{MS} is finite, one will get precisely the wrong position! The general term *accuracy* is defined as $\delta x_{MA} = \delta x_{MS} + \delta x_{MR}$, i.e. the sum of *precision* and *trueness*. These errors originate from the limited resolution of the encoder system in the stage ($\pm 15.26\text{nm}$), from the limited positioning precision of the stage motor ($3 * 10^5$ steps per revolution $\approx 3 \text{ nm}$), from the digital command precision (16 bit) and from others like noise and vibrations in the encoders and motors. To reduce all these positioning errors a closed-loop control system is used (see below).

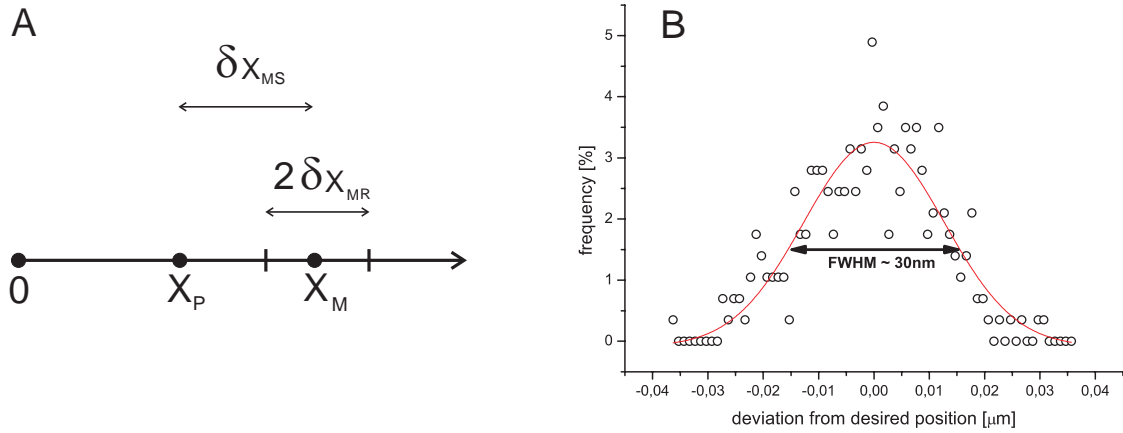


Figure 3.6: **A** Sketch illustrating a motor movement with positioning errors. **B** Evaluation of the encoder readings of the waveguide translation. By plotting the frequency of the deviation from the desired position a full-width-at-half-maximum of 30nm is obtained by fitting a Gaussian.

For the waveguide and sample translations the positioning precision of the system can be evaluated by plotting the frequency of the deviation from the desired position in a scan measured with the optical encoders as shown in Figure 3.6. A Gaussian fit exhibits a full-width-at-half-maximum (FWHM) of about 30nm. Since we do not know the exact position of the motor (*trueness*) - we only know where it should be - this value corresponds to the *precision* $2\delta x_{MR}$ of the translation system.

The value of $\delta x_{MR} \approx 15\text{nm}$ matches the nominal resolution of the optical encoder system integrated in each MICOS stage. This is due to the closed-loop control mechanism used to move all high precision stages. The basic concept of this control mechanism is sketched in Figure 3.7.

After movement commands from the host computer are transferred to the controller the position of the stage is continuously compared to the encoder-readings. In case of positioning errors, they are iteratively decreased by re-commanding the desired position. If the reached position is within some error limit the encoder reading is transferred back to the host computer and the movement is finished.

Let us assume that a position X_c is commanded, a true position X_p is reached and a position X_m is measured. Then a closed loop control can be described by figure 3.7. The commanded position X_c is transferred to the motor by a transfer function G . G is generally not linear and depends on time and temperature. While transferring this command to the motor an error b_1 can be introduced. The movement itself is executed with a transfer function P , again introducing errors b_2 and b_3 due to limited motor precision (e.g. dead-band errors, non-linearities) in the motor and mechanical errors like thermal expansions in the system. The reached position X_P is then measured (transfer function H) and compared to the initial commanded position X_C .

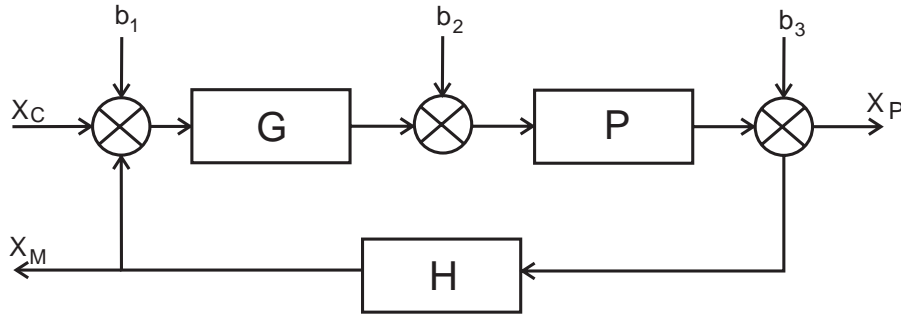


Figure 3.7: Execution of a positioning command in a closed-loop system. The commanded position is sent to the positioning controller and from there to the stage. The encoder system reads out the reached position. In case of positioning errors the controller again commands the desired position until the encoder readout is within the error limits.

Thus the reached position in the closed loop system can be described by [HAMX97]:

$$\begin{aligned} X_P &= b_3 + P[b_2 + G[X_C + b_1 - HX_P]] \\ &= \frac{b_3}{1 + HPG} + \frac{Pb_2}{1 + HPG} + \frac{PG(X_C + b_1)}{1 + HPG} \end{aligned} \quad (3.1)$$

To reduce the influence of error effects, one needs to make G effectively infinite and is then left with

$$X_P = \frac{X_C + b_1}{H}, \quad (3.2)$$

meaning that the reached position only depends on the input offset b_1 , which is of course undistinguishable from the command, and on imperfections in the measurement process H . This explicitly means, that the (static) performance in an closed-loop system only depends on the performance of the encoders system. It

actually explains the measured precision (see fig. 3.6) of $\pm 15\text{nm}$ for the MICOS stages.

3.2.3.2 Dynamic performance

So far we have considered a system, where non-varying command inputs are considered and where speed and mass of the stage are of no importance. In reality, the performance of a system with varying command input depends on the mass and stiffness of the stage, the frequency response of the controller and the acceleration of the motor. This can be compared to a driven oscillator with damping. Resonant frequencies of course have to be avoided (or at least reduced). As sketched in figure 3.8 **A**, strong oscillation can occur for an uncontrolled system. In order to overcome this limitation, quite involved feedback control systems, such as the classic proportional, integral and differential (PID) control setup are used [HAMX97].

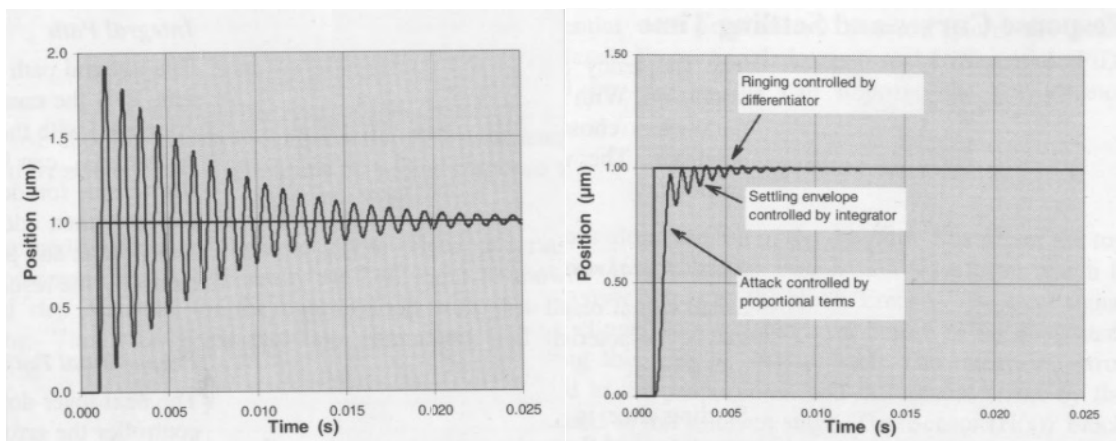


Figure 3.8: **A** Signal response of an open loop resonant stage and **B** response of the same stage in a PID controlled closed loop system. (from [HAMX97])

The technical realization of this type of feedback control, which is also used in the Micos Pegasus controller, is quite involved and we referred here to [HAMX97, Föl92] for further reading. In figure 3.8 **B** the response to a commanded step is shown for a PID controlled system. Here, the desired position is obviously faster reached than in the uncontrolled case. The initial slope in the system response (attack) is controlled by the proportional terms, the oscillation (ringing) by the differential terms and the damping of the system response (settling) by the integral terms. Obviously the optimal values for the parameters, i.e. the values, where the motor settles fastest, depend on the commanded step size. Thus an optimization of

the feedback control system could be obtained, by dynamic adjusting of the PID parameters depending on the commanded step size.

For obvious reasons, the performance of the PID system is limited to a certain frequency bandwidth, within which positioning errors can be corrected. As part of an x-ray nan positioning system, this temporal response of the system can affect the time structure of the waveguided beam. Additional time structures are due to beam fluctuations, starting from the bunch structure at high frequencies to thermal drift on the low frequency end.

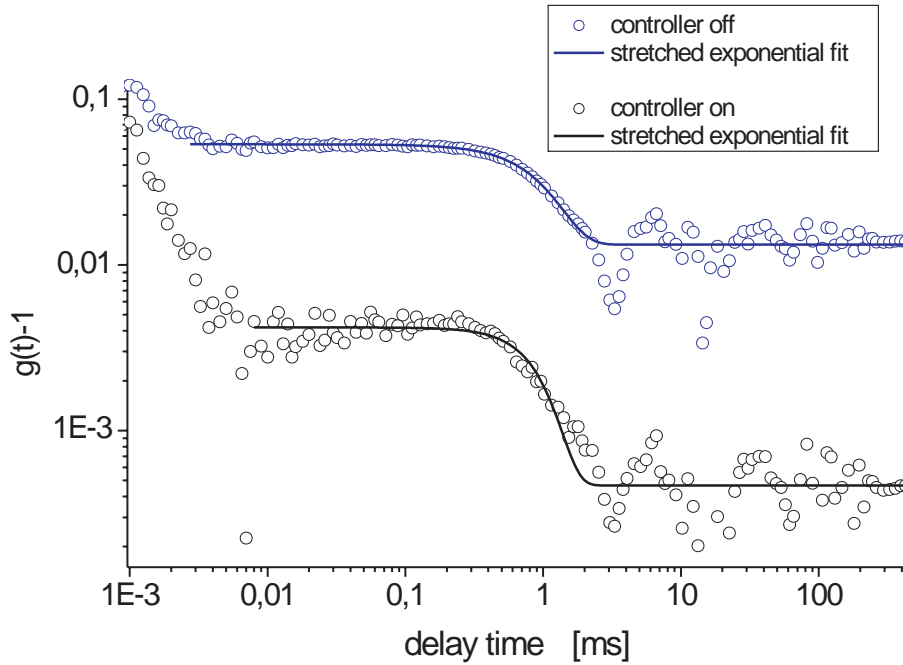


Figure 3.9: Measurement of the temporal correlation function $g(\tau) - 1$. The two graphs correspond to the measured correlation in the far-field of a two dimensionally confining waveguide in the focus of a Kirckpatrick-Baez (KB) mirror setup at ID22 with switched on and turned off motor controllers.

$$g(\tau) - 1 = \frac{\langle I(t) I(t - \tau) \rangle}{\langle I(t) \rangle^2} \quad (3.3)$$

As defined in equation 3.3, $g(\tau) - 1$ is the intensity autocorrelation of a measured signal. In our case this correlation was obtained using a multiple tau digital correlator (ALV, Langen, Germany). In figure 3.9 measured correlation functions of

the waveguide far-field are compared, with and without using the Micos feedback control.

This shows, that the feedback control of the Micos controller is able to damp the autocorrelation for the whole frequency range covered by the measurement. Note, that the decay in the autocorrelation at $\approx 1\text{ms}$ could correspond to characteristic times of a feedback control upstream the waveguide, e.g. in the focusing optics.

3.3 Hard x-ray photon detection

3.3.1 Two dimensional detection

An efficient photon detection system is a crucial point for a successful waveguide imaging experiment (see also chapter 4) [OFKS06]. For in-line holography, intensity variations of only a few percent are to be detected. For a suitable ³ resolution in the waveguide far-field an angular resolution in the range of $1\mu\text{rad}$ is necessary. For these specifications direct illumination silicon charge coupled devices (CCD) provide efficient and affordable two dimensional x-ray detectors (see e.g. [FBM04]). In contrast to x-ray CCD cameras where the x-rays are first converted to optical light with a scintillation foil (see e.g. [Ins]), direct illumination CCDs allow direct detection of x-rays with the CCD chip. Of particular advantage is the efficiency of well above 10%. Disadvantageous is that the pixel size is limited to about $10\mu\text{m}$ - $15\mu\text{m}$ ⁴[FBM04].

In figure 3.10 the layout of a direct illumination x-ray CCD is sketched. The CCD chip consists of an electrode structure, a nonconducting oxide layer, a depletion region and a bulk silicon layer. For x-ray detection the depletion region ($20\mu\text{m}$ - $50\mu\text{m}$) is bigger compared to optical light depletion regions ($5\mu\text{m}$ - $20\mu\text{m}$) in order to increase the probability of absorption (quantum efficiency). The incoming x-ray photons are transmitted through the electrode and isolation layer and are absorbed in the highly doped depletion region. For an absorbed multi keV x-ray photon several thousand electron-hole-pairs (mean transition energy 3.65 eV) are excited. Since a voltage in the electrodes in the top layer is applied, a potential well close to the isolation layer is induced in the depletion region. For a p-doped

³The Young interference after a double waveguide used for reference beam holography has to be resolved.

⁴At least for a chip architecture with silicon ⁴At least for a chip architecture with silicon and in the photon energy range between 5keV and 20keV .

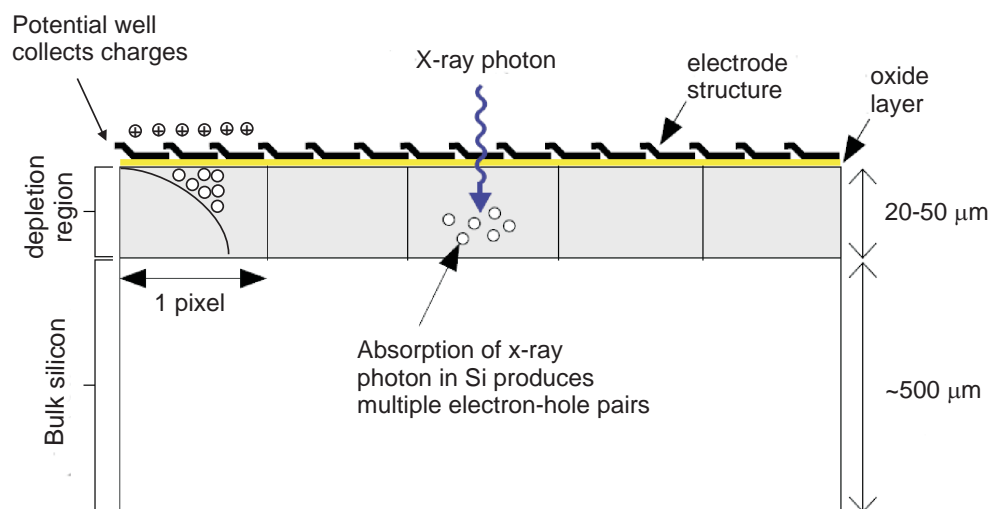


Figure 3.10: Schematic view of a front illuminated x-ray CCD chip. The mean transition energy for an electron-hole pair is 3.6eV; thus an absorbed multi keV photon produces several thousand of electrons, which are collected in the potential well of each pixel.

depletion region, the applied voltage is positive, and thus the electrons are collected in the potential well. The amount of collectable electrons in this single pixel potential well depends on the specific chip architecture and finally defines the maximum number of detectable photons for one acquisition.

A distinction is drawn between front illuminated CCD chips, as sketched in Fig. 3.10, and back illuminated chips, where the photons are incident onto the thinned bulk silicon layer. These back illuminated chips are better suited for hard x-ray detection than front illuminated CCDs, since the electrode structure is protected from incoming x-rays and thus the noise production is suppressed and the lifetime of the chip is longer. The biggest disadvantage of back illuminated chips is the (up to 60%) higher price, because of the more complicated production process.

After the acquisition process is finished the electrons in the respective pixels have to be transferred to an amplifier and converted to an electron proportional voltage for further processing. The readout depends on the chip architecture. Full frame (FF), frame transfer (FT) and interline transfer (IT) chips are distinguished (see figure 3.11).

For FF chips the readout works as follows: By changing the voltage in adjacent pixels the electrons are transferred row by row into the shift register. From there each shift register pixel is transferred into the amplifier. This type of readout design

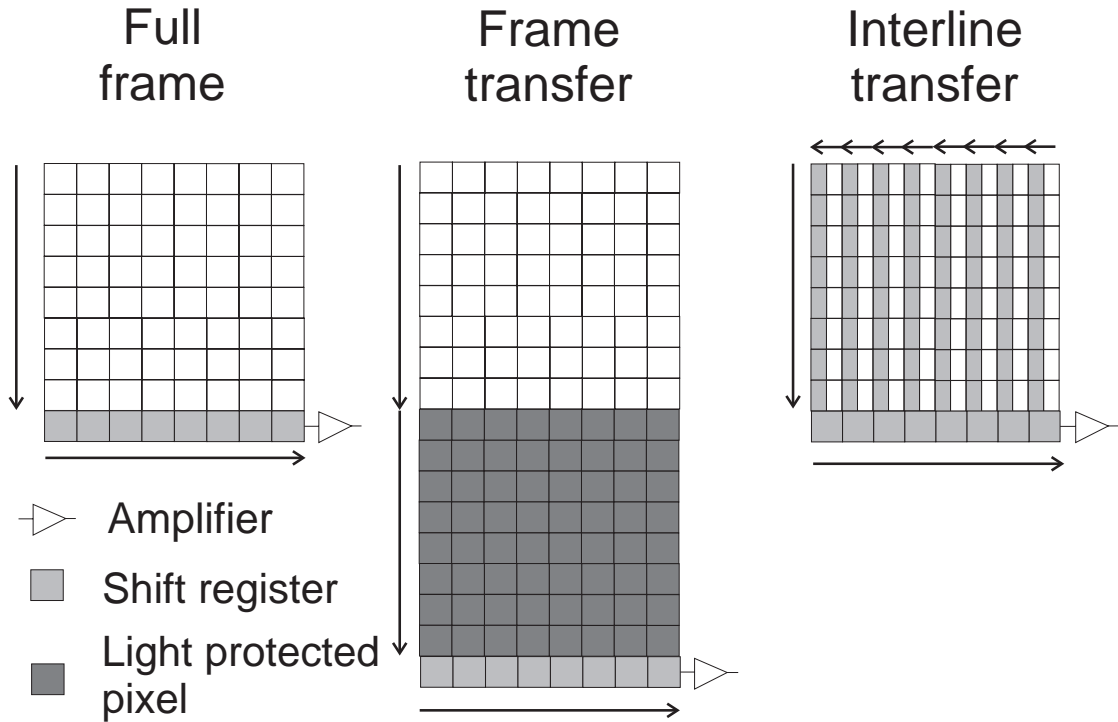


Figure 3.11: CCD readout architectures. In the full frame design the electrons are transferred from pixel to pixel into the shift register and from there into the amplifier. The frame transfer design transfers the electrons of the whole frame into an light protected region and from there into shift register and amplifier. In interline transfer chips each pixel has its own transfer pixel.

allows that the full chip area is sensitive to light, but for readout the chip has to be protected from incident photons by a shutter. FT chips quickly transfer the whole frame into a light protected area from where it is read out. Thus the next acquisition can be started, while readout is still in progress. FT chips require nearly a twice as large chip area as FF chips and are thus much more expensive. IT chips are the fastest chips in readout time, since each pixel has its own transfer pixel. Because of this architecture the chip area is not completely sensitive to light and, especially for x-rays, the transfer registers are hard to protect from incoming photons.

We chose to buy a Princeton Instruments (Trenton, NJ, USA) LCX-1300 CCD system. It is a front illuminated, deep depletion, full frame type of CCD. The key features of this detection system are listed in Table 3.2.

The full well capacity of 400.000 electrons per pixel theoretically allows for example the detection of up to 133 photons with an energy of $10.8keV$, since each of these photons would excite 3000 electrons. In practice several effects have to be taken into account when calculating the number of photons incident on each pixel:

pixel size	$20\mu m \times 20\mu m$
number of pixels	1340×1300
single pixel full well capacity	400.000 electrons
Analog-digital-converter dynamic range	16 bit
Dark current	≈ 100 electrons / pixel / second
readout noise	≈ 10 electrons rms

Table 3.2: Main properties of the Princeton Instruments LCX-1300 x-ray CCD system.

Depending on the photon energy, only a certain amount of photons are absorbed and detected in the depletion region. For the LCX-1300 system this energy dependence is shown in figure 3.12. Towards low energies the efficiency is dominated by absorption of photons before reaching the depletion region and towards high energies the absorption probability in the depletion region is dominant.

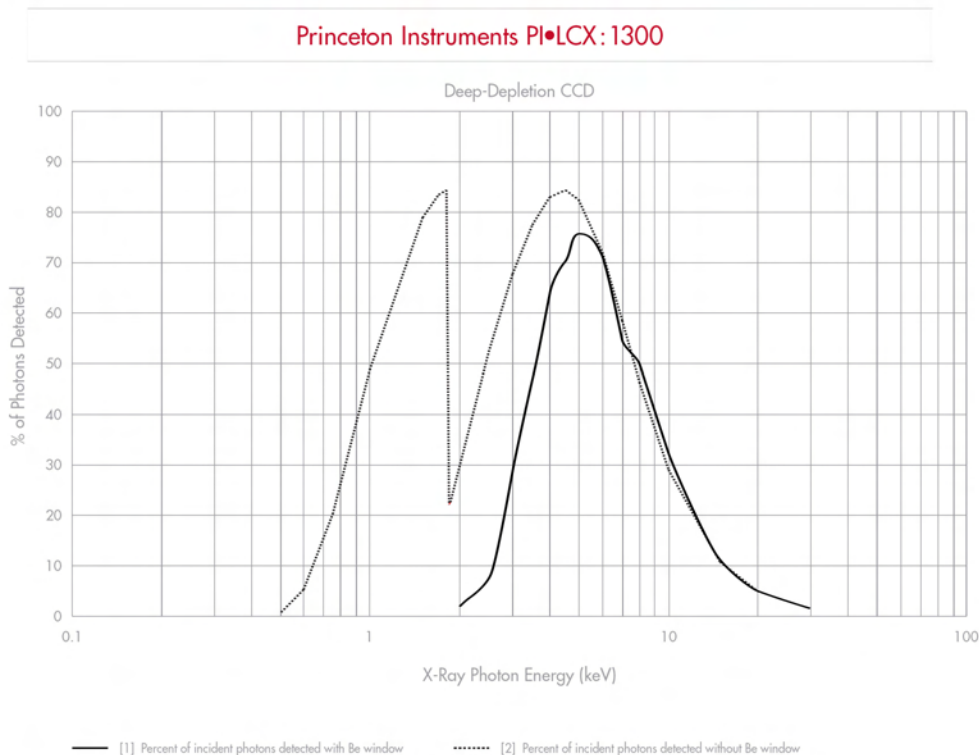


Figure 3.12: Detection efficiency of the Princeton Instruments LCX-1300 CCD. With the installed Be window about 20% - 40% of the photons are detected in the energy range between $8keV$ - $12keV$. [Ins]

Although the CCD chip is thermoelectrically cooled, thermal effects induce electrons in each pixel, generating the so-called dark current. As can be seen from table 3.2 this value is quite low compared to the number of electrons excited by an x-ray photon, but can become important for long time acquisition of weak signals. Another effect is noise generated during readout. It is induced while the electrons are transported from the light sensitive pixels into the amplifier and from there into the analog-digital (AD) converter. It depends on the readout speed and amplification gain and is typically in the range of about 10 electrons rms.

After the amplification process (amplification factors between 1.2 and 12 can be applied) the signal is discretized by the AD converter into 16 bit equidistant steps. Depending linearly on the amount of electrons stored in each pixel, a value between 0 and 65535 of these analog-digital-units (ADUs) is displayed as intensity value.

While interpreting these intensity maps, the user has to consider effects which can decrease the data quality: The effects described above, which lead to a dark current, can be compensated by subtraction of a frame acquired under the same conditions as the data frame, but without illuminating the CCD. By illuminating the CCD homogeneously, efficiency variations from pixel to pixel can be detected and compensated by dividing the data frame with such a flat field.

3.3.2 Energy dispersive detection

As described in section 3.1 the MoWaSt setup is supposed to be equipped with an energy dispersive detection system to allow for fluorescence imaging and experiments at the white beam beamline EDR at Bessy II. This is accomplished by including a Roentec XFlash 1001 (Roentec, Germany) silicon drift detector or alternatively a Si(Li) detector (Eurisys Mesures, France) owned by the ID22 beamline (ESRF, France) where most experiments were performed (see chapter 4). In this section the functional principle of both detectors is briefly described.

3.3.2.1 Silicon drift detector

Silicon drift detectors (SDDs) make use of the fact, that the number of excited electron-hole pairs in a silicon semiconductor depends on the energy of the absorbed x-ray photon (see also section 3.3.1). Following the explanations given in [Egg02], a silicon drift detector works as follows:

As sketched in figure 3.13 the photon active part of a SDD consists of a n-doped silicon wafer with a typical thickness of some $100\mu m$. This wafer is sandwiched by a p-doped back contact on the photon entrance side and p-doped so-called drift rings on the back side. A negative voltage is applied to the drift rings and the back contact giving rise to a space-charge region or depletion region throughout the whole n-doped silicon. This reduces thermally induced electron-hole pairs and allows to operate the detector at moderate temperatures (thermoelectrical cooling to about $-40C$). Since the applied negative voltage in the drift rings is increasing from inner to outer rings, a potential gradient is induced parallel to the wafer surface. This leads to a drift (electron drift speed about $10^3 - 10^4 \frac{m}{s}$) of the photon excited electrons towards the anode in the middle of the structure. The anode is connected to a field effect transistor (FET) with low capacity, which allows to transform the incoming electrons into a measurable voltage pulse.

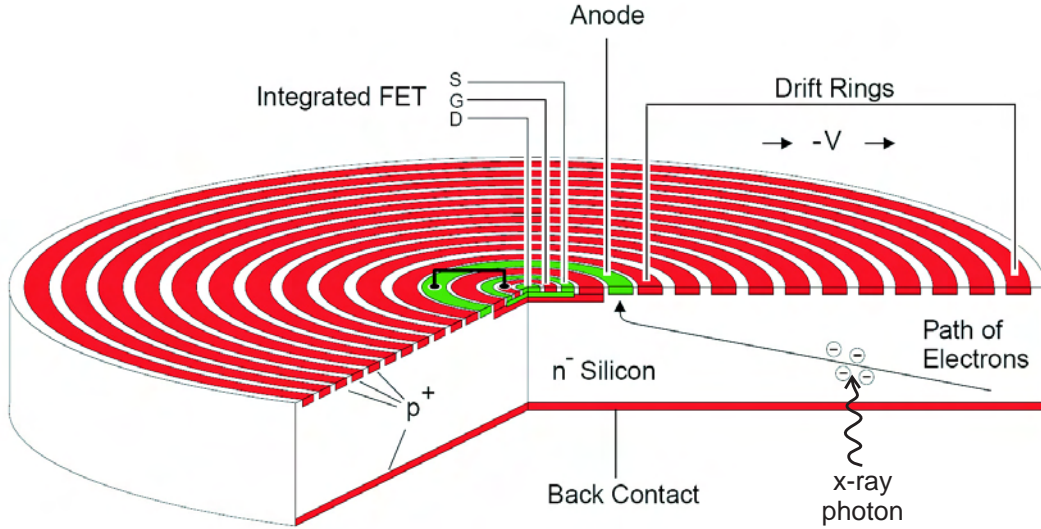


Figure 3.13: Sketch of the architecture of a standard silicon drift detector. The incoming x-ray photon excites an energy dependent number of electron-hole pairs. The electrons then follow the potential induced by the drift rings and are collected at the anode. With the help of an incorporated transistor a photon energy dependent voltage pulse is detected. (adapted from [Egg02])

For an x-ray energy of $E = 6keV$, a capacity of $200fF$ and the mean electron-hole-pair transition energy of $\omega = 3.65eV$ a voltage pulse of

$$\Delta U = -\frac{Ee}{\omega C} = -1.3mV \quad (3.4)$$

is measured for a single absorbed photon. This voltage output is then digitized and the number of detected events for each digital step (channel) is then analyzed with a multi channel analyzer (MCA). A counts per channel spectrum is shown in figure 3.14.

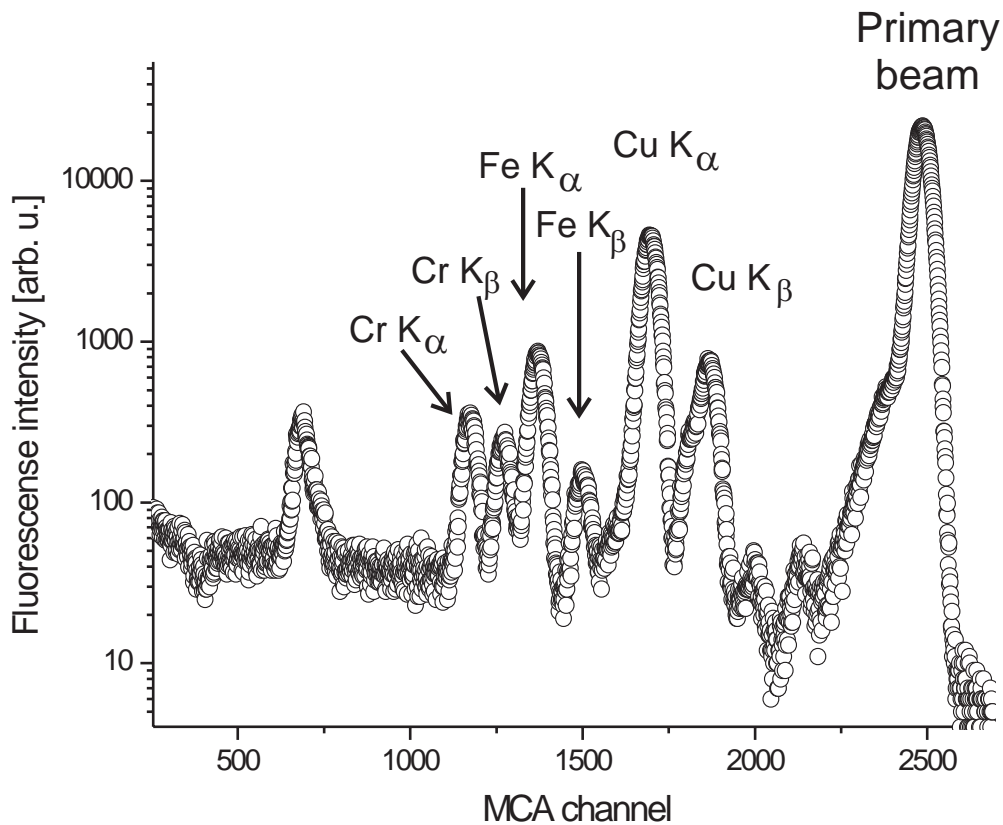


Figure 3.14: Spectrum obtained with an energy dispersive detector. Here a sample holder made of steel was illuminated by a $E = 12\text{keV}$ x-ray beam. By identifying the fluorescence radiation of the elements in the steel alloy, the channels can be calibrated.

To calibrate the channels of the MCA to a photon energy, fluorescence lines of known samples are measured and, using equation 3.4, are linearly mapped to photon energy. After calibration, a certain energy bandwidth can be integrated and displayed in the so-called region-of-interest. The key features of the Roentec XFlash 1001 SDD detector used in this thesis are listed in table 3.3:

active area	$5mm^2$
silicon thickness	$300\mu m$
electronically limited count rate	10^6 counts per second
energy resolution	$245eV @ 500kcps @ MnK_\alpha$
detector temperature	$-10C$

Table 3.3: Characteristics of the Roentec XFlash 1001.

3.3.2.2 Si(Li) detector

The working principle of this Si(Li) type of detectors is again based on the excitation of electron-hole-pairs in a silicon semiconductor. The detector type used during the thesis (Eurisys Mesures (France)) was provided by beamline ID22 at ESRF. It consists of a 4.2 mm thick x-ray active silicon semiconductor placed between two Au electrodes (see Fig. 3.15). To reduce absorption, the Au electrode on the photon entrance side is thinned down to 20 \AA . A voltage of about $500V$ is applied between the electrodes, allowing the separation of the x-ray induced charges (see also section 3.3.2). Behind this detection head a transistor circuit amplifies the collected charges. Both, detector head and transistor are kept at liquid nitrogen temperature to reduce the thermally induced charges to an acceptable level. Close to room temperature no discernable signal could be detected since the noise level would be too high.

active area	$12mm^2-200mm^2$
electronically limited count rate	10^6 counts per second
energy resolution	$145eV-205eV @ 1000cps @ 5.9keV$
detector temperature	$-200C$

Table 3.4: Main properties of the Eurisys Mesures Si(Li) detector heads. The energy resolution depends on the used plus processing unit and on the used detector head (see active area).

The energy resolution of this Si(Li) type of detectors is in the same range as for the SDD as well as the linear count rate. The biggest advantage of Si(Li) type detectors is an improved signal to noise ratio compared to the SDD. A disadvantage is the necessity to provide liquid nitrogen for cooling, which makes the operation

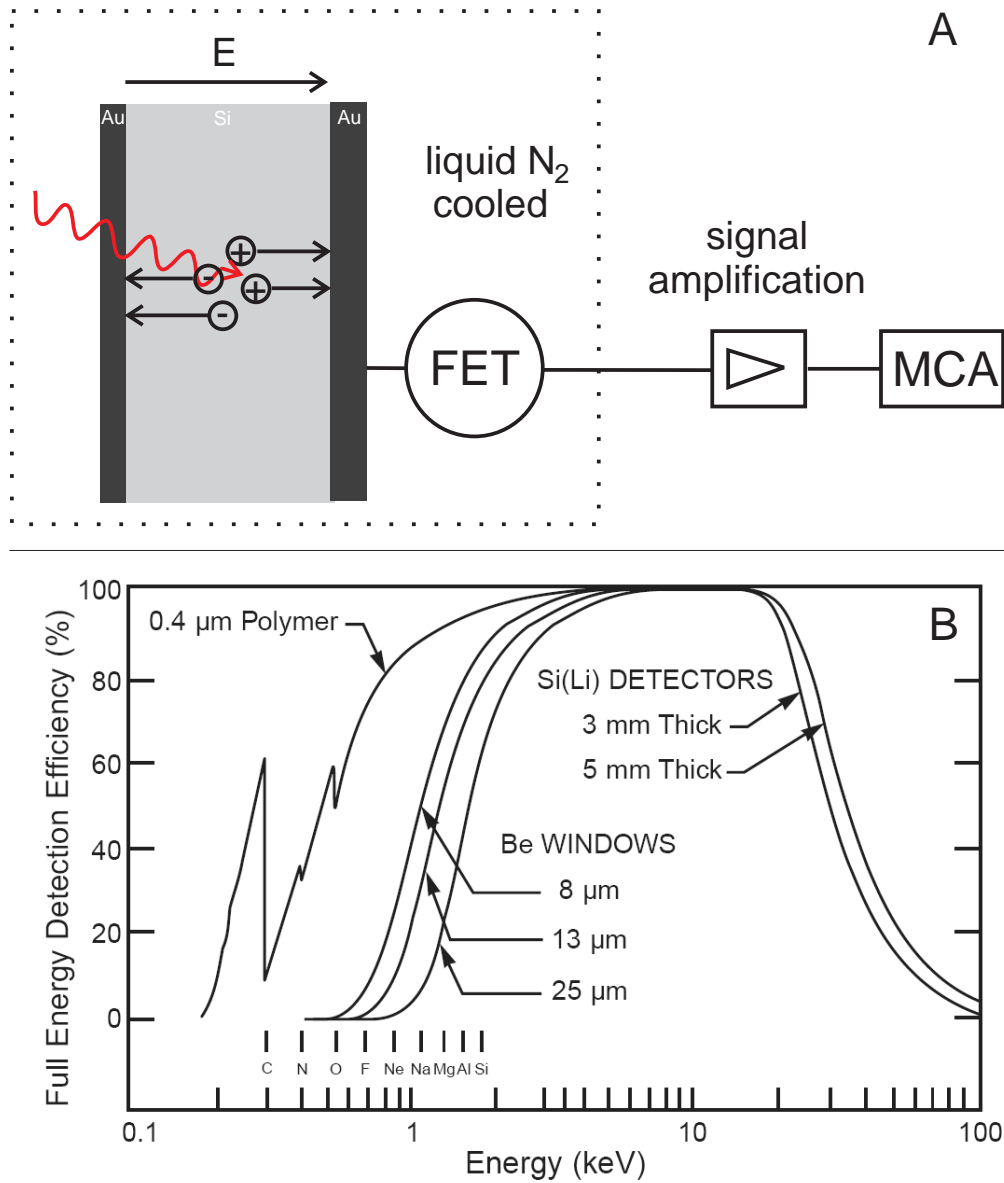


Figure 3.15: **A** The 4.2mm thick x-ray active semiconductor material is sandwiched between Au electrodes. The collected charges are amplified and transferred to the MCA for further processing. **B** Detection efficiency versus detected energy for a typical Si(Li) detector (here a Canberra 2026). As was the case for the CCD, the low energy efficiency is limited by the Be-window transmission while the high energy efficiency is limited by absorption.

expensive and cumbersome.

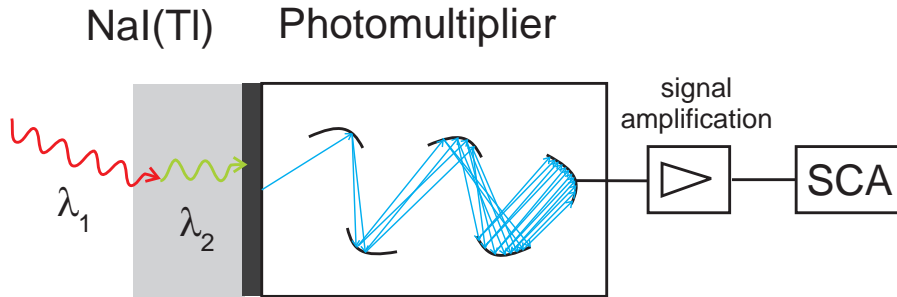


Figure 3.16: The incoming x-ray photons (λ_1) are converted to visible light (λ_2) in the NaI(Tl) scintillator crystal. The visible light is then transformed to an electronic signal and amplified in the photomultiplier. Depending on the energy of the incoming photons the single channel analyzer (SCA) is calibrated to produce one digital pulse per detected x-ray photon.

3.3.3 Point detection

For the alignment procedures (see section 4.2) a scintillation point detector (Cyberstar, Oxford Danfysik, UK) is used. As shown in figure 3.16, it consists of a scintillation crystal (NaI(Tl)) converting x-ray photons to optical ones. The latter are then amplified in a photomultiplier cascade (see also [cyb]). The scintillator crystal is protected by a $200\mu\text{m}$ thick beryllium window. The main properties of the NaI(Tl) scintillation foil are shown in table 3.5:

crystal thickness	1mm
peak scintillation wavelength	410 nm
glow decay constant	$0.23\mu\text{ s}$
absorption @ 20keV	$\approx 99\%$

Table 3.5: Main properties of the NaI(Tl) scintillation crystal used in the cyberstar detector head.

The glow decay constant for the scintillation material limits the maximum count rate of the detector. Although about 10^6 photons per second are detectable with a NaI foil, electronic effects limit the linear range to some 10^5 photons per second. Since the efficiency of the whole system is far above 90% up to about 20keV this type of detector is widely used.

3.4 Implementation

The properties of the needed motors and detectors are described above, but several practical problems have to be solved to get the instrument working. Since the idea of the MoWaSt setup is to install all hardware within only a few hours at a synchrotron, a lot of effort has been taken to keep the setup as simple as possible for the user. In the following section major problems of implementation and their solutions are described.

3.4.1 Computer network

To reduce cabling during build-up of the setup at a beamline, the control computer and all motor controllers are installed in the experimental hutch. This allows to reduce the cabling to only a few meters, testing of all motors after installation, easy setting of motor limits and rough alignment of the setup, e.g. with the help of an adjustment laser. In beam operation mode it is of course not possible to run the setup from inside the experimental hutch. Therefore a computer network is installed at the beamline, where one network cable is needed to connect the instrument control computer with its clients. The desktop of the instrument control computer is exported via network to a client computer in the control room. In Figure 3.17 one out of several possibilities for the MoWaSt beamline network is sketched.

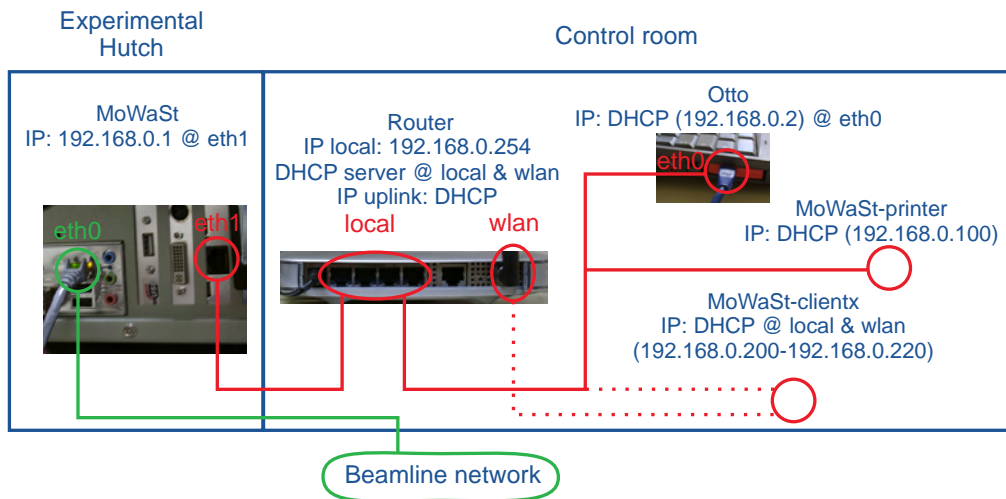


Figure 3.17: Layout of the instrument network. Only one network cable is needed to run the system from the control room. All other cabling is done in the experimental hutch.

This way of connecting the computers at the beamline provides several addi-

tional advantages: As we will see later (3.4.2) it allows for the synchronization between the SPEC motor-control-software and the CCD acquisition software. If the network is additionally connected to the native beamline network, it is possible to run beamline provided hardware in the MoWaSt's SPEC session. The MoWaSt control computer can be used as file server for all computers in the network and only one beamline provided IP-address is needed for all computers of the setup.

At the same time the network can be used for a lot more, e.g. license server for simulation software or interface for additional motor controllers. To make use of this flexibility and modularity it is recommended to have some knowledge of computer networks and Linux configuration. Helpful references here are [Lin, Sou] and the links and newgroups therein.

3.4.2 CCD - Motor synchronization

To be able to take CCD frames depending on motor positions of the MoWaSt setup and to be able to scan with the CCD as detector, it was necessary to implement the possibility of sending trigger events from the SPEC instrument control software to the CCD. To realize that, we chose to include the CCD into the SPEC software in a way that is easy to implement, modular and feasible within a few weeks. We are again using the network capabilities for the SPEC software. In Figure 3.18 the connections for the different parts of the CCD setup are described.

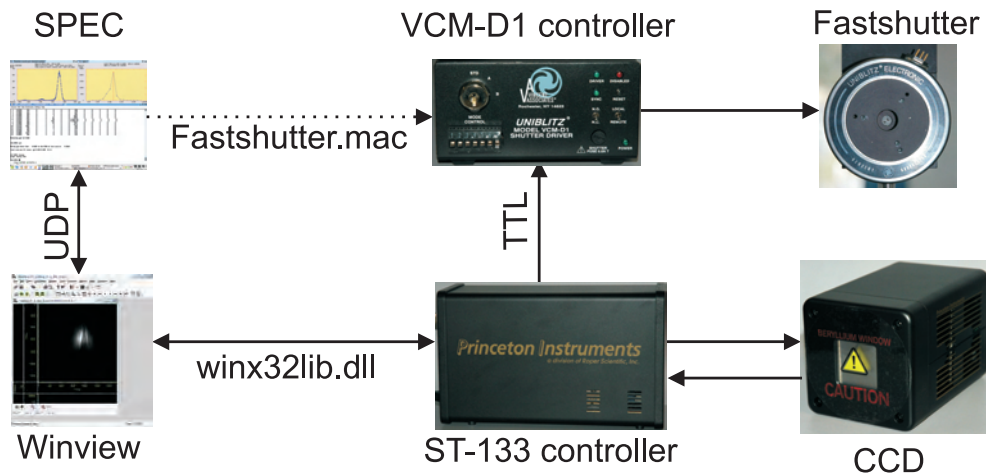


Figure 3.18: Sketch showing the connections between SPEC, Winview and the hardware

The Princeton Instruments LCX-1300 CCD is controlled by the ST-133 controller, which is connected via TAXI interface to a PCI interface card accessible un-

der Windows XP with the WinView CCD acquisition software. A stand-alone-setup of the CCD thus consists of the windows PC connected to the ST-133 controller, which has access to the CCD. This software package provides a dynamically loadable library (dll) usable by any Microsoft .net programm. We chose to program a small UDP server application (Microsoft .net Visual Basic), which is able to control the most common features of the WinView software through the winx32lib.dll (see Appendix A.1 for source code). As described above (see section 3.3.1) the LCX-1300 chip has a full frame architecture and thus needs an external shutter. We chose to include a UNIBLITZ (Rochester, NY, USA) XRS6 fastshutter into the setup. It has a 6mm wide aperture, which can be closed magnetically with a Pt/Ir-alloy blade (x-ray transmission $\ll 10^{-14}$ up to $20keV$) within 3.2msec with up to 50 repetitions per second. It is controlled by a VCM-D1 UNIBLITZ controller. As sketched in figure 3.18 this controller is connected to the ST-133 CCD controller via a standard BNC cable using a TTL (5V, active-high) signal as trigger event for opening and closing the shutter. As an option it is possible to open and close the fastshutter directly from SPEC via a RS232 connection and with the help of a small macroset called fastshutter.mac. This allows opening the shutter permanently during point detector operation of the system. In CCD operation mode of the system the UDP server is accessed by a SPEC macroset (see Appendix A.1 for source code) representing the client side.

3.4.3 SDD implementation

As described in section 3.3.2 an energy dispersive silicon drift detector system can be used to detect fluorescence photons during scanning. Although the SPEC software supports low level communication to multi channel analyzers (MCA) such as the Roentec SDD, neither user-friendly commands nor a standardized data display was available.

Again a macroset was developed to access the roentec detection system via all standard SPEC commands, to allow user-friendly configuration of the detection system, to provide a rough energy calibration and to display and save the MCA data in reproducible manner. The source code of this set of macros can be found in appendix A.2. Since all MCA devices need a comparable software environment, it was possible to adapt the Roentec macroset for the silena Si(Li) detector at the ID22 beamline.

3.5 In-House setup

A dedicated in-house setup for the MoWaSt instrument is conceptually sketched in the following. It can be used i) to train new users on the instrument, ii) to test new hard- and software under 'real' conditions and iii) to perform in-house waveguide experiments. In the latter case, one can think of phase contrast applications as described in [LCC⁺97a], applications making use of the white beam properties as described in [FOKS06] or waveguide enhanced scattering applications comparable to [PMS02].

The in-house beamline setup as planned (and in parts already realized) today is shown in figure 3.19:

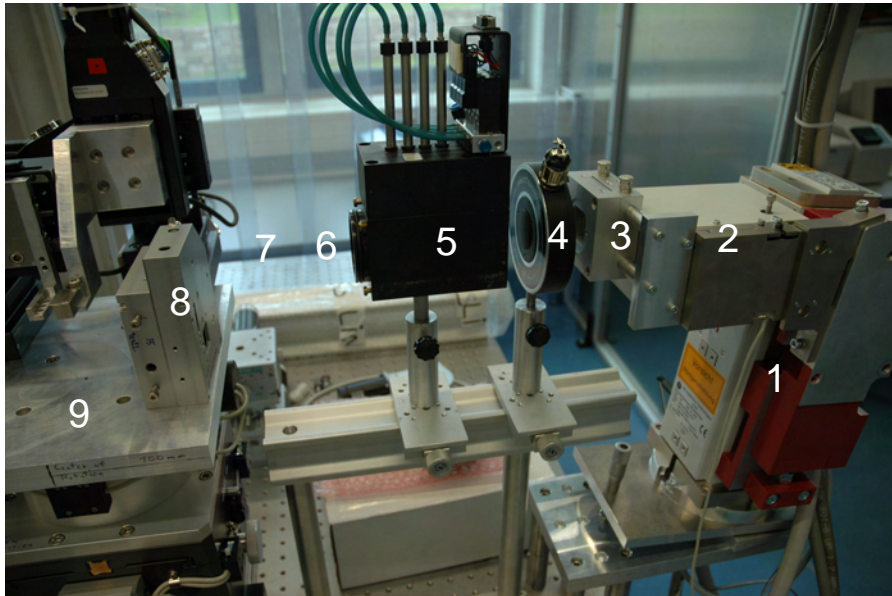


Figure 3.19: Image of the in-house beamline setup during build-up. From right to left: **1** The tube with the 2.2 kW Cu $12\text{ mm} \times 0.4\text{ mm}$ anode **2** Curved multilayer mirror for monochromatisation and collimation in one dimension **3** Manual driven slitset **4** A fastshutter with 14 mm aperture **5** An attenuator box **6** A monitor detector (to be installed) **7** An alignment laser (to be installed) **8** a beam defining slitset (to be mounted) **9** The MoWaSt main tower.

The copper anode (2.2 kW , GE inspection technologies, Germany) with a line focus of $12\text{ mm} \times 0.4\text{ mm}$ is combined with a curved multilayer mirror (more than 75 layers of Ni/C with a mean period of 4 nm) reaching about $10^7 - 10^8\text{ photons/second}$ in a $1\text{ mm} \times 1\text{ mm}$ (semi-)parallel beam. The installed fastshutter (Uniblitz XRS14, Vincent Associates, USA) allows to use the full beam width while working with the CCD as described in 3.4.2. The pneumatically driven attenuator box (PF4, XIA,

Ca, USA) is necessary while working with a point detector (see also section 3.3.3).

Chapter 4

Experiments

In this chapter the experiments performed with the instrument described in the previous chapter are presented. Starting with a general description of the ID22 beamline at the European Synchrotron Radiation Facility, a description of the major steps during installation of the instrument and the alignment of the waveguide structures is given. The nanometer-sized and coherent beam exiting these x-ray waveguides can be used to perform scanning fluorescence and holographic imaging. The corresponding experiments are presented in this chapter.

4.1 General beamline layout

The experiments shown in this thesis were performed at the ID22 undulator beamline at the European Synchrotron Radiation Facility (ESRF) in Grenoble, France. Several experiments not discussed here were also performed at other beamlines [OFJS05, FOKS06, MOF⁺04, OFS05]. In the following section the ID22 beamline layout is described. Although the exact values for the beam-properties (x-ray energy and spot-size of the focusing optics) varied during the different beamtimes presented here, a general description of the beamline can be given. For clarity, the exact values given in this section are mentioned for the experiments described in sections 4.4, 4.5 and 4.6.

The beamline ID22 uses two undulators for the generation of x-ray photons. An undulator consist of a linear arrays of permanent magnets, which force the electrons in the storage ring onto an undulated path, emitting x-ray photons into a narrow cone along their travelling direction. A brief but ample description of synchrotron radiation generation can be found in [ANM00]. These undulators deliver a beam

from a source of size $d_h \times d_v = 700 \times 30 \mu m^2$ (horizontal \times vertical) into a cone with $30 \times 20 \mu rad^2$ divergence. The two undulator systems installed at beamline ID22 are: One ex-vacuum undulator (U42) with a magnet period of $\lambda_U = 42 mm$ and one in-vacuum undulator (U23) with a magnet period of $\lambda_U = 23 mm$. Using the software package SRWE obtained from the ESRF ¹, the spectrum of such undulator U23 is simulated as shown in figure 4.1 for different undulator gap sizes.

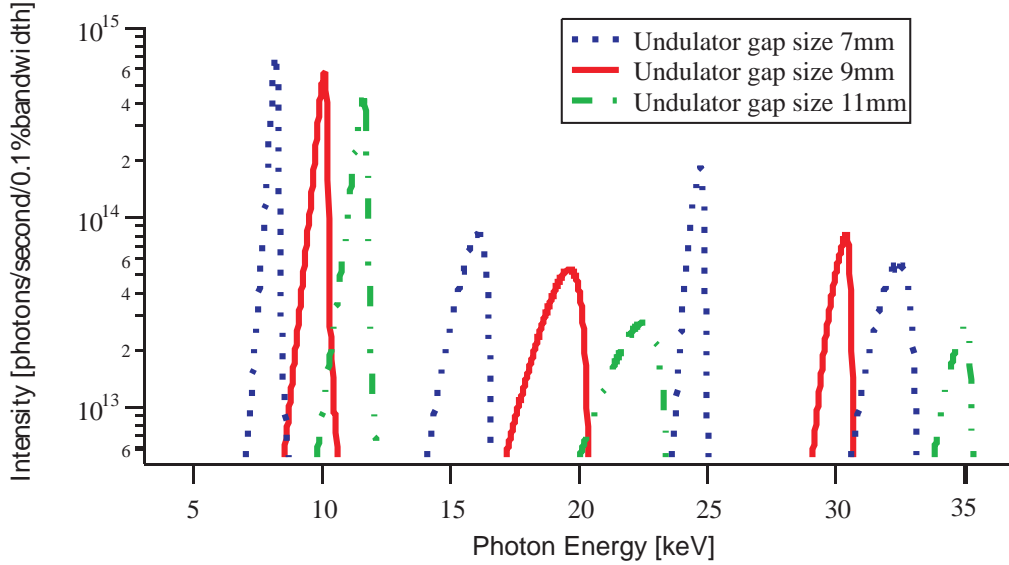


Figure 4.1: In-vacuum undulator spectrum of the U23 ESRF undulator for different gap openings. A monochromaticity of about $\Delta E/E \approx 10^{-2}$ and a significant intensity difference between odd and even harmonics is visible. The spectrum is simulated with the SRWE macro package for Igor Pro from the ESRF.

The energy distribution of the undulator radiation is harmonic and each harmonic has an energetic width of $\Delta E/E \approx 10^{-2}$. The in-vacuum undulator is used with its first or third harmonic and the ex-vacuum undulator U42 is used with its third or fifth harmonic, depending on the energy.

For monochromatisation and suppression of high photon energy contributions additional optical elements are needed. At the ID22 beamline (as for most beamlines) a combination of mirrors and monochromator crystals is used as sketched in figure 4.2.

The first optical element after the undulator is a mirror. Its total external reflection depends on the wavelength of the photons, the deflection angle and the mirror material. The ID22 mirror is made of Si with additional Pd and Pt coating.

¹www.esrf.fr

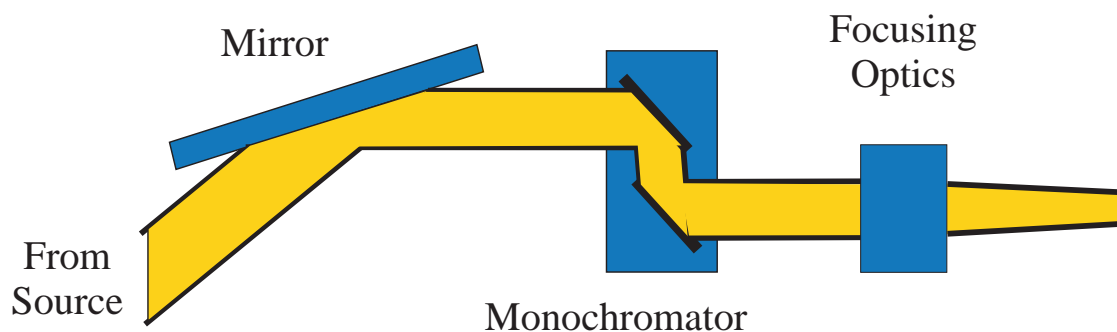


Figure 4.2: The 'raw' undulator radiation is reflected from a mirror, onto two single crystal monochromators and from there onto a beam focusing optic, here two crossed mirrors. Each mirror reflection reduces contributions from higher energies, while the monochromators reduce the wavelength bandwidth in the beam.

These coatings are laterally separated, so that the user can decide from which of the three materials the beam is reflected by translating the respective material in the beam. The mirror is mounted at a fixed deflection angle of 0.3° . In figure 4.3 **A** the simulated reflectivity of a silicon mirror is plotted for varying photon energy. Above $\approx 12\text{keV}$ the total external reflection ends and the reflectivity suddenly drops, making it possible to reduce higher photon energies in intensity.

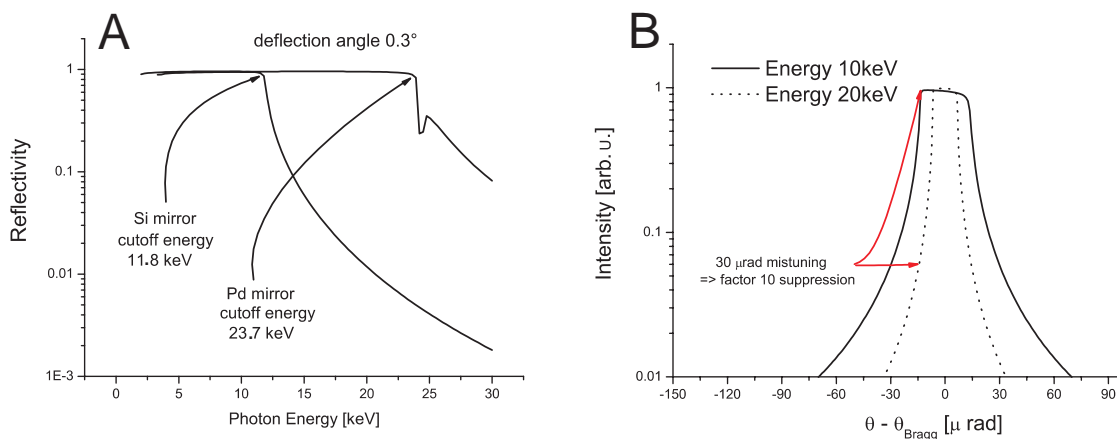


Figure 4.3: **A** Energy dispersive reflectivity of the first mirror in the ID22 beamline. The deflection angle of 0.3 leads to a cut-off energy of $\approx 12\text{keV}$ for silicon and $\approx 24\text{keV}$ for palladium. The reflectivity is simulated using the CXRO database [HGD93]. **B** Simulated (using XOP) rocking curve of the silicon $\langle 111 \rangle$ Bragg peak. The higher energy reflection is much smaller, which can be used to suppress higher order energy contributions in the beam. The monochromaticity reached is $\Delta E/E \approx 10^{-4}$

The beam is monochromatized by two silicon single crystals. The angular position of the first monochromator follows from Bragg's law and the lattice constant for the Si $\langle 111 \rangle$ (3.13 \AA). Using these crystals a monochromasy of $\Delta E/E \approx 10^{-4}$

is reached. Since the width of higher energy Bragg reflections is smaller, the second Si $\langle 111 \rangle$ crystal is slightly detuned from the ideal Bragg angle (within the width of the first Bragg reflection but outside for higher energy reflections), leading to a further suppression of high energy contributions in the beam. In figure 4.3 **B** the rocking curve of the Si $\langle 111 \rangle$ reflection is shown for different photon energies illustrating the behavior described above. Until otherwise mentioned, the experiments presented in this chapter were performed at an x-ray energy of $E = 10.4keV$.

Behind the monochromators the beam enters the experimental hutch with a flux of about $I = 10^{12}photons/second/mm^2$ at a ring current of $200mA$ approximately $42m$ downstream the source. As will be shown later, holographic x-ray imaging and scanning fluorescence experiments demand high photon flux densities (photons/area/second), it is of high importance to increase the flux density with a powerful focusing optics.

In the setup a Kirckpatrick-Baez (KB) mirror [HRC⁺01, HCRM05] design is used, to increase the flux in front of the guide. Two elliptically curved mirrors (focal length of $f_v = 60mm$ for the vertically focusing first mirror and $f_h = 40mm$ for the horizontally focusing second mirror) demagnify the x-ray source into a spot of $\sim 3\mu m \times 5\mu m$. The measured intensity was $\sim 5 * 10^{11}photons/second$, i.e. the gain in photon flux is about 30000. The far-field of the KB mirrors is shown in figure 4.4

To estimate a lower limit for the lateral coherence length $L_T = \lambda \cdot f_h/d_{app}$ in the focal spot of the KB mirrors one can assume, that the mirrors act as completely incoherent source. With an aperture of $d_{app} \sim 300\mu m$ and a focal length of $40mm$ for the horizontal focusing mirror, a lower limit for the transversal coherence length in horizontal direction for an x-ray wavelength of $\lambda \sim 1\text{\AA}$ would be $L_T \sim 130nm$.

To compare the quality of the x-ray beam at a synchrotron beamline, the brilliance B is defined [ANM00]:

$$B = \frac{Intensity[photons/second]}{beam\ divergence\ [mrad^2] \times source\ area\ [mm^2] \times 0.1\% \text{ bandwidth}}. \quad (4.1)$$

This quantity combines the intensity of the source with its natural divergence in horizontal and vertical direction, and its size and normalizes to an energetic bandwidth of 0.1%. In case of the ID22 beamline the brilliance is about $B = 4 \cdot 10^{19}photons/second/mrad^2/mm^2/0.1\%bandwidth$ [Han]. Assuming, that the op-

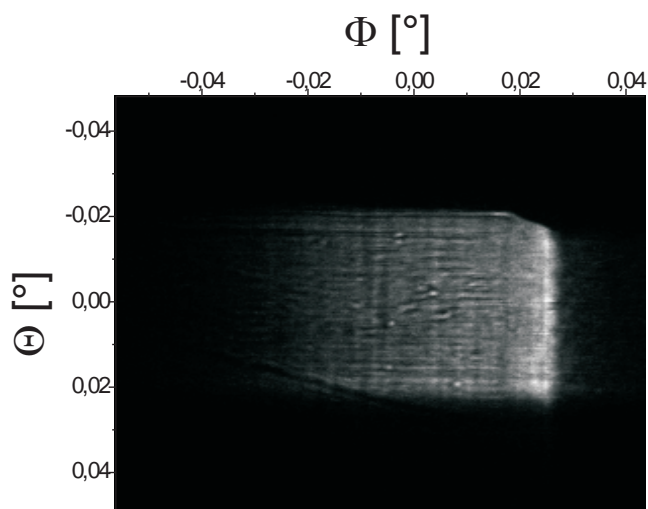


Figure 4.4: Measurement of the far-field of the focussed beam from the Kirckpatrick-Baez mirror system. The visible pattern in the far-field is very likely caused by imperfections on the surface of both mirrors.

tical elements downstream the source do not affect the brilliance², an upper limit for the expected flux in the waveguide far-field can be estimated. Assuming a waveguide with $100 \times 100\text{nm}^2$ guiding core, an efficiency of 10%, and a monochromatic beam with $\Delta E/E = 10^{-4}$ an intensity of $\sim 10^9$ photons per second is estimated as upper limit.

²In fact they will always decrease B, due to limited efficiency!

4.2 Considerations for alignment

Using the focussed and monochromatic beam provided by the beamline as described above, an x-ray waveguide has to be aligned to provide the beam properties needed for the experiments. Since this alignment requires for a precise positioning of sample and waveguide in the focussed beam, the MoWaSt instrument (see chapter 3) is installed at the beamline. After mechanical installation at the beamline is finished, it is necessary to position the pivot-point (sometimes called center-of-rotation, i.e. the intersection of all rotational axes of the instrument) of the rotational stages in the focal spot of the Kirckpatrick-Baez mirrors.

4.2.1 Pivot-point

In figure 4.5 the setup is shown during the alignment.

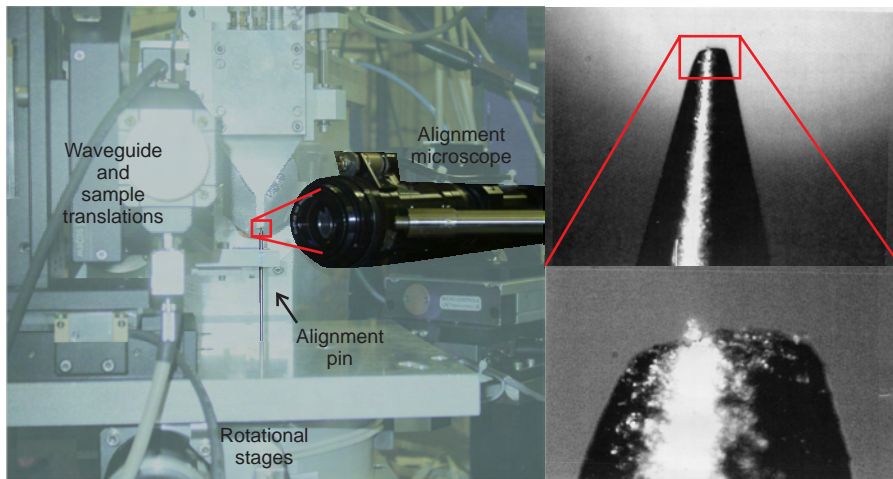


Figure 4.5: The alignment-microscope provided by the beamline, is focussed onto the position of the focal spot of the KB mirror system. An alignment-pin, marking with its tip the pivot-point, is placed onto the MoWaSt instrument. By translating the tip of the pin, with translations below the rotational stages, into the focus of the microscope, the pivot-point can be aligned to the focal spot by $\sim 20\mu m$. The picture is taken looking upstream the x-ray beam.

The optical microscope shown in the figure is provided by the beamline. It is focussed onto the position of the focal spot of the KB mirror system. A pin is mounted onto the main tower, with its tip in the pivot-point of the stages. By translating the tip into the focal plane of the alignment microscope, the center of rotation and the focal spot of the KB mirror system are on top of each other. This

procedure allows to align the center of rotation with a precision of $\pm 20\mu m$, which is sufficient to allow a more precise alignment using the x-ray beam.

4.2.2 Waveguide preparation

As described in chapter 2 the thickness of the guiding core of a typical waveguide is on the order of $\sim 100\text{nm}$. The top cladding layer is approximately 200nm thick. Thus the very intense focussed and $\sim 3\mu m$ broad beam would pass the waveguide unguided and would render the experiment impossible. Also, spurious radiation upstream the focal spot can complicate the experiment. To avoid this, all waveguide wafers are prepared as sketched in figure 4.6:

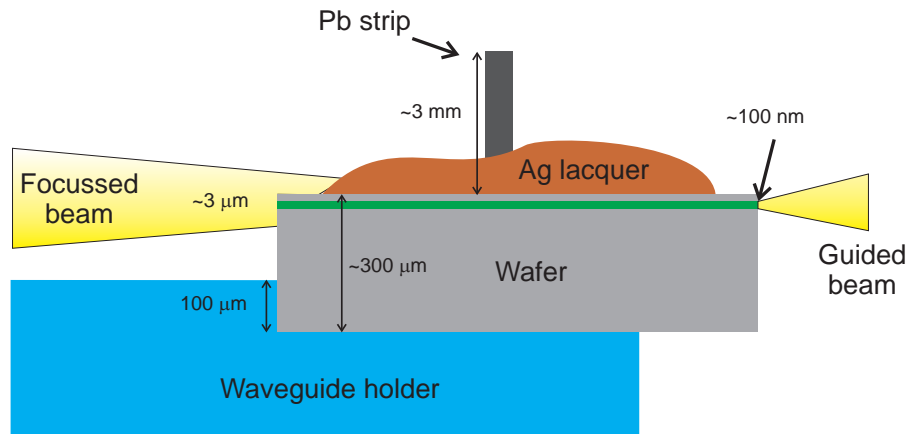


Figure 4.6: On top of the waveguide wafer a leadstrip is glued with silver lacquer. Lead and silver allow to block radiation passing above the guide. To avoid that spurious radiation is passing below the guide, the wafer is mounted on a holder with a $100\mu m$ high step in front of the guide.

The holder, onto which the waveguide wafer is positioned on during the experiment, includes a step of $\sim 100\mu m$ upstream the waveguide, to block radiation, which could pass below the wafer. On top of the adsorbed silicon layer, a strip of lead is glued with silver lacquer to block the radiation passing above the waveguide.

4.2.3 Waveguide choice

The alignment of a single waveguide channel with a size of $\approx 30\text{nm} \times 30\text{nm}$ and an angular acceptance of about 0.1 in a focussed beam of about $3\mu m \times 3\mu m$ requires an elaborate arrangement of numerous waveguides on a single wafer. A sketch of

a typical arrangement is shown in figure 4.7, including the coordinate system used in the experiments.

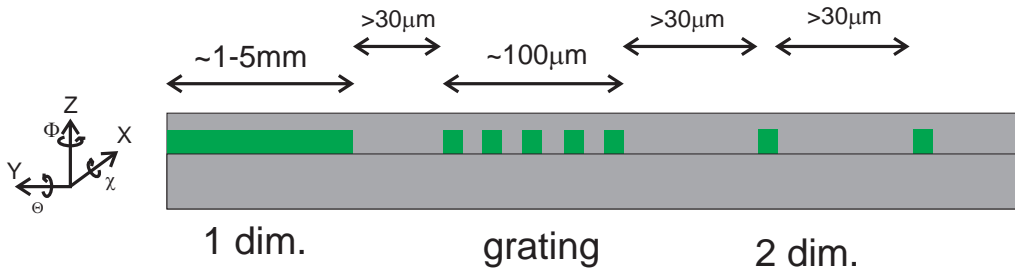


Figure 4.7: To facilitate the alignment of single channel waveguides, the design of a waveguide wafer includes: A one dimensionally confined waveguide for angular and translational alignment in Θ and Z , a grating for rough alignment of the Φ and Y direction and the final two dimensionally confined waveguides separated by a multiple of the incoming beam size.

Most of the angles and translations can roughly be aligned by shadowing the primary beam. The precise alignment is then performed by first aligning a one dimensionally confined waveguide in Θ and Z . By translating the wafer horizontally (Y -direction) a grating structure is illuminated for a first alignment of Φ . The two dimensionally confining waveguides, separated by a multiple of the incoming beam size in Y , require a final adjustment of all angles and translations. To support multiple applications with one setup, several types of waveguides are included on a single wafer. The lateral structure size can be varied, as well as the arrangement of curved waveguides on the wafer. A typical arrangement is sketched in figure 4.8.

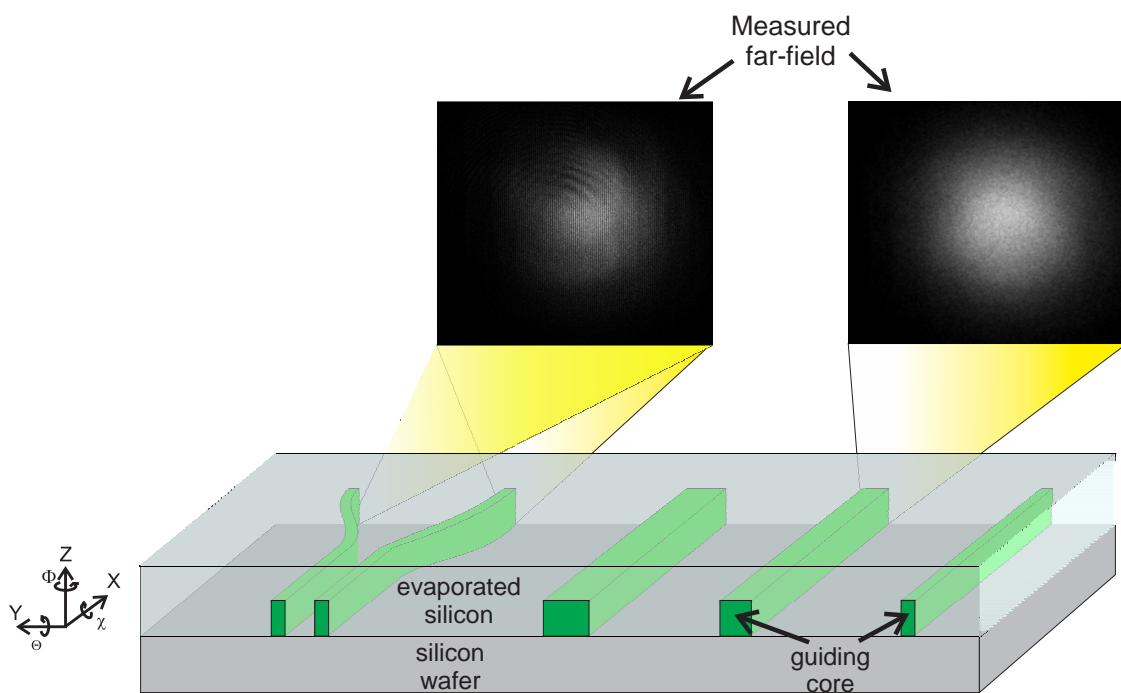


Figure 4.8: Several types of waveguides are structured onto one wafer. Thus, depending on the application, the experimentalist can decide which type of waveguide is used, by translating the respective waveguide entrance into the beam.

4.3 Hard x-ray beam compression to nanometer size

This section presents the experimentally achieved beam properties with a combination of prefocusing optics and single channel x-ray waveguides.

The first experiment showing the feasibility of combining the high gain of a Kirkpatrick-Baez mirror setup with a two dimensionally confining single channel waveguide is published in [JFO⁺05] and was performed at the ID22 beamline described in section 4.1. The x-ray channel waveguide used in this experiment was fabricated as described in chapter 2 with a PMMA core size of $30 \times 70 \text{ nm}^2$ (vertical \times horizontal). It was cut to a length of 4.05mm yielding a transmission of $T = 1.8 \cdot 10^{-7}$ [HGD93] for the incident x-rays. The energy of the x-rays was set to $E = 12.5 \text{ keV}$. The KB mirror system provided a spot of $2.5 \times 3.8 \mu\text{m}^2$ size and an integrated intensity of $7.7 \cdot 10^{11}$ photons/second/180mA in the far-field. Behind the waveguide, $3.6 \cdot 10^6$ photons/second/180mA were detected, corresponding to an enhancement in photon density of ~ 4000 for the combination of waveguide and focusing optics. In figure 4.9 the detected far-field of this single channel waveguide is compared to the far-field of the Kirkpatrick-Baez mirror system.

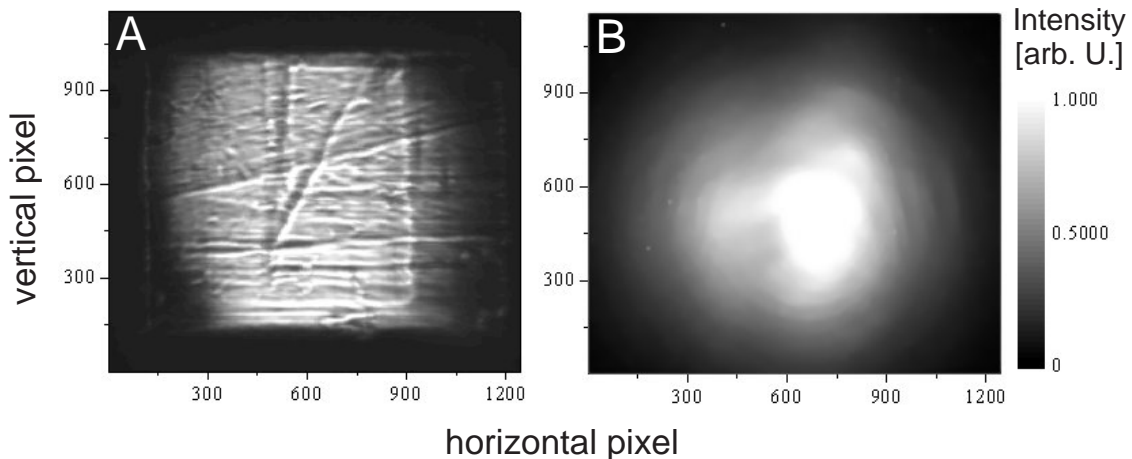


Figure 4.9: CCD images of the beam defined (A) by only the Kirkpatrick-Baez focusing optics and (B) by the combined focusing and waveguiding optics. Both images taken 170 mm behind the focal spot of the KB optics illustrate the filtering properties of the 2D waveguide structure.

While the KB image shows small scale interference fringes, such a fine struc-

ture is not observed in the waveguided beam. The respective far-field profiles were investigated in more detail by orthogonal line scans using a point detector.

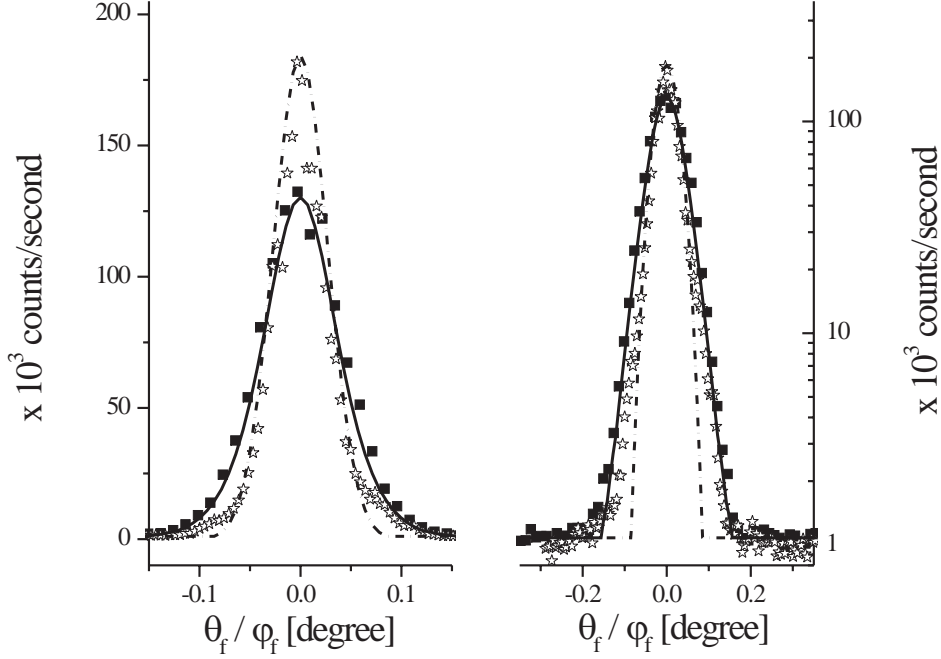


Figure 4.10: Measured far-field pattern of the waveguided beam in vertical (solid squares) and horizontal (open stars) direction, both in linear (left) and logarithmic (right) scales. The lines show the simulated far-field of a two dimensionally confining x-ray waveguide with a PMMA guiding layer of $30 \times 70 \text{ nm}^2$ (solid: vertical, dashed: horizontal). These values correspond to a beam size of $25 \times 47 \text{ nm}^2$ (FWHM) in the near-field and directly behind the two dimensionally confined x-ray waveguide channel structure.

Measured scans through the far-field both in vertical and horizontal direction are shown in Fig. 4.10 (symbols). The lines in the graph represent an integration of the simulated far-field in one direction (corresponding to the perpendicular scan directions). These simulations were performed using the parabolic-wave equation as implemented by Fuhse (see [Fuh06] and chapter 1). The simulations were scaled to the measured intensity, while the scaling factor is the same for both directions. The calculation is in good agreement with the measured data concerning the vertical scan direction, while small deviations are observed between the simulation and the tails of the horizontal far-field distribution. The vertical side length of the rectangular waveguide was 30 nm. This implies guiding of a single mode only, which is not highly sensitive to variations in the incidence angle. In contrast, the horizontal

dimension of the guide was 70 nm, i.e. the guide exhibits multimodal behavior. Slight variations in the incidence angle can explain the deviations in the measured far-field from the simulation.

As will be shown in the following sections, a highly symmetrically waveguide far-field is not necessary to allow for lens-less imaging, but it can simplify the interpretation of the obtained data. In order to enhance the beam properties of the waveguide far-field, two approaches were followed: i) The entrance and exit of the waveguides were polished by the focussed-ion beam technique described in chapter 2 to ensure, that no debris from the cutting process contaminates the beam quality. ii) While lowering the x-ray energy to $E = 10.4\text{keV}$, the length of the illuminated waveguide was kept at $\sim 4\text{mm}$. This lowers the transmission in the silicon cladding to $T \approx 1.35 \cdot 10^{-12}$. It also implies, that the higher order modes propagating in a multimodal waveguide are damped out stronger. To illustrate this behavior, the field distribution inside the same multimodal waveguide³ with 70nm guiding core size (material is a calixarene type resist (see chapter 2)) is shown in figure 4.11 for the two different energies 12.5keV and 10.4keV.

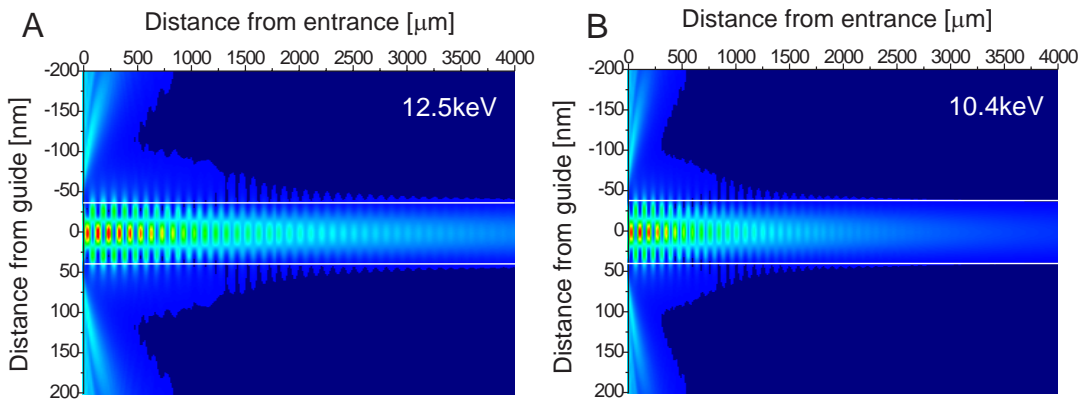


Figure 4.11: Simulated field distribution inside an x-ray waveguide with 70nm guiding layer (calixarene) thickness and a wafer length of 4mm (Si cladding). The simulation on the left is performed for an x-ray energy of $E = 12.5\text{keV}$, while the simulation on the right is done for an x-ray energy of 10.4keV . The higher order modes are faster damped out at lower x-ray energies than the lower order modes.

As visible in the simulations and described in more detail in [FOKS06] the higher order modes are subject to stronger absorption in the silicon cladding. Their

³The simulations were performed for an one dimensionally confined waveguide.

contribution to the waveguide far-field is thus reduced. In figure 4.12 the far-field of the PMMA core $30 \times 70 \text{ nm}^2$ sized waveguide measured at an energy of $E = 12.5 \text{ keV}$ is compared to a calixarene core $30 \times 70 \text{ nm}^2$ sized waveguide measured at an energy of $E = 10.4 \text{ keV}$. The waveguides had a length of 4.05mm and 4.1mm respectively. The CCD camera (SX 1300, Princeton Instruments) was placed 3m downstream the focus of the KB mirror system. Differing from the CCD system described in chapter 3, this camera used a back illuminated full frame chip with a size of $20 \times 20 \mu\text{m}^2$ per pixel. Practically the only difference between both CCD systems (SX1300 and LCX1300) is a reduced detection efficiency of the SX1300 by approximately a factor 3.

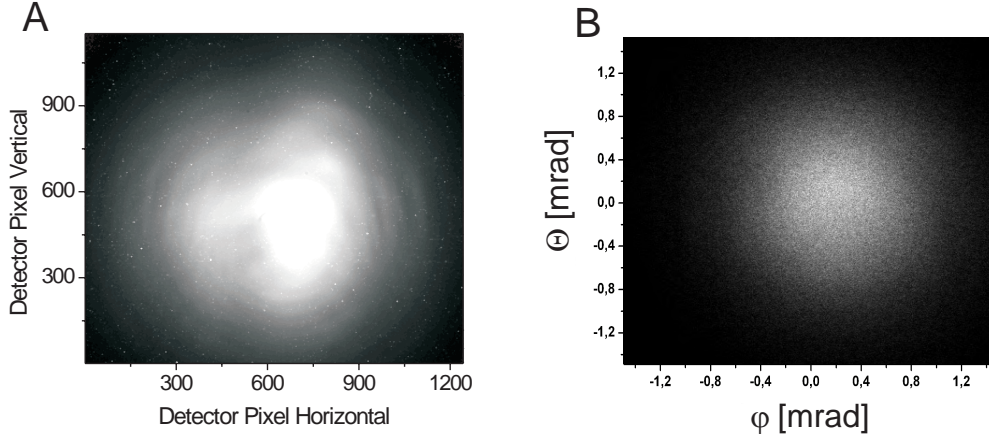


Figure 4.12: Comparison of the far-field of a single channel waveguide at different photon energies. **A** Waveguide dimensions $30 \times 70 \text{ nm}^2$; Waveguide Length 4.05mm; Photon energy 12.5keV. **B** Waveguide dimensions $80 \times 100 \text{ nm}^2$; Waveguide Length 4.1mm; Photon energy 10.4keV. The waveguide illuminated with the lower energy x-rays has a homogenous and symmetric far-field, although it supports more modes.

Although the guiding core dimensions of $100 \times 80 \text{ nm}^2$ (horizontal \times vertical) for the calixarene core waveguide imply a propagation of several modes in both directions the far-field is particularly clean and homogenous. This is due to the fact, that the higher order modes are stronger suppressed for lower x-ray energies (see above) and thus can not contribute to the far-field that much.

It should be mentioned at this point, that a degradation in the far-field shape was observed experimentally. After a few hours in the beam, the far-field shape gets asymmetric and the integrated intensity drops. If the particular waveguide is moved out of the beam, it can be reused after a few hours. After several days of

beamtime, this procedure does not work anymore and the waveguide is irreversibly damaged. Although, beam damage seems to be the reason for the degradation of the far-field, it remains unclear, why the degradation is, at least in parts, reversible. Also, a change in the structure of the guiding core at the beam entrance side should not have a huge effect on the far-field, since the guiding properties at the exit of the guide mainly define the far-field (see also chapter 1 and [Fuh06]). In figure 4.13 the same waveguide is shown, just after alignment and after some hours in the beam.

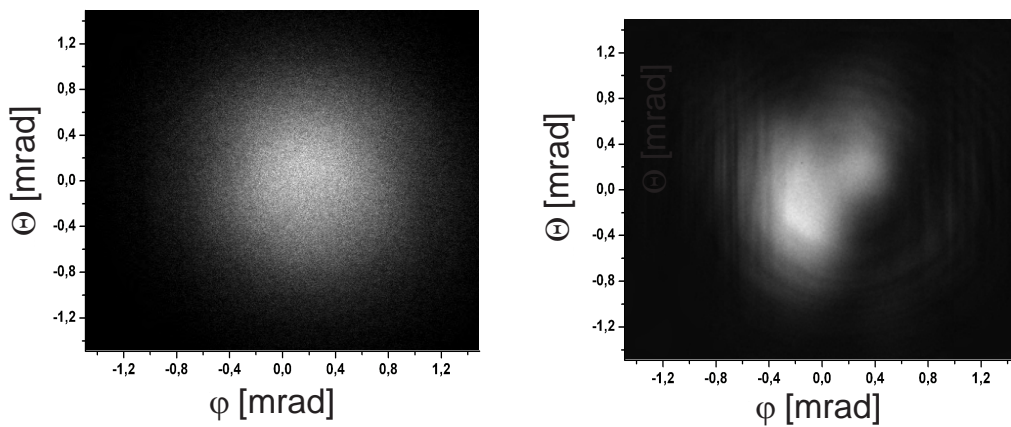


Figure 4.13: Comparison of the far-field of a single channel waveguide. Just after alignment (**A**) and after a few hours in the waveguided beam (**B**). It is clearly visible, that the shape of the beam is not symmetric anymore and it is not possible to realign the wafer, so that the far-field gets again symmetric.

The intensity values measured here are two to three orders of magnitude lower, than the value estimated from the beamline brilliance in section 4.1. Due to a limited efficiency of all optical elements upstream the waveguide, the brilliance of the source can not be transported completely to the waveguide. From the intensity values measured in the focal spot of the KB system, a loss in brilliance of one to two orders of magnitude can be estimated. Thus improving the performance in the optical system can provide half the brilliance needed to reach the theoretical maximum value! Additionally one to two orders of magnitude are lost due to the fact, that the waveguides used here have an efficiency of $\approx 5\%$. To increase this value, one can remove the guiding core polymer as was demonstrated by [See04, PJB⁺05] and/or use a tapered waveguide entrance as described in [Fuh06]. Also, one has to consider the angular acceptance of the waveguide, which is approximately $2mrad$, but can easily vary by a factor 2 when changing the guiding core dimensions

or the guiding core geometry (e.g. for tapered waveguides, see [Fuh06]). For optimal coupling efficiency this value should be matched to the convergence angle of the prefocusing system, which is in our case $\sim 1\text{mrad}$.

4.4 Hard x-ray waveguide scanning fluorescence

Combining x-ray scanning fluorescence with the small beam dimensions presented in the previous section, high resolution scanning experiments are possible. In the following section scanning experiments performed in the slightly divergent waveguided beam with test samples are presented. They show a resolution of below 100nm.

As was presented in section 4.3 the x-ray beam downstream a single channel waveguide is slightly divergent and can have a size of below 50nm in both direction at the exit of the waveguide. As sketched in figure 4.14 a sample can now be placed in this beam. Depending on the distance to the waveguide exit (d_{ws}), the beamsize at the sample position can be chosen due to the beam divergence. A Si(Li) energy dispersive detector (see also chapter 3) is placed perpendicular to the waveguided beam facing the sample. Since the fluorescence radiation, which is to be detected, is emitted in all directions the energy dispersive detector is placed as close as possible to sample. By this way the solid angle covered by the detector aperture is maximized and the collected fluorescence intensity is biggest.

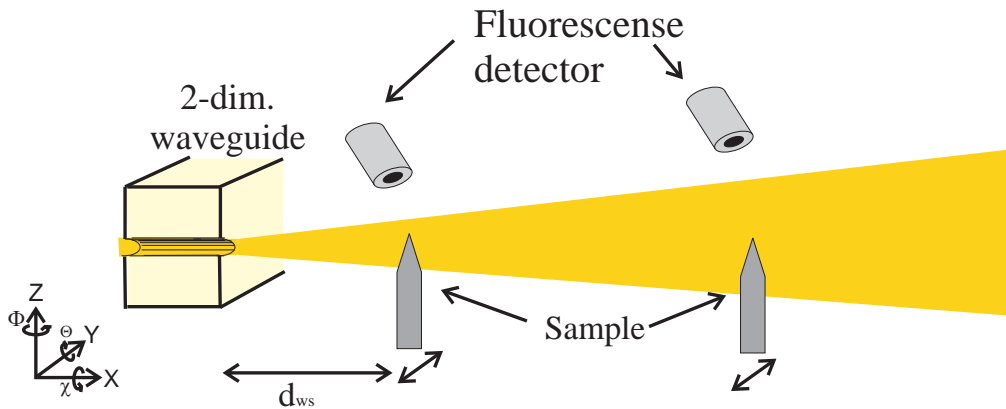


Figure 4.14: Sketch showing the experimental setup used for x-ray waveguide scanning fluorescence. Since the waveguided beam is divergent, the distance from the waveguide exit (d_{ws}) defines the beamsize at the sample position. A Si(Li) energy dispersive detector is placed perpendicular to the x-ray beam direction, allowing to collect fluorescence photons from the sample.

Two different types of samples were used to demonstrate the scanning fluorescence performance of the setup. The first type is a lithographically defined Au structure prepared with the lift-off technique described in chapter 2. The 150nm thick Au structure is prepared on a thinned Si foil with a thickness of 150nm. To allow the excitation of the L_{III} -edge ($E_{L_{III}} \approx 11.9keV$) of Au the x-ray energy was

set to $E = 12\text{keV}$. The Au layer then absorbs approximately 5% of the incident x-rays. This enables the excitation of the L_β transition and produces fluorescence radiation in the Au sample at an energy of $E_{L_\beta} \approx 11.5\text{keV}$. The intensity of this radiation is proportional to the amount of Au in the beam.

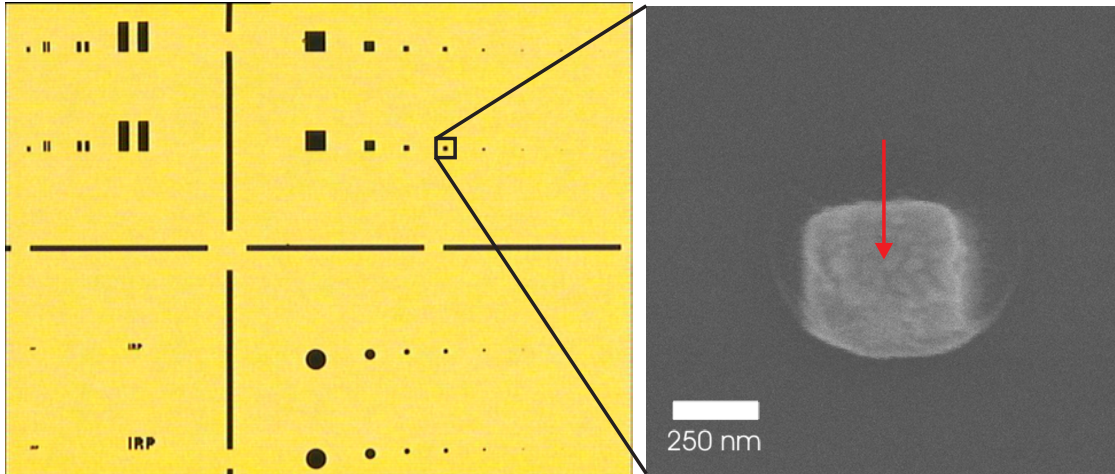


Figure 4.15: Color-coded optical micrograph of the Au sample used for scanning fluorescence. The dark area corresponds to the 150nm thick Au. In the inset a SEM image of one of the smaller Au squares is shown. The arrow indicates the scan position of the fluorescence scan shown in figure 4.16.

In figure 4.15 an optical micrograph and an SEM of the sample is shown. It is also indicated, how the sample was scanned through the beam. During these scans the fluorescence intensity in the energy region-of-interest, i.e. close to the Au L_β emission, is integrated and displayed. In figure 4.16 a scan of the sample at a distance of $d_{ws} \approx 160\mu\text{m}$ behind the waveguide exit is shown. By fitting the measured intensity step with an error function, a FWHM of 188nm is determined. This value can be used as an upper limit for the resolution, since the width of the intensity step is a convolution of the beamsize and the shape of the sample itself. Thus, if the edge of the sample is assumed to be a perfect step, the FWHM value is only determined by the beam size.

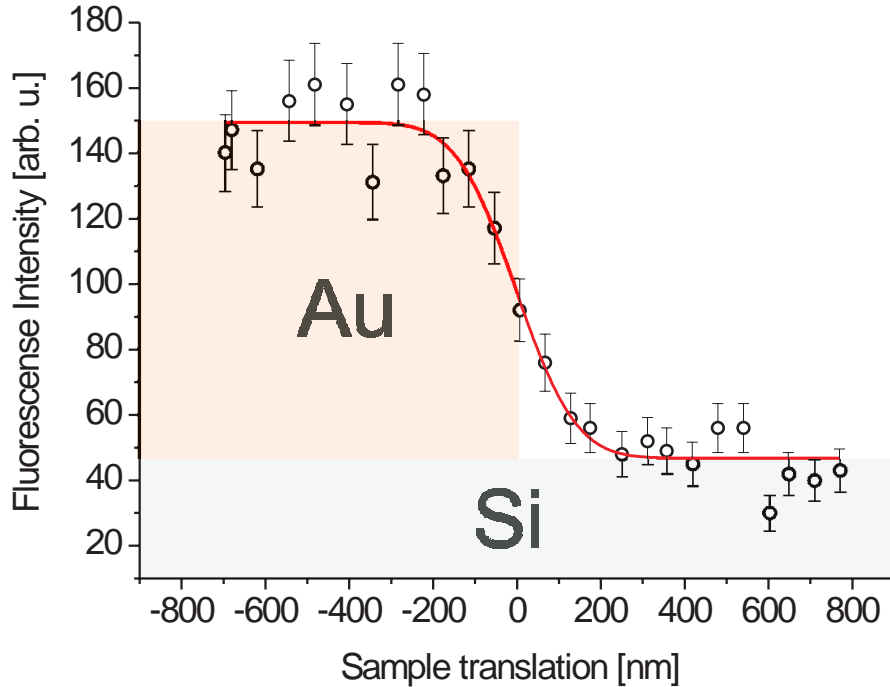


Figure 4.16: Fluorescence scans of the Au sample in the waveguided beam at a distance of $d_{ws} \approx 160\mu m$ behind the waveguide exit. An error function fit shows a FWHM of 188nm. Assuming a perfectly shaped sample, this value should correspond to the FWHM of the beam and thus represents the resolution.

Due to the divergence of the waveguided beam, highest resolution can only be obtained by approaching the sample as close as possible to the waveguide exit. Since the wafer and the lift-off sample have a lateral length of a few mm, slight misalignment can inhibit the sample from getting directly behind the guide. Figure 4.17 shows the lift-off sample in the position, where the scan from figure 4.16 was performed. It can be seen that the sample is nearly hitting the waveguide wafer on the left, while still some space is left at the scanning position. To avoid this, either the sample or the waveguide itself can be reduced in lateral size.

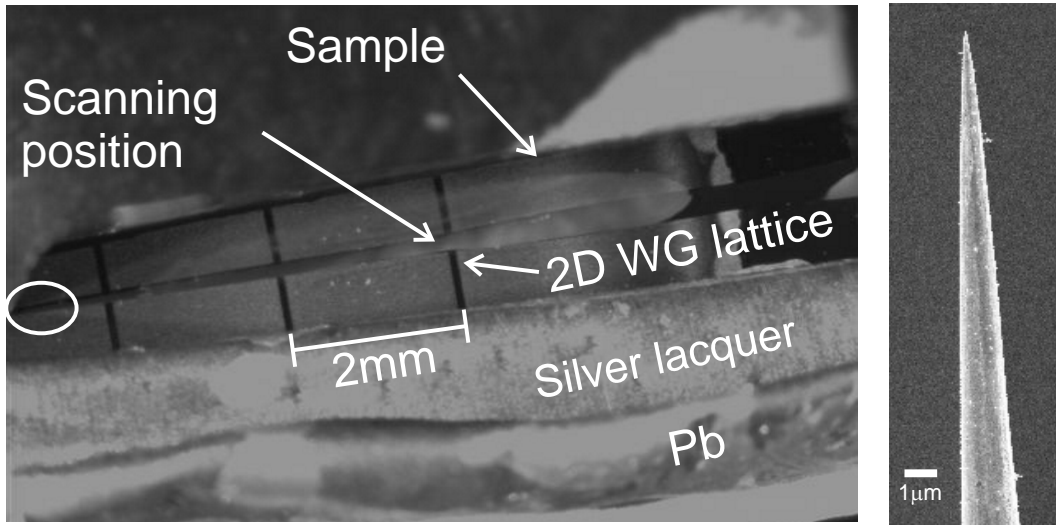


Figure 4.17: Image taken with the video microscope showing a sample close to the waveguide exit. The waveguide lattice structure, which is visible on the waveguide, is mirrored on the sample. Due to angular misalignment, the distance between the waveguide wafer and the sample holder increases from the left to right side of the setup shown here. To avoid contact between sample and wafer, the lateral size of the sample can be reduced. In the SEM on the right, a tip of a pin made of tungsten is shown, which can approach the waveguide exit more easily.

To overcome this limitation, a pin made of tungsten was used. It was electrochemically etched down to a topmost diameter of $< 50\text{nm}$ and is typically used in field ion microscopy [DEH⁺04]. From the tip of the pin, the diameter increases to $\sim 80\mu\text{m}$. An SEM of the tip of this sample is shown in figure 4.17. These samples were provided by the Institut für Materialphysik of the Universität $\frac{1}{2}$ of Gießen $\frac{1}{2}$ tingen. To allow for scanning fluorescence, the x-ray energy was set to $E = 10.4\text{keV}$. This allows to excite the L_{III} -edge of tungsten and enables fluorescence radiation at $L_{\beta} \approx 9.8\text{keV}$. Using the same experimental setup as described above, the tip is positioned in the waveguided beam. Its diameter at the beam position was set to be $\sim 10\mu\text{m}$, i.e. much bigger than the estimated beams size (guiding core dimension of the waveguide 100nm). The obtained fluorescence data is shown in figure 4.18.

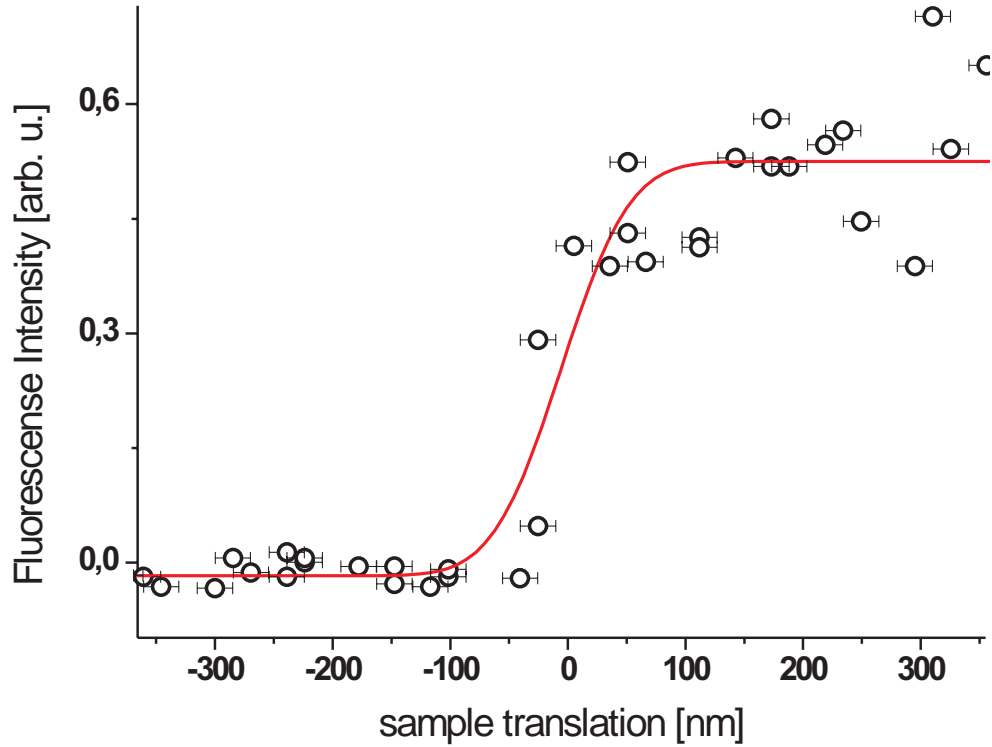


Figure 4.18: Fluorescence scan of the tungsten tip through the wavguided beam. The distance to the waveguide exit can be estimated to be $\sim 30\mu\text{m}$. An error function fit to the data shows a FWHM value of 70nm .

The error function fit shows a value of 70nm for the full width of the step. Approximating the $10\mu\text{m}$ diameter as a sharp step compared to the beam width, the FWHM corresponds to a beam size at the position of the tip. Some movement of the tip was observed, but a FWHM value of $< 100\text{nm}$ was reproducible. Note, that a FWHM value lower than the nominal guiding core size is not contradictory (see [JFO⁺05]).

4.5 Hard X-ray in-line holography

Not only the small beam dimensions can be used to image a sample, but also the waveguide property to only support the propagation of a discrete number of modes, giving rise to a coherent and slightly divergent beam. To apply this x-ray beam to an in-line holography experiment as originally suggested by Gabor [Gab48] and described in chapter 1 is subject of this section.

The experimental setup used to allow for recording x-ray inline holograms is sketched in figure 4.19. The difference to the experimental setup used for scanning fluorescence is only the type and position of the detector as well as the sample position. In other words: The setup does not need to be changed, when changing from scanning mode to holography!

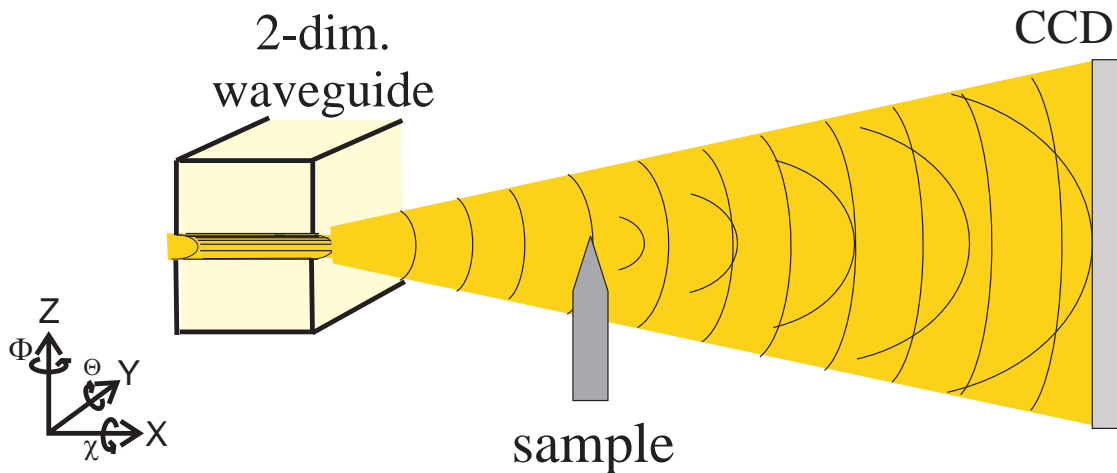


Figure 4.19: Experimental setup used for inline holography. Waves stemming from the sample and undisturbed waves passing the sample interfere at the CCD position and give rise to a hologram.

In order to demonstrate the in-line holography possibilities of the setup, the Au lift-off structures described in chapter 2 are used. The x-ray energy was set to $E = 10.4\text{keV}$, which leads to an absorption of 3% and a phase shift of 0.22 in the 150nm thick Au structures. Thus the sample can be understood as a nearly pure phase object. An SEM of the used sample is shown in figure 4.20. It was positioned $\sim 40\text{mm}$ downstream the waveguide exit. At this position CCD frames were acquired, each frame at a different horizontal position (Y-translation) and with 5 seconds exposure time. These frames can then be combined to one hologram of the sample (see figure 4.20 **B**). This method allows to enlarge the field of view given

by the beam divergence and to increase the signal to noise ratio. In the hologram the large bars in the upper half of the sample are visible but reading the letters is nearly impossible. As described in chapter 1 a reconstruction of the wave in the object plane is necessary. It was performed using an effective defocusing distance of $z_{eff} = 40\text{mm}$. Each single frame was reconstructed separately to reduce computing time, which greatly increases with the number of pixels. After reconstruction, the phase image of the sample is again combined and shown in figure 4.20 **C**.

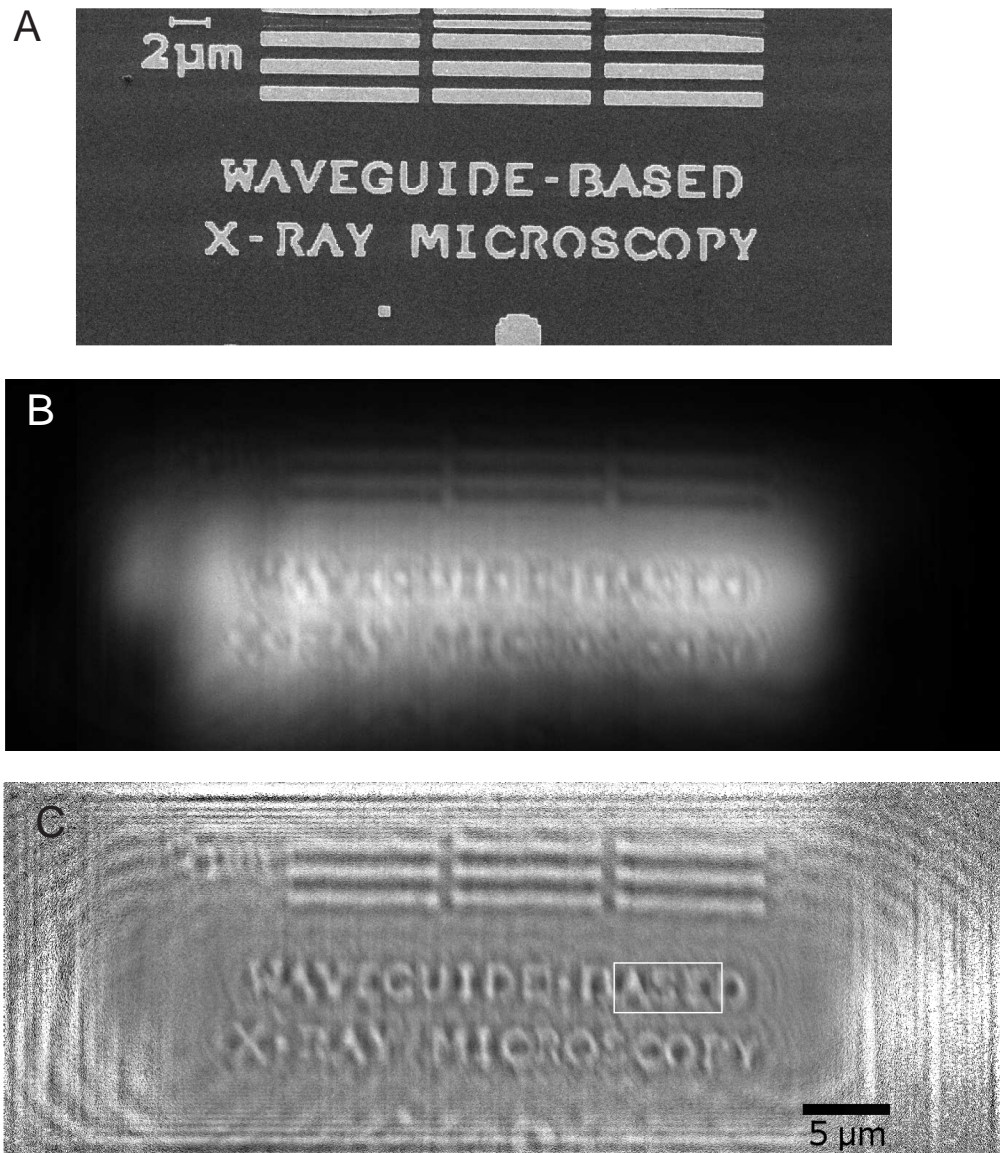


Figure 4.20: **A** SEM of a Au test-sample prepared with the lift-off method described in chapter 2. **B** 12 holograms recorded at different positions on the sample and stitched together. **C** Phase map of the reconstructed direct image of the hologram in **B**.

In the reconstructed phase of the direct image, it is now possible to read the letter structures. Still the image is blurred and circular features close to the reconstructed structures are visible. They can be attributed to the twin image, which is intrinsically included in the reconstruction. To estimate the achieved resolution in the reconstructed image a cut through the images can be evaluated (see figure 4.21).

Along the cut of $1.8\mu\text{m}$ length, five light and dark areas can be distinguished,

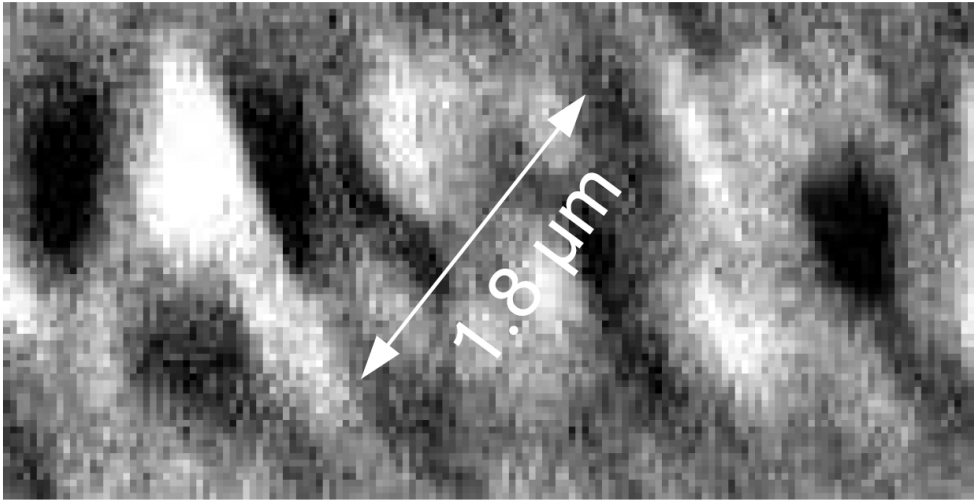


Figure 4.21: Enlarged view of the box marked in figure 4.20. Along the cut through the letter "S" 5 light and dark areas are recognizable, which correspond to a resolution of $\approx 360\text{nm}$.

corresponding to a resolution of $\approx 360\text{nm}$. This is already clearly in the sub-micron range. A resolution comparable to the waveguide core size ($\approx 100\text{nm}$) can not be reached since the image quality is degraded by the twin image. To overcome this restriction, a reference beam holography setup was realized.

4.6 Hard X-ray reference beam holography

In the in-line geometry used in the previous section, a hologram can be recorded and reconstructed, but the reconstructed image will be superposed by the twin image. As described in chapter 1 the twin image can be separated by separating the object and reference wave spatially. In the following section the implementation of such an experiment is shown.

4.6.1 Waveguide design

To provide the necessary illumination with two spatially separated and coherent beams, a special waveguide design is used (see also [Fuh06]). As sketched in figure 4.22, the device is made of two single channel waveguides separated by 100nm at the beam entrance side, which corresponds to the lateral coherence length in the incident beam (see section 4.1). At the beam exit side both waveguide channels are laterally separated by $d_{exit} = 5\mu\text{m}$. This allows to illuminate the sample separately from the reference wave. As described in detail in [Fuh06], bending of a waveguide reduces the efficiency. however, as long as the bending angle is below the critical angle sufficient flux is obtained in the far-field of the waveguides.

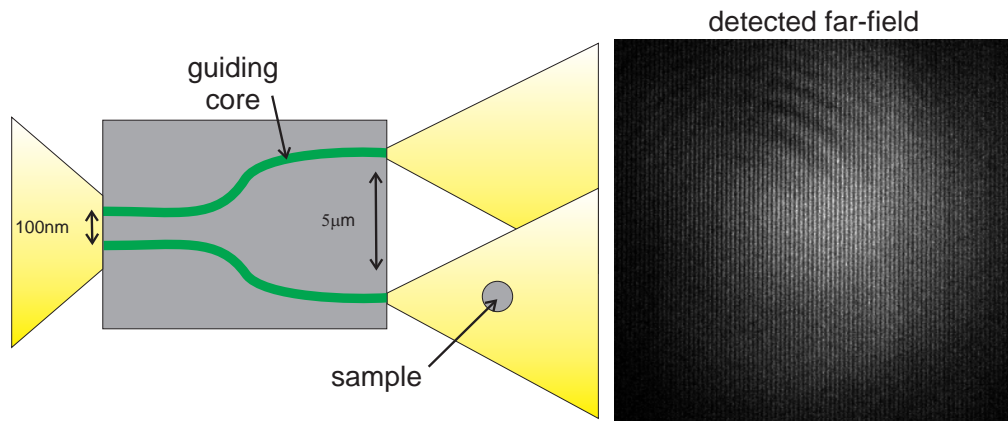


Figure 4.22: To allow coherent illumination in the reference beam geometry, two curved waveguides are used. At the beam entrance side they are separated by 100nm corresponding to the coherence length in the focussed beam. At the exit side the separation is $5\mu\text{m}$. This separation at the exit side gives rise to a Young interference pattern in the far-field. For the used photon energy of 10.4keV the angular separation of 0.024mrad is resolved with the CCD. Note, that the circular structures in the far-field are possibly due to beam damage in the waveguides and can be neglected.

The detected far-field pattern corresponds to a far-field of a single waveguide

channel modulated by a Young interference pattern. To allow the separation of direct image and twin image in the reconstruction, these Young fringes have to be resolved in the detector (see also chapter 1). The angular separation of the fringes is given by $\sin(\alpha_Y) = \lambda/d_{exit}$. For the values used in the experiment ($E=10.4\text{keV}$, $d_{exit} = 5\mu\text{m}$) a separation of 0.024mrad between the fringes is expected. With the used CCD with $20\mu\text{m} \times 20\mu\text{m}$ pixel size positioned 3m downstream the waveguide, this corresponds to a fringe separation of 3.6 pixels. In figure 4.22 a far-field of a double waveguide structure is shown, where the separation of the Young fringes is clearly visible. The maximum separation of both waveguides at the exit is limited by the angular resolution in the detector. For the present setup, the minimal fringe separation of 2 pixels is reached at a waveguide separation of $d_{exit} \approx 9\mu\text{m}$.

4.6.2 Experiment

As sample the tungsten tip described in section 4.4 was used. The tip was positioned in one of the two beams exiting the double waveguide device at an effective defocusing distance of 1.25mm . The recorded hologram is shown in figure 4.23 **B**, where the tip is already visible as shadow.

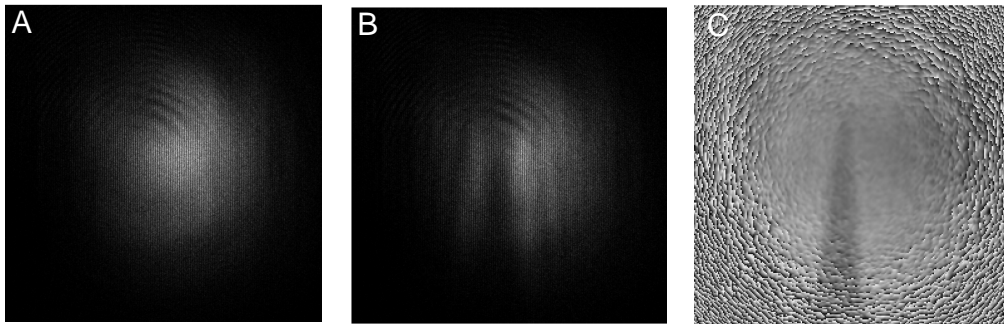


Figure 4.23: **A** Recorded intensity pattern of the double waveguides without the sample. The Young fringes are clearly resolved by the CCD. Acquisition time 10 seconds. **B** Recorded hologram with the tip aligned in one of the guided x-ray beams. Here the shadow of the tip is visible. **C** Reconstructed first order phase pattern of the hologram shown in **C**.

Using the reference beam reconstruction method described in chapter 1 and [Fuh06], a pattern of the phase shift in the object plane can be obtained as shown in figure 4.23 **C**. Here the tip is clearly recognizable. Outside the central region, where the beam intensity was highest, the phase image becomes noisy. In order to enhance the photon statistic in these regions, the tip can be scanned through the

beam and each single frame can then be reconstructed. The obtained phase images of the object plane can then be stitched together. In figure 4.24 the combined reconstruction of three individual holograms shows a large section of the tip.

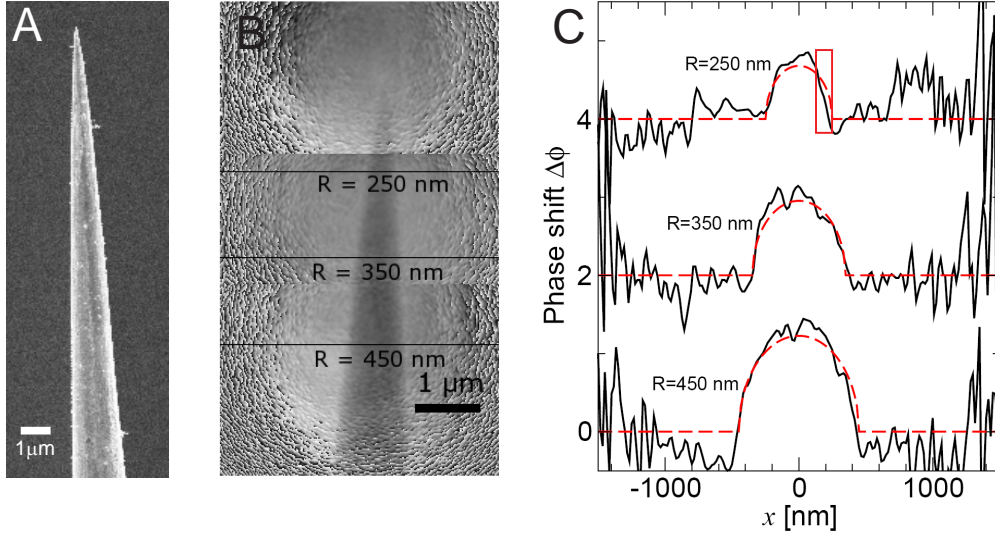


Figure 4.24: **A** SEM of the tungsten pin used as sample for reference beam holography. **B** Combined reconstruction of the phase shift images in the object plane. The tip can clearly be recognized. **C** Cuts through the phase images in **B** compared to the theoretical phase shift as defined in equation 4.2. The red box indicates 100nm.

In figure 4.24 **C** the phase shift along the lines indicated in **B** are compared to the theoretical phase shift calculated from:

$$\Delta\phi = \begin{cases} 2\sqrt{R^2 - x^2}\delta k & |x| < R \\ 0 & |x| \geq R \end{cases} \quad (4.2)$$

Here $2\sqrt{R^2 - x^2}$ denotes the thickness of the (approximately) round tip at position x . At an x-ray energy of $E = 10.4\text{keV}$, $\delta = 2.59 \cdot 10^{-5}$ as tabulated in [HGD93] is used. The comparison shows, that the tip-radii can easily be obtained by this method. The resolution in the image, e.g. for the cut through the tip region with 250nm radius, can be estimated to be $\approx 100\text{nm}$ (see figure 4.24 **B** red box). Since the resolution limit is given by the size of the guiding core of the waveguide used for illumination, a value of 100nm is reasonable.

4.7 Object localization with 10nm accuracy by x-ray in-line holographic imaging

The in-line setup presented above can be used to localize objects far below the imaging-resolution limit. In the following section, the localization accuracy achieved in the experiments is described and compared to simulations.

Using the setup described in section 4.5, a tungsten pin (see section 4.4) is coherently illuminated and the evolving hologram is recorded. At the given sample distance $d_{ws} = 1.6\text{mm}$ and detector distance $d_{sd} + d_{ws} = 3020\text{mm}$ the magnification of the hologram is $M \simeq 1890$. The nominal imaging resolution is given by the beam cross-section at the waveguide exit. From the far-field of the used waveguide a beam width of $\approx 31\text{nm}$ (vertical) and $\approx 44\text{nm}$ (horizontal) can be estimated. In figure 4.25 the waveguide far-field without the sample, the recorded hologram and an SEM image of the tungsten tip is shown.

The pin is translated laterally through the waveguided beam. The translational scan exhibited 21 positions covering a total distance of 300nm. In figure 4.26 the same region on the CCD (see also box in figure 4.25) is shown, for each position in the scan. Each 5 pixel slices was then added up to reduce noise. The position of the central maximum was determined by fitting to a Gaussian (Fig. 4.25 inset). The calibration curve is then obtained by plotting the peak position versus the

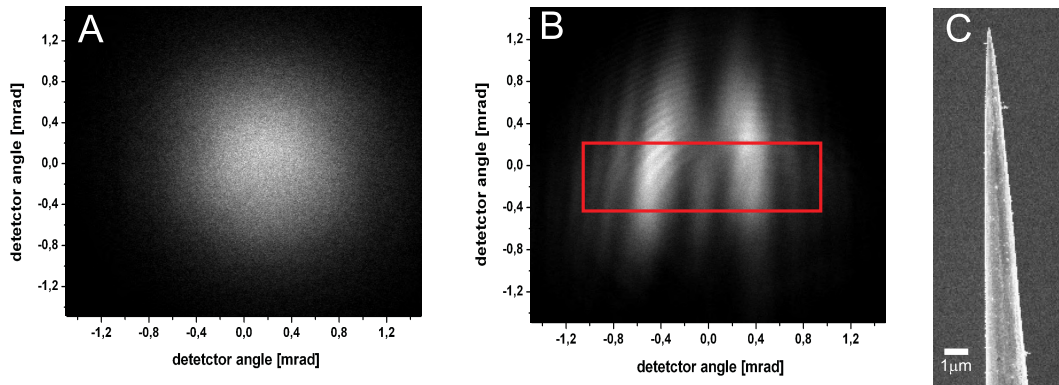


Figure 4.25: **A** Far field pattern of the waveguide without sample. **B** Recorded hologram of the FIM-tip recorded at $d_{ws} \simeq 7\text{mm}$ and $d_{ws} + d_{sd} = 3020\text{mm}$. The highlighted box is further analyzed (see fig. 4.26 and 4.27). **C** SEM image of the tungsten pin.

encoder readings for each frame, see figure 4.27. With fitting errors of the central maximum ranging between 0.5 and 1.5 pixels and a linear slope of 0.0840 pixel/nm (calibration curve) a localization accuracy of around 10nm is achieved.

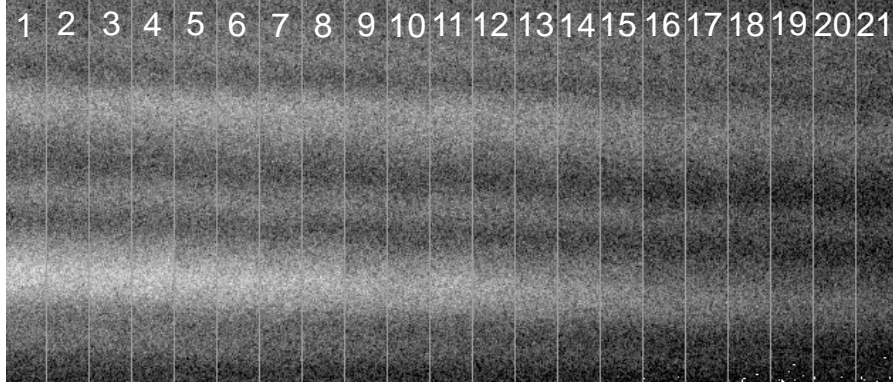


Figure 4.26: Region of interest on the CCD for all 21 positions of the sample in the beam during the lateral scan.

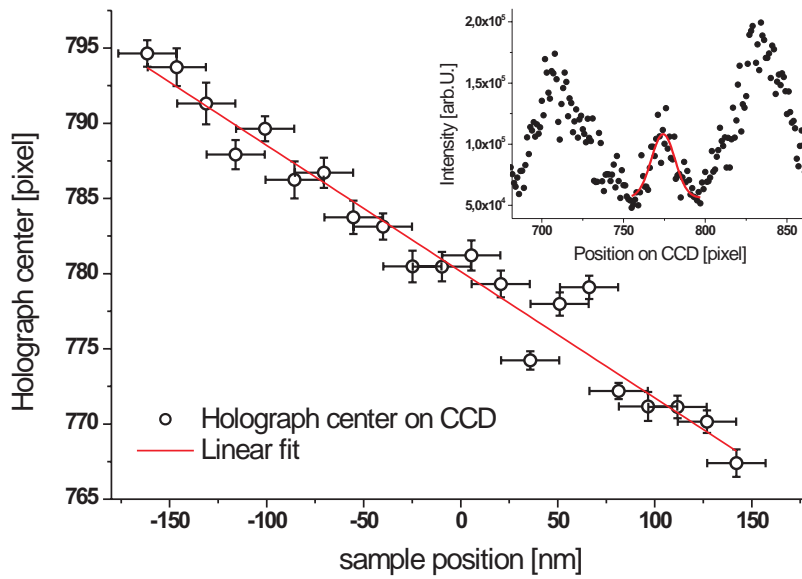


Figure 4.27: Calibration of the lateral sample position by fitting the central peak in the hologram. The error bars represent the errors of the least-square fitting (y -axis) and the encoder precision (x -axis), respectively. The data is linearly fitted obtaining a slope of 0.084 pixel/nm. In the inset, the data obtained from integrating 5 pixel slices (see figure 4.26) is shown. The solid line correspond to an Gaussian fit from which the peak position is determined.

4.7.1 Simulation

Let us consider heavy atom markers for x-ray holographic imaging. In the following we assume spherical gold particles with radius R and density $\rho = 19.3\text{g/cm}^3$. As defined in chapter 1 the imaging resolution Δ is proportional to the waveguide dimension $\Delta \propto d$. Since the presently achievable waveguide dimensions range down to $d \simeq 30 - 50\text{nm}$ (see section 4.3), it would be interesting to use markers of similar or smaller radius R . For $R \leq d$ the intensity distribution on the CCD camera is approximately the hologram of a point source, i.e. the Fresnel zone plate (FZP) pattern [LLT95]. The radius of the zones on the detector appear at $r_n \simeq \sqrt{n\lambda d_{sd}}$, so that the zones all occupy the same area on the detector [Mic86].

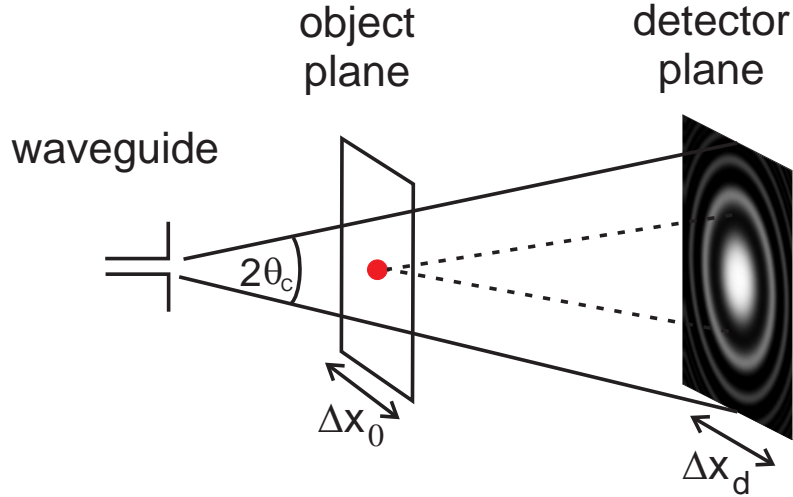


Figure 4.28: Sketch illustrating the geometry used for the simulation.

The intensity minima of the uneven zones are given by the negative interference of the empty beam I_0 with the spherical wave originating from the marker position. Modelling the strength of the marker object as a point-like Thompson scatterer [ANM00], we find

$$I^* = I_0 \underbrace{\left(1 - c \times \frac{R_c^3}{d_{ws}}\right)^2}_r, \quad c := \frac{4\pi\rho_{el}r_0}{3}, \quad (4.3)$$

for the intensity minimum I^* . R_c is the radius of the marker object, d_{ws} is the distance of the object behind the waveguide exit, ρ_{el} is the electron density of the marker object, r_0 the classical electron radius and I_0 the impinging intensity. For

a gold bead with $R = 10\text{nm}$ at a distance of $d_{ws} \simeq 100\mu\text{m}$ this leads to a reduction $r = I_{min}/I_o \simeq 0.998$.

To detect such a weak contrast the Poissonian noise in the detector counts must be smaller than a critical value. To estimate how the critical flux depends on the localization accuracy, let us assume, that image analysis is performed by translating the transmission mask of a FZP pattern to find the most likely lateral position of the marker. Let us consider the relative reduction χ of counts transmitted by a mask shifted from the initial position by a small distance Δx_d on the detector, corresponding to a relative shift of $\epsilon = \Delta x_d/x_d = \Delta x_d/\sqrt{\lambda d_{wd}}$ with $\epsilon \ll 1$. The intensity in areas of maximum I_{max} and minimum I_{min} intensity for the shifted FZP pattern can then be written as

$$\begin{aligned} I_{max}(\epsilon) &= I_0 \cdot x \cdot (1 - \epsilon) \\ I_{min}(\epsilon) &= I^* \cdot (1 - x) \cdot (1 + \epsilon) , \end{aligned}$$

where x denotes the area fraction on the detector for the high intensity region. Thus the relative reduction in intensity χ compared to the unshifted case is given by:

$$\begin{aligned} \chi(\epsilon) &= \frac{I_{max}(\epsilon) + I_{min}(\epsilon)}{I_{max}(0) + I_{min}(0)} \\ &= \frac{I_0 \cdot x \cdot (1 - \epsilon) + I^* \cdot (1 - x) \cdot (1 + \epsilon)}{I_0 \cdot x + I^* \cdot (1 - x)} \\ &= \frac{\frac{x}{1-x} \cdot (1 - \epsilon) + r \cdot (1 + \epsilon)}{\frac{x}{1-x} + r} . \end{aligned}$$

Maximal contrast will be achieved, if the transmission mask is shifted by half the area, i.e. if $x = 0.5$. Then

$$\begin{aligned} \chi(\epsilon) &= \frac{1 - \epsilon + r + r\epsilon}{1 + r} \\ &= 1 + \epsilon \frac{1 - \epsilon + r + r\epsilon}{1 + r} \\ &\stackrel{r \leq 1}{\cong} 1 - \epsilon \frac{1 - r}{2} \\ &\stackrel{\delta := 1-r}{\cong} 1 - \frac{\epsilon \delta}{2} \end{aligned} \tag{4.4}$$

Thus we have to compare the Poissonian noise of $F_0\Delta t$ where F_0 is the integral flux of the waveguide beam and Δt the exposure time, with the reduction in counts $F_0\Delta t(1 - \chi(\epsilon))$ corresponding to a small shift ϵ . The observability condition can then be stated as

$$\frac{1}{\sqrt{F_0\Delta t}} \ll \frac{\epsilon\delta}{2} \quad (4.5)$$

Next we assume that the magnification $M \simeq d_{sd}/d_{ws} \gg 1$ is high and that $d_{sd} \gg d_{ws}$. Assuming that the radius of the first zone of the hologram is on the same order of magnitude as the radius of the far-field pattern on the detector $\sqrt{\lambda d_{sd}} \simeq d_{sd}\text{NA}$, a shift Δx_o of the marker in the object plane is related to the relative shift ϵ of the hologram on the detector by

$$\Delta x_o/(\text{NA } d_{ws}) = \Delta x_d/(\text{NA } d_{sd}) \simeq \epsilon \quad (4.6)$$

Expressing ϵ in terms of the object translation Δx_o , and the contrast $\delta = cR^3/d_{ws}$, where the prefactor c is taken from equation 4.3, the observability condition reads

$$F_0\Delta t \gg N_c = \frac{4 (NA)^2 d_{ws}^2}{c^2(\Delta x_o)^2 R_c^6} \quad (4.7)$$

The critical number of photons N_c of the entire beam for a 1 second exposure and parameters on the order of the present experiment $\text{NA} = 1\text{mrad}$, $z_1 = 1\text{mm}$, $\Delta x_o = 30\text{nm}$, $R_c = 100\text{nm}$ equals $N_c = 4.4 \times 10^5$. This value should be compared to the integral waveguide flux of 3.5×10^6 photons/sec. Thus 10nm localization accuracy for an object with a size of 150nm is not surprising. Correspondingly smaller object sizes in between 10-50nm could become observable at smaller distances $d_{ws} \simeq 10\mu\text{m}$ and higher photon flux F_0 .

For illustration and to corroborate the above scaling argument, we have simulated the hologram of point scatterers including Poissonian noise. The scattering amplitude given by equation 4.3 is superposed with a wave of Gaussian shaped amplitude. This is supposed to model the marker objects in the coherent waveguided beam. The source code of the programm developed for this purpose is given in appendix C. A simulation is shown in figure 4.29.

Fig. 4.29 **A** shows the simulated hologram of a colloidal particle with $R_c = 40\text{nm}$ (at the resolution limit) represented by a point scatterer at a lateral position 50nm

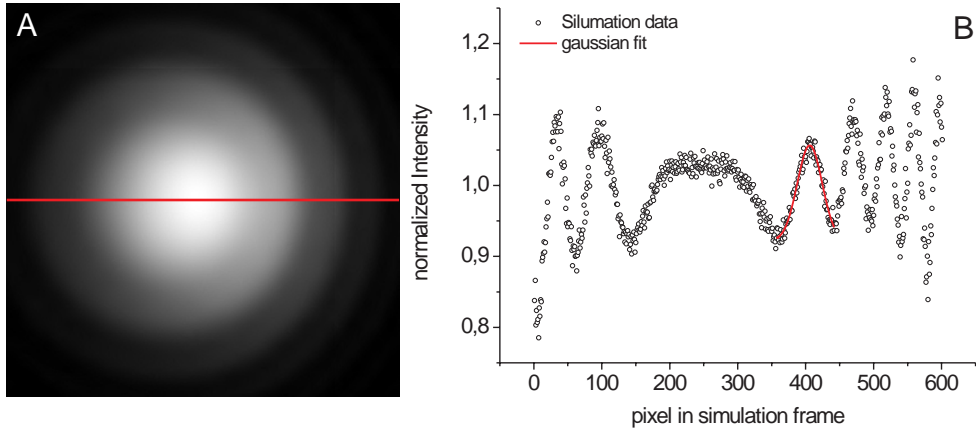


Figure 4.29: **A** Simulation of a gold marker object ($R_c=40\text{nm}$) in a Gaussian shaped ($\text{NA} = 1\text{mrad}$) coherent beam (50 counts in brightest pixel) at a magnification of $M = 10000$. **B** A cut through the simulated intensity along the red line is shown after normalization to an overall Gaussian shape. The first oscillation is localized by fitting to a Gaussian.

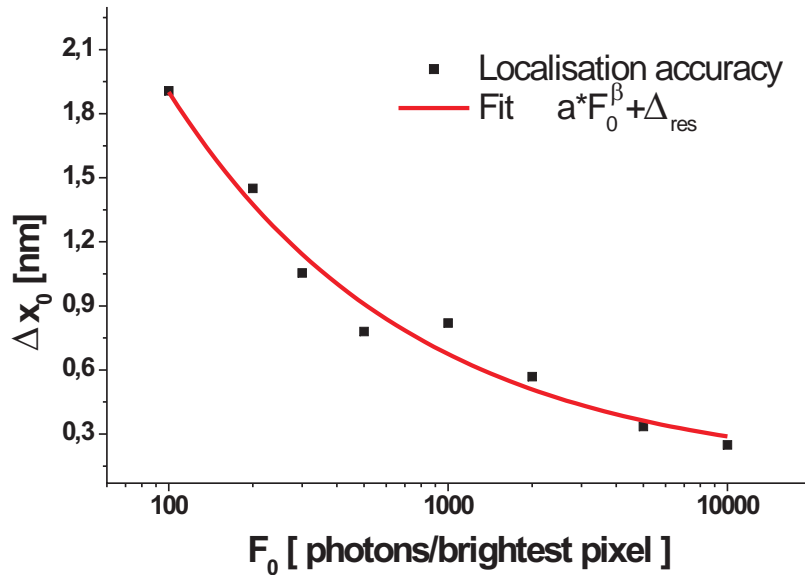


Figure 4.30: **A** Localization accuracy of a marker colloid as a function of beam intensity. The power-law fit confirms the $\Delta x \propto F^{-0.5}$ scaling. **B** Simulated hologram of three Au colloids with $R_c=40\text{nm}$ at a magnification of $M=10000$ and an intensity of 50 photons in the brightest pixel.

from the beam center, simulated for $E = 10.4\text{keV}$, $d_{ws} = 100\mu\text{m}$, $d_{sd} = 1\text{m} - d_{ws}$ and $\text{NA} = 1\text{mrad}$. Poissonian noise is then added to the intensity corresponding to a given maximum intensity per pixel in the center of the Gaussian beam. Next, a slice through the simulated hologram (one particle) is fitted to determine the position of one of the strongest fringes. In figure 4.30, the error of the fitted position is plotted as a function of peak intensity. The solid line is a fit $\Delta x_0 \propto F_0^\beta + \Delta_{res}$, where the residual error is computed from a simulation run without noise. The fitted exponent of $\beta = -0.50 \pm 0.12$ is clearly in agreement with equation 4.3.

4.8 Conclusions

We have experimentally demonstrated that the combination of a high gain KB mirror system and a two dimensionally confined nanostructure fabricated by e-beam lithography can be used to produce x-ray beams with a cross section of down to $25 \times 47\text{nm}^2$ (FWHM), as evidenced from the far-field distribution of the exiting beam (see section 4.3). A flux density enhancement (gain) of $g \sim 4000$ was observed for the combined KB-waveguide system. Owing to the filtering properties of the waveguide, this beam is not accompanied by disturbing side peaks or spurious reflected and primary beams, as long as the waveguide length is matched to the incident x-ray energy. Compared to other methods to focus x-rays, this is one of the smallest beam sizes reported so far [JFO⁺05] getting close to the fundamental limit reported by [BKvdV03].

Making use of these small beamsizes, a sample can be scanned through the waveguided beam, measuring fluorescence radiation. Experimental evidence shows, that this waveguide enhanced scanning x-ray fluorescence can reach resolutions in the sub-100nm range.

Owing to its guiding properties, the waveguide also acts as a coherence filter for the incident photons. Utilizing these coherence properties and the divergence of the beam behind the guide, magnified in-line holograms can be recorded. Experimentally demonstrated with lithographically fabricated gold structures, a lateral resolution of $\approx 360\text{nm}$ was obtained in the reconstructed phase image of the sample. The theoretical limit in resolution is determined by the size of the waveguide and is in this case not reached, since the reconstructed phase is blurred by the twin image. To overcome this limitation reference beam holography was experimentally implemented, allowing to separate direct and twin image in the reconstruction. With this method the the theoretical limit for the resolution in the image seems to be reached.

Making use of the waveguide-based in-line holographic imaging, localization accuracies of $\approx 10\text{nm}$ are experimentally observed, which is below the theoretically obtainable lateral imaging resolution as defined in chapter 1 by about one order of magnitude. Based on this experimental observation, 'point-like' labels for hard x-ray holographic imaging are proposed. Depending on the size of these objects and on the total intensity in the waveguided beam, a lateral localization accuracy in the nanometer range should be obtainable.

Summary

Two dimensionally confining hard x-ray waveguides consist of a nanometer-sized guiding core embedded in an adequate cladding material. Within this thesis, we have experimentally demonstrated that these guides provide x-ray beams with cross sections of down to $25 \times 47 \text{ nm}^2$, when used in combination with a high gain focusing optic. Owing to their property to only support the propagation of a discrete number of modes, a highly coherent beam is exiting the waveguide. As evident from the performed measurements the far-field exhibits sufficient flux to perform imaging experiments. It is not disturbed by any side peaks or spurious reflected and primary beams, if the waveguide length is adapted to the incident x-ray energy.

An instrument was designed, to allow for waveguide based imaging. It consists of translational and rotational stages, providing the necessary degrees of freedom to align the waveguide in the focused x-ray beam. The sample positioning in the waveguided beam is realized with stages providing a precision of $\pm 15 \text{ nm}$. Thus, scanning experiments with a resolution comparable to the waveguide core size are not limited by the motors. For these scanning fluorescence experiments, an energy dispersive detector is included in the setup, as well as a high efficiency direct illumination CCD for holographic imaging. The whole instrument is designed to allow for scanning fluorescence and holographic imaging without changing the setup.

To demonstrate the capabilities of this waveguide based lens-less x-ray microscope, several proof-of-principle experiments were performed. Making use of the small beam dimensions behind the guide, scanning x-ray fluorescence was demonstrated. This method allows to image samples with a spatial resolution of $< 100 \text{ nm}$. Adapting the setup originally proposed for visible light [Gab48] to x-rays, in-line holographic imaging was demonstrated. A reconstruction of the phase shift at the sample position shows a spatial resolution with $\approx 360 \text{ nm}$, only blurred by the presence of a twin image in the reconstruction. To reach the theoretical resolution limit defined by the core dimension of the illuminating waveguide, the waveguide design

was altered to allow for reference beam illumination. Recording holograms with this illumination scheme allows to separate direct and twin image in the reconstruction. The observed spatial resolution in the reconstructed phase image of $\approx 100\text{nm}$ already approaches the theoretical limit mentioned above. Using the in-line holography setup, localization accuracies of down to 10nm are obtainable.

In conclusion it has been demonstrated in this thesis, that waveguide based lens-less imaging is possible utilizing the novel instrumentation designed in this thesis. The designed instrument provides all experimental prerequisites to allow for the alignment of waveguide and sample and to detect the x-rays with sufficient efficiency. With the setup, two dimensionally confined nano x-ray beams can be produced with sufficient flux to perform imaging experiments. Proof-of-principle experiments have been performed, showing that the instrument can be used in 'scanning mode' (waveguide based scanning fluorescence), or in 'full-field mode' (in-line and reference beam holography) without changing the setup.

Appendix A

MoWaSt implementation

In this appendix the source code for various pieces of software is given, which needed to be developed during the implementation of the MoWaSt setup.

A.1 CCD client-server application

To allow the synchronisation between the CCD acquisition software and the SPEC motor control software, a small client-server application via UDP protocol has been developed within the scope of this thesis. The source code of the server application running under Windows XP and making use of the COM libraries of the WinView acquisition software is given in this appendix. Also the SPEC macros, representing the client part on the instrument control computer are mentioned.

A.1.1 Server application

The server application is written in microsoft visual basic. It uses methods defined in the common libraries provided by the WinView software (version 2.5.16) package from Princeton Instruments / Roper Scientific. This design allows maximal transparency for the user. In fact only a small button in the WinView software has to be pressed to allow the connection and provide complete remote access to the acquisition software!! Main parts of the coding were done by Tim-Oliver Husser.

```
Public Class formMain
```

```
    Inherits System.Windows.Forms.Form
```

```
#Region " Windows Form Designer generated code "
```

```

Public Sub New()
    MyBase.New()

    'This call is required by the Windows Form Designer.
    InitializeComponent()

    'Add any initialization after the InitializeComponent() call

End Sub

'Form overrides dispose to clean up the component list.
Protected Overloads Overrides Sub Dispose(ByVal disposing As Boolean)
    If disposing Then
        If Not (components Is Nothing) Then
            components.Dispose()
        End If
    End If
    MyBase.Dispose(disposing)
End Sub

'Required by the Windows Form Designer
Private components As System.ComponentModel.IContainer

'NOTE: The following procedure is required by the Windows Form Designer
'It can be modified using the Windows Form Designer.
'Do not modify it using the code editor.
Friend WithEvents textLog As System.Windows.Forms.TextBox
Friend WithEvents textExecute As System.Windows.Forms.TextBox
Friend WithEvents butExecute As System.Windows.Forms.Button
<System.Diagnostics.DebuggerStepThrough()> Private Sub InitializeComponent()
    Me.textLog = New System.Windows.Forms.TextBox
    Me.textExecute = New System.Windows.Forms.TextBox
    Me.butExecute = New System.Windows.Forms.Button
    Me.SuspendLayout()
    ,

```

```
'textLog
,
Me.textLog.Location = New System.Drawing.Point(8, 8)
Me.textLog.Multiline = True
Me.textLog.Name = "textLog"
Me.textLog.ReadOnly = True
Me.textLog.ScrollBars = System.Windows.Forms.ScrollBars.Vertical
Me.textLog.Size = New System.Drawing.Size(456, 216)
Me.textLog.TabIndex = 0
Me.textLog.Text = ""
,
'textExecute
,
Me.textExecute.Location = New System.Drawing.Point(8, 232)
Me.textExecute.Name = "textExecute"
Me.textExecute.Size = New System.Drawing.Size(336, 20)
Me.textExecute.TabIndex = 0
Me.textExecute.Text = ""
,
'butExecute
,
Me.butExecute.Location = New System.Drawing.Point(352, 232)
Me.butExecute.Name = "butExecute"
Me.butExecute.Size = New System.Drawing.Size(112, 20)
Me.butExecute.TabIndex = 1
Me.butExecute.Text = "Execute"
,
'formMain
,
Me.AutoScaleBaseSize = New System.Drawing.Size(5, 13)
Me.ClientSize = New System.Drawing.Size(472, 261)
Me.Controls.Add(Me.butExecute)
Me.Controls.Add(Me.textExecute)
Me.Controls.Add(Me.textLog)
Me.MaximizeBox = False
Me.Name = "formMain"
```

```

        Me.Text = "Spec to WinView"
        Me.ResumeLayout(False)

    End Sub

```

```

#End Region

```

```

Private m_Server As CServer
Private m_ServerThread As Threading.Thread
Private m_VM As CVirtualMachine
Private m_CmdHistory As New Collections.ArrayList
Private m_CmdHistoryEnum As Int32

```

```

Private Sub textExecute_KeyPress(ByVal sender As Object, ByVal e As KeyPressEventArgs)
    If e.KeyChar = Microsoft.VisualBasic.ChrW(13) Then
        butExecute_Click(0, New EventArgs)
    End If
End Sub

```

```

Private Sub textExecute_KeyDown(ByVal sender As Object, ByVal e As KeyEventArgs)

    If e.KeyCode = Control.ModifierKeys.Up Then
        If m_CmdHistoryEnum > 0 Then
            m_CmdHistoryEnum = m_CmdHistoryEnum - 1
        End If
        textExecute.Text = m_CmdHistory(m_CmdHistoryEnum)
    ElseIf e.KeyCode = Control.ModifierKeys.Down Then
        If m_CmdHistoryEnum < m_CmdHistory.Count Then
            m_CmdHistoryEnum = m_CmdHistoryEnum + 1
        End If
        If m_CmdHistoryEnum = m_CmdHistory.Count Then
            textExecute.Text = ""
        Else
            textExecute.Text = m_CmdHistory(m_CmdHistoryEnum)
        End If
    End If

```

```
End If

End Sub

Private Sub butExecute_Click(ByVal sender As System.Object, ByVal e As System.EventArgs)
    Dim exec As String = textExecute.Text()
    textExecute.Clear()
    Execute(exec)
    m_CmdHistory.Add(exec)
    m_CmdHistoryEnum = m_CmdHistory.Count
    textExecute.Focus()
End Sub

Public Delegate Sub _Execute(ByVal cmd As String)

Public Sub Execute(ByVal cmd As String)
    m_VM.Execute(cmd)
End Sub

Public Sub ExecuteSync(ByVal cmd As String)
    If Me.InvokeRequired Then
        Dim args(0) As Object
        args(0) = cmd
        Me.Invoke(New _Execute(AddressOf Execute), args)
    Else
        Execute(cmd)
    End If
End Sub

Public Sub Log(ByVal log As String)
    textLog.AppendText(log)
    textLog.AppendText(Microsoft.VisualBasic.Constants.vbNewLine)
End Sub

Private Sub formMain_Load(ByVal sender As System.Object, ByVal e As System.EventArgs)
    Me.SetDesktopLocation(0, 0)
End Sub
```

```
Log("Spec To WinView 0.1")
Log(" by Tim-Oliver Husser (mail@husser.de), 2005")
Log("")

m_VM = New CVirtualMachine(Me)

m_Server = New CServer(Me)
m_ServerThread = New Threading.Thread(AddressOf m_Server.Start)
m_ServerThread.Start()
End Sub

Private Sub formMain_Closing(ByVal sender As System.Object, ByVal e As System.Co
    m_Server.Stop()
End Sub

Public Function getVM()
    Return m_VM
End Function

Public Function getServer()
    Return m_Server
End Function
End Class
```

A.1.2 Client SPEC macro

The client side uses the network and macro capabilities of the SPEC instrument control software. The by the server application opened socket on the remote windows computer is accessed via UDP protocol. This communication is hooked into the standard SPEC macro execution using chained macro definition. This is again, as for the server side, the construction with maximal transparency for the user.

```
#####
# macroset to trigger the princeton instruments ST133 controller #
```

```
# with the help of a udp server connected to winview on a separate
computer          # # chol 15.11.2005 #
```

```
#####
```

```
#                                     # # needs menu.mac
(adapted from esrf)                   # # needs
fastshutter.mac                        #
```

```
#####
```

```
# # ===== user commands
===== # ccdacq time accumulation frames
# exposure with specified time number of accumulations and numer
of frames # ccdsave                # saves last exposure and
asks for filename # ccdmenu        # menustyle
definition of all important parameters # ccdon                #
exposure acquisition during scans swichted on # ccdoff
#   "           "           "           "           "   off # #
```

```
===== internal commands
===== # # _ccdinit                #
initialisation of variables and parameters # _ccdscanset
# set exposure time during scan # _ccdset                # set
parameters # _ccd_start                # start exposure with
predefined parameters # _ccd_wait                # wait until
exposure finishes # _ccd_savescan                # define
filename and save exposure during scans # _ccd_menu
# core of ccdmenu # _ccd_cleanup                # take care of
scan abortions #
```

```
global CCD_IP CCD_AUTO CCD_FOLDER CCD_TIME CCD_FRA CCD_ACC
CCD_FILECOUNT global CCD_CUT CCD_SCANDATAFILE CCD_DATAFILE
CCD_SCANON global CCD_INTROI CCD_ROI_LEFT CCD_ROI_TOP
CCD_ROI_WIDTH CCD_ROI_HEIGHT CCD_ROIMNE
```

```
# #===== internal commands
===== #
```

```
# set all values to default and # estabilsh connection (although
```

```
it's not really necessary with udp ....) def _ccdinit '
    CCD_IP="192.168.0.101:24637"
    CCD_SCANON=0
    CCD_TIME=0.1
    CCD_ACC=1
    CCD_FRA=1
    CCD_INTNUM=7
    CCD_ROI_LEFT = 0
    CCD_ROI_TOP = 0
    CCD_ROI_WIDTH = 100
    CCD_ROI_HEIGHT = 100
    CCD_ROIMNE = "ccdroi"
    CCD_FOLDER="e:\\daten\\id22_1105\\"
    sock_par(CCD_IP,"connect_udp")
    CCD_FILECOUNT=0
    CCD_ACQFILENAME="ccddummy"
,

# pipe scanparameters to ccd def _ccdscanset '
    CCD_TIME=COUNT_TIME
    _ccdset
,

# set ccd parameters def _ccdset '
    sock_par(CCD_IP,"flush")
        sock_put(CCD_IP,sprintf("set exp_time %s",CCD_TIME))
    sock_put(CCD_IP,sprintf("set num_acc %s",CCD_ACC))
    sock_put(CCD_IP,sprintf("set num_frames %s",CCD_FRA))
    sock_put(CCD_IP,"olli")
    _ccd_wait
,

# start aquisition with predefined values def _ccd_start'
    sock_par(CCD_IP,"flush")
    sock_put(CCD_IP,"start")
,
```



```

# wait 'til exposure finishes def _ccd_wait '

    for(;sock_get(CCD_IP) != "done");

,

# save routine during scanning def _ccd_savescan '

    tempsave2=split(DATAFILE,CCD_CUT,"/") # cut out filename
    CCD_SCANDATAFILE=sprintf("%s%s_%s_%s",CCD_FOLDER,CCD_CUT[tempsave2-1],SCAN_N,NPTS
    sock_put(CCD_IP,sprintf("save %s",CCD_SCANDATAFILE))

,

def _ccd_precount '
    _ccdscanset
    _ccd_start
,

def _ccd_getcounts '
    _ccd_wait
    _ccdsave
    _ccd_wait
    _ccdintroi
,

def _ccdsave '
    CCD_DATAFILE=sprintf("%s%s_%s.spe",CCD_FOLDER,CCD_ACQFILENAME,CCD_FILECOUNT)
    sock_put(CCD_IP,sprintf("save %s",CCD_DATAFILE))
    p
    printf("Acquisition saved as: %s\n",CCD_DATAFILE)
    CCD_FILECOUNT++
,

def _ccd_cleanup ' ser_put(FS_ADDR,"A\n") _ccd_wait

```

```
ser_put(FS_ADDR,"A\n") p "Fastshutter was closed immediately but"
p "CHECK YOUR CCD for overexposure and/or communication problems
!!!!" '

# # ===== hook to standard macros
===== #

# # hook on # def ccdon '

cdef("user_precount","", "ccd_precount", "delete")
cdef("user_precount" ,"
    _ccd_precount
    ", "ccd_precount", 0x10)

cdef("user_getcounts","", "ccd_getcounts", "delete")
cdef("user_getcounts" ,"
    _ccd_getcounts
    ", "ccd_getcounts", 0x10)

cdef("measure0","", "ccd_measure0", "delete")
cdef("measure0" ,"
    CCD_SCANON=1
    ", "ccd_measure0")

cdef("measure2","", "ccd_measure2", "delete") cdef("measure2", "
    CCD_SCANON=0
    ", "ccd_measure2")

cdef("_cleanup2","", "ccd_cleanup", "delete") cdef("_cleanup2", "
_ccd_cleanup ", "ccd_cleanup")

# turn off fs while ccd takes control
#cdef("user_getcounts","", "fastshutter_getcounts", "delete")
#cdef("user_precount","", "fastshutter_precount", "delete")
#cdef("_cleanup2","", "fastshutter_cleanup", "delete")
```

```
p "ccd acquires during scanning...."
p "fastshutter now controlled by ccd !!"
,

# # hook off #

def ccdoff '
  cdef("user_precount","", "ccd_precount","delete")
  cdef("user_getcounts","", "ccd_getcounts","delete")
  cdef("measure0","", "ccd_measure0","delete")
  cdef("measure2","", "ccd_measure2","delete")
  cdef("_cleanup2","", "ccd_cleanup","delete")
# give back fs control to spec # if (FS_AUTO) { #
ser_put(FS_ADDR,"A\n") #close fs and

# cdef("user_precount","", "fastshutter_precount","delete") #
cdef("user_precount" ," #      _fastshutter_trigger #
", "fastshutter_precount",0x10)

# cdef("user_getcounts","", "fastshutter_getcounts","delete") #
cdef("user_getcounts" ," #      _fastshutter_trigger #
", "fastshutter_getcounts",0x10) # }

p "ccd acquisition turned off during scanning"
,

# #===== user commands
===== #

def ccdconnect '
  sock_par(CCD_IP,"connect_udp")
,

def ccdacq'
  if ($#!=3) {
    p "usage: ccdacq time accumulations frames"
```

```
    }
    if ($#==3) {
        CCD_TIME = $1
        CCD_ACC = $2
        CCD_FRA = $3
        _ccdset
        _ccd_start
        _ccd_wait
        printf("Exposure done:\n")
        printf(" %s second(s)\n", CCD_TIME)
        printf(" %s accumulation(s)\n", CCD_ACC)
        printf(" %s frame(s)\n", CCD_FRA)
        #tempsave3=0
        #if (yesno(sprintf("Save acquisition"), tempsave3)) {
            _ccdsave
        #} else {
            #p "Frame(s) NOT saved!"
            #p "Use ccdsave to save last exposure!!!"
        #}
    }
,

def ccdset '
    if ($#!=3) {
        p "usage: ccdset time accumulations frames"
        printf("active settings are: %s %s %s\n", CCD_TIME, CCD_ACC, CCD_FRA)
    } else {
        CCD_TIME=$1
        CCD_ACC=$2
        CCD_FRA=$3
        _ccdset
    }
,
```

```

def ccdsetroi '
    if ($#!=4) {
        p "usage: ccdsetroi left top width height"
        printf("active settings are: %s %s %s %s\n",CCD_ROI_LEFT,CCD_ROI_TOP,CCD_ROI_WIDT
    } else {
        CCD_ROI_LEFT = $1
        CCD_ROI_TOP = $2
        CCD_ROI_WIDTH = $3
        CCD_ROI_HEIGHT = $4
        if (CCD_ROI_LEFT<0 || CCD_ROI_TOP< 0 || CCD_ROI_WIDTH > 1339 || CCD_ROI_HEIGHT> 1
            p "roi settings do not match framesize! Try again ..."
        } else {
            _ccdintroi
            printf("Counts in active roi: %s\n",CCD_INTROI)
            printf("active settings are: %s (left) %s (top) %s (width) %s (height)\n",CCD_ROI
        }
    }
,

#define ccdintroi ' #    if ($#!=4) { #    p "usage: ccdintroi left top
width height" #    } else { #    _ccdintroi
#    printf("Counts in active roi: %s\n",CCD_INTROI)
#    printf("active settings are: %s (left) %s (top) %s (width) %s (height)\n",CCD_ROI
#    }

#'

def _ccdintroi '
    CCD_INTROI=0
    sock_par(CCD_IP,"flush")
    sock_put(CCD_IP,sprintf("integrateroi %s %s %s %s",CCD_ROI_LEFT,CCD_ROI_TOP,CCD_R
    ret = ""
    for(;ret == "");
        ret = sock_get(CCD_IP)
    ctr = cnt_num(CCD_ROIMNE)
    CCD_INTROI = ret

```

```
    S[ctr] = sprintf("%s",CCD_INTROI)
,

def ccdinit '
    _ccdinit
    p "All CCD setting are now reset to default values ! "
,

# ===== setup menu
===== #

def ccdmenu ' temp=CCD_ACQFILENAME menu("\n M o W a S t - C C D
S E T U P M E N U","_ccd_menu")
if(CCD_ACQFILENAME!=temp){CCD_FILECOUNT=0} _ccdset if (CCD_SCANON)
{ccdon} else {ccdoff} '

def _ccd_menu '{

    print
    menuoptval(-35,"\n","IP and Port of CCD computer: ",CCD_IP,"IP")
    menuvargetv("CCD_IP")

    print
    menuoptval(-35,"\n","Folder on CCD computer were frames are saved: ",CCD_FOLDER,"s")
    menuvargetv("CCD_FOLDER")
    # menuaction("if (CCD_FOLDER) {_ccd_folder_info}")
    print
    menuoptval(-35,"\n","CCD filename for ccdacq ",CCD_ACQFILENAME,"fi")
    menuvargetv("CCD_ACQFILENAME")
    menuaction("_save_scan_info2")
    print
    menuoptval(-35,"\n","Time set to: (sec)",CCD_TIME,"Ti")
    menuvargetv("CCD_TIME")
    menuoptval(-35,"\n","Number of accumulations set to: ",CCD_ACC,"ac")
```

```

menuvargetv("CCD_ACC")
menuoptval(-35,"\n","Number of frames set to: ",CCD_FRA,"fr")
menuvargetv("CCD_FRA")
print
print
menuoptval(-35,"\n","CCD acquisition during scans",CCD_SCANON?"ON":"OFF","sc")
menuvartogg("CCD_SCANON")
menuaction("_save_scan_info1")
print

# for (i=0;i<MCA_DEVNUM;i++) {
#   menuprint(0,MCA_DEVSTATUS[i],"DEVICE",sprintf("%s %s",MCA_DEVNAME[i],i));print
# }
# print
## if (MCA_DEVNUM>1 && MCA_DEVSTATUS[0]=="connected") {
# menuoptval(-35," ",sprintf("mca0 %s %s is ",MCA_DEVNAME[0],0),MCA_ACTIVE[0]?"activ
# menuaction("MCA_TOGGLE=0; mcactive 0; MCA_TOGGLE=1") # print #
} ## if (MCA_DEVNUM>1 && MCA_DEVSTATUS[1]=="connected") {
# menuoptval(-35," ",sprintf("mca1 %s %s is ",MCA_DEVNAME[1],1),MCA_ACTIVE[1]?"activ
# menuaction("MCA_TOGGLE=0; mcactive 1; MCA_TOGGLE=1") # print #
} ## if (MCA_DEVNUM>2 && MCA_DEVSTATUS[2]=="connected") {
# menuoptval(-35," ",sprintf("mca2 %s %s is ",MCA_DEVNAME[2],2),MCA_ACTIVE[2]?"activ
# menuaction("MCA_TOGGLE=0; mcactive 2; MCA_TOGGLE=1") # print #
} ## if (MCA_DEVNUM>3 && MCA_DEVSTATUS[3]=="connected") {
# menuoptval(-35," ",sprintf("mca3 %s %s is ",MCA_DEVNAME[3],3),MCA_ACTIVE[3]?"activ
# menuaction("MCA_TOGGLE=0; mcactive 3; MCA_TOGGLE=1") # print #
} ## print
# if (MCA_DEVNUM>0 && MCA_DEVSTATUS[0]=="connected") {
# menuoptval(-35," ", "Region-of-interest 0 (roi0) start channel: ",MCA_ROIBEG[0],"r
# menuvargetv("MCA_ROIBEG[0]","start channel")
# menuvargetv("MCA_ROIEND[0]","end channel")
# menuprint(-35,"\n","end channel:",MCA_ROIEND[0])
# menuoptval(-35,"\n","end channel: ",MCA_ROIEND[0],"")
# menuaction("if (MCA_ROIEND[0]<=MCA_ROIBEG[0]) {_mca_setupchk2;MCA_ROIEND[0]=MCA_RO
# menuaction("if (MCA_ROIEND[0]>4095) {_mca_setupchk3}")
# }

```

```
#else if (MCA_DEVNUM>0 && MCA_DEVSTATUS[0]=="unresponsive") {
#menuprint(-35,MCA_DEVSTATUS[0],"RoI is NOT set because",sprintf("%s %s",MCA_DEVNUM,MCA_DEVSTATUS[0]))
#}

# if (MCA_DEVNUM>1 && MCA_DEVSTATUS[1]=="connected") {
# menuoptval(-35,"  ", "RoI 1 start channel: ",MCA_ROIBEG[1],"r1s")
# menuvargetv("MCA_ROIBEG[1]")
# menuoptval(-35,"\n", "RoI 1 end channel: ",MCA_ROIEND[1],"r1e")
# menuvargetv("MCA_ROIEND[1]")
# menuaction("if (MCA_ROIEND[1]<=MCA_ROIBEG[1]) {_mca_setupchk2;MCA_ROIEND[1]=MCA_ROIBEG[1]}")
# menuaction("if (MCA_ROIEND[1]>4095) {_mca_setupchk3}")
# }
# else if (MCA_DEVNUM>1 && MCA_DEVSTATUS[1]=="unresponsive") {
#menuprint(-35,MCA_DEVSTATUS[1],"RoI is NOT set because",sprintf("%s %s",MCA_DEVNUM,MCA_DEVSTATUS[1]))
#}

# if (MCA_DEVNUM>2 && MCA_DEVSTATUS[2]=="connected") {
# menuoptval(-35,"  ", "RoI 2 start channel: ",MCA_ROIBEG[2],"r2s")
# menuvargetv("MCA_ROIBEG[2]")
# menuoptval(-35,"\n", "RoI 2 end channel: ",MCA_ROIEND[2],"r2e")
# menuvargetv("MCA_ROIEND[2]")
# menuaction("if (MCA_ROIEND[2]<=MCA_ROIBEG[2]) {_mca_setupchk2;MCA_ROIEND[2]=MCA_ROIBEG[2]}")
# menuaction("if (MCA_ROIEND[2]>4095) {_mca_setupchk3}")
# }
# else if (MCA_DEVNUM>2 && MCA_DEVSTATUS[2]=="unresponsive") {
#menuprint(-35,MCA_DEVSTATUS[2],"RoI is NOT set because",sprintf("%s %s",MCA_DEVNUM,MCA_DEVSTATUS[2]))
#}

# if (MCA_DEVNUM>3 && MCA_DEVSTATUS[3]=="connected") {
# menuoptval(-35,"  ", "RoI 3 start channel: ",MCA_ROIBEG[3],"r3s")
# menuvargetv("MCA_ROIBEG[3]")
# menuoptval(-35,"\n", "RoI 3 end channel: ",MCA_ROIEND[3],"r3e")
# menuvargetv("MCA_ROIEND[3]")
# menuaction("if (MCA_ROIEND[3]<=MCA_ROIBEG[3]) {_mca_setupchk2;MCA_ROIEND[3]=MCA_ROIBEG[3]}")
# menuaction("if (MCA_ROIEND[3]>4095) {_mca_setupchk3}")
# }
```



```

# else if (MCA_DEVNUM>3 && MCA_DEVSTATUS[3]=="unresponsive") {
#menuprint(-35,MCA_DEVSTATUS[3],"RoI is NOT set because",sprintf("%s %s",MCA_DEVNAM
#}

}',

#def _ccd_folder_info' # menuwarning("Be sure to use \\ \\
instead of \\ while typing folder !!!") #' #def _mca_setupchk2' #
menuerror("The last channel of RoI can never be lower than the
first channel") #' #def _mca_setupchk3' # menuerror("The last
channel of RoI can never bigger than 4095. Check your settings
..") #' def _save_scan_info1'
    menuwarning(sprintf("Filename for ccd during scan: %sSPECDATAFILE_SCANNUMBER_POINT
,

def _save_scan_info2'
    menuwarning(sprintf("Filename for ccd after ct and ccdacq: %s%s_increment.spe",CCD
,

#def _cal_energy20_info' # #menuwarning("Range set to 20keV.
Using: Energy=-540+5.08*Channel")
# menuwarning(sprintf("Range set to 20keV. Using: Energy=%s+%s*Channel",MCA_A20,MCA
#' #def _cal_energy40_info' # #menuwarning("Range set to 40keV.
Using: Energy=-975+10.1*Channel")
# menuwarning(sprintf("Range set to 40keV. Using: Energy=%s+%s*Channel",MCA_A40,MCA
#' #def _cal_energy_info' # menuwarning("Energy calibration only
possible for 20keV and 40keV range!! Please specify!") #' #def
_cal_range_info' # menuwarning("Wrong range specified (either
20keV or 40keV). Energy Calculation switched off.") #'

```

A.2 Roentec implementation

Since the SPEC software only supports low level access to the basic features of the roentec controller, it was necessary to write a macroset, allowing display and saving of this MCA data and some handy features for the user. This macroset also can

show how one can make use of the command and macro execution hierarchy of the SPEC software.

```

# # macro for initialisation for one roentec mca devices # utility
macros for running the Roentec MCA are also defined here # last
change: chol: 23.11.05 # # needs cplot.mac and menu.mac ( both
from ESRF ) # # # # ===== command definition
===== # # == user commands == # mcasetroi
[roinum] firstchan lastchan # set roi roinumber from channel
fistchannel to channel lastchannel # mcareadroi #
display roi settings # mcastatus # display all
relevant settings # mcaon # turn acquisition on
during scans # mcaoff # turn acquisition off
during scans # mcaactive devnumber # set mca device
devnumber to active # mcaacq time {devnumber} # acquire
spectrum for time time on mca device devnumber # mcaplot
firstchannel lastchannel # plot last acquired spectrum from
channel fistchannel to lastchannel # mcasave #
save last acquired spectrum # mcasavesetup # asks
for filename and acquisitionnumber for spectra saved after mcaacq
# mcasetup # menu for mca configuration # # ==
internal macros === # _mca_init # initialisation
of all needed variables # _mca_device # searches
for configured devices and sets status variables # measure0
# used to toggle MCA_TOGGLE (predefined in standard.mac) #
measure2 # used to toggle MCA_TOGGLE (predefined in
standard.mac) # user_getcounts # does acquisition and
counting during scans (predefined in standard.mac) # cleanup2
# set variables after aborting scans with ^C (predefined in
standard.mac) # _mca_save # save routine used by
mcasave and user_getcounts # _mca_menu # menu layout
for mcasetup #

# ===== global variable definition
=====

```

```

global MCA_DATA MCA_DUMMYDATA MCA_ACTIVE global MCA_DEVNAME
MCA_TIME MCA_ROIBEG MCA_ROIEND MCA_ROINUMBER MCA_TOGGLE global
MCA_DEVSTATUS MCA_ON MCA_SCANON MCA_STRINGON global MCA_SAVESCAN
MCA_SCANDATAFILE MCA_DATAFILE MCA_AQCOUNT MCA_AQDATAFILE global
MCA_LINES MCA_DOTS MCA_EBARS MCA_LOGPLOT global MCA_SLINES
MCA_SDOTS MCA_SEBARS MCA_SLOGPLOT MCA_PLOTSTRING global MCA_ENERGY
MCA_RANGE MCA_EDATA MCA_A MCA_B MCA_A20 MCA_B20 MCA_A40 MCA_B40
global MCA_AQFIRSTCHAN MCA_AQLASTCHAN MCA_ENERGYFIRST
MCA_ENERGYLAST

```

```

#=====
# #   internal command definition #
#=====

```

```

def _mca_device '{
    MCA_DEVNUM=0
    local _line _field
    fon "/tmp/mca_status_dump"
    offt
    mca_sel("?")
    fclose "/tmp/mca_status_dump"
    ont
        getline("/tmp/mca_status_dump","open")
    while ((_line=getline("/tmp/mca_status_dump"))!=-1) {
        split(_line,_field)
        if (index(_line,"0")) {
            if (index(_line,"unresponsive")) {
                MCA_DEVSTATUS="unresponsive"
            } else {
                MCA_DEVSTATUS="connected"
            }
        }
        if (_field[0]=="*") {
            MCA_ACTIVE=1
        }
    }
}

```

```
        MCA_DEVNAME=sprintf("%s %s %s %s",_field[2],_field[3],_field[4],_field[5])
    } else {
        MCA_ACTIVE=0
        MCA_DEVNAME=sprintf("%s %s %s %s",_field[1],_field[2],_field[3],_field[4])
    }
}
}
}
getline("/tmp/mca_status_dump","close")
u(rm /tmp/mca_status_dump)
}' # # send initial commands to all configured roentec mca devices
# def mcainit '
    _mca_init
,

def _mca_init '
    MCA_ENERGY=0
    MCA_RANGE=20
    MCA_TOGGLE=0
    MCA_SAVESCAN=0
    MCA_DATAFILE=sprintf("%s/acqdummy",CWD)
    MCA_SCANDATAFILE=sprintf("%s/scandummy",CWD)
    MCA_PLOTSTRING=sprintf("-ylog +lines +dots -ebars")
    MCA_LOGPLOT=0
    MCA_LINES=1
    MCA_EBARS=0
    MCA_dots=1
    MCA_AQFIRSTCHAN=0
    MCA_AQLASTCHAN=4095
    MCA_ENERGYFIRST=0
    MCA_ENERGYLAST=20000
    MCA_A20=-540
    MCA_B20=5.08
    MCA_A40=-975
    MCA_B40=10.1
    MCA_A=MCA_A20
    MCA_B=MCA_B20
```

```

_mca_device
mcaoff
ulong array MCA_DATA[4096] [2]
ulong array MCA_DUMMYDATA[4096]
long array MCA_EDATA[4096] [2]
    mca_sel(0)
    MCA_AQCOUNT=0
mca_par("halt")
    mca_par("clear")
    mca_par("auto_run",1)
    mca_par("auto_clear",1)
MCA_ROINUMBER=1
for(j=0;j<3;j++) {
    MCA_ROIBEG[j] [i]=0
    MCA_ROIEND[j] [i]=4095
        counter_par(cnt_num(sprintf("roi%s%s",j,i)),"disable",4711)
    }
for(j=0;j<MCA_ROINUMBER;j++) {
    counter_par(cnt_num(sprintf("roi%s%s",j,i)),"disable",0)
}
MCA_TOGGLE=1
# counter_par for roi setup
,

#####
# # user commands #
#####

# # explicit acquisition # def mcaacq'
if ($#==0) {
    MCA_TIME=1
    p "usage: mcaacq time"
}
if ($#==1) {
    MCA_TIME=$1
}

```

```
mca_par("auto_run",1)
mca_par("soft_preset",1)
tcount(MCA_TIME)
wait(4)
mca_get(MCA_DUMMYDATA)
MCA_DATA[0:4095][1]=array_op("transpose",MCA_DUMMYDATA)
array_op("fill",MCA_DATA[0:4095][0],1)
if (MCA_ENERGY) {
  if (MCA_RANGE==20) {
    MCA_EDATA[0:4095][1]=MCA_DATA[0:4095][1]
    MCA_EDATA[0:4095][0]=(MCA_A20+MCA_B20*MCA_DATA[0:4095][0])
  }
  if (MCA_RANGE==40) {
    MCA_EDATA[0:4095][1]=MCA_DATA[0:4095][1]
    MCA_EDATA[0:4095][0]=(MCA_A40+MCA_B40*MCA_DATA[0:4095][0])
  }
}
  if (MCA_ENERGY==0) {mcaplot MCA_AQFIRSTCHAN MCA_AQLASTCHAN}
if (MCA_ENERGY==1) {mcaplot MCA_ENERGYFIRST MCA_ENERGYLAST}
,

# # plot and replot the data #

def mcaplot'

if (MCA_ENERGY==0) {
  if ($#==2){
    MCA_AQFIRSTCHAN=$1
    MCA_AQLASTCHAN=$2
  }
  aqfirstchan=MCA_AQFIRSTCHAN
  aqlastchan=MCA_AQLASTCHAN

  plot_cntl(sprintf("filter%s",2))
  #plot_cntl("filter3")
  plot_cntl(sprintf("colors=%s",splot_col))
```

```
plot_cntl(MCA_PLOTSTRING)
plot_cntl("open")
plot_cntl("erase")
plot_cntl("mca")
plot_cntl("perpetual")
plot_cntl(sprintf("title= Roentec counts per channel number"))
plot_range(aqfirstchan, aqlastchan, 0, "auto")
#data_plot(42,aqfirstchan,aqlastchan-aqfistchan,"all")
#data_plot(42,0,4095,"all")
array_plot(MCA_DATA[aqfirstchan:aqlastchan] [])

        res1 = sprintf("Peak at %.5g is %.5g.  COM at %.5g.  ",MCA_DATA[array_op

        res2 = sprintf("FWHM is %.5g at %.5g.  Total counts are %g",

        res3 = sprintf("Total counts in RoI00 (channel %s - %s) are %g", MCA_ROIB

plot_move(-50,0,res1)
plot_move(-50,1,res2)
plot_move(-50,2,res3)

plot_move(0,1,sprintf("Roentec SPECTRUM"))
plot_move(0,2,"Counts")
plot_move(0,-1,sprintf("%.8s", "Channels"))

plot_cntl("filter1")

} if (MCA_ENERGY==1){

if (MCA_RANGE==20) {
    if ($#==2){
        MCA_ENERGYFIRST=$1
        MCA_ENERGYLAST=$2
    }
    energyfirst=MCA_ENERGYFIRST
    energylast=MCA_ENERGYLAST
```

```
aqfirstchan=((energyfirst-MCA_A20)/MCA_B20)
aqlastchan=((energylast-MCA_A20)/MCA_B20)
enroi beg=((MCA_ROIBEG [0] [0]*MCA_B20)+MCA_A20)
enroi end=((MCA_ROIEND [0] [0]*MCA_B20)+MCA_A20)
} if (MCA_RANGE==40) {
  if ($#==2){
    MCA_ENERGYFIRST=$1
    MCA_ENERGYLAST=$2
  }
  energyfirst=MCA_ENERGYFIRST
  energylast=MCA_ENERGYLAST
  aqfirstchan=((energyfirst-MCA_A40)/MCA_B40)
  aqlastchan=((energylast-MCA_A40)/MCA_B40)
  enroi beg=((MCA_ROIBEG [0] [0]*MCA_B40)+MCA_A40)
  enroi end=((MCA_ROIEND [0] [0]*MCA_B40)+MCA_A40)
}

plot_cntl(sprintf("filter%s",2))
#plot_cntl("filter3")
plot_cntl(sprintf("colors=%s",splot_col))
plot_cntl(MCA_PLOTSTRING)
plot_cntl("open")
plot_cntl("erase")
plot_cntl("mca")
plot_cntl("perpetual")
plot_cntl(sprintf("title= Roentec counts per Energy"))
plot_range(energyfirst, energylast, 0, "auto")
#data_plot(42,aqfirstchan,aqlastchan-aqfirstchan,"all")
#data_plot(42,0,4095,"all")
array_plot(MCA_EDATA[aqfirstchan:aqlastchan] [])

res1 = sprintf("Peak at %.5g is %.5g. COM at %.5g. ",MCA_EDATA[array_

res2 = sprintf("FWHM is %.5g at %.5g. Total counts are %g",

res3 = sprintf("Total counts in RoI00 (Energy %s - %s eV) are %g", enroi
```



```

plot_move(-50,0,res1)
plot_move(-50,1,res2)
plot_move(-50,2,res3)

plot_move(0,1,sprintf("Roentec SPECTRUM"))
plot_move(0,2,"Counts")
plot_move(0,-1,sprintf("%.8s", "E [eV]"))

plot_cntl("filter1")

}
  if ($#==0){
    print "usage: mcaplot firstchannelnumber lastchannelnumber"
  }
,

# # define plotting #

def mcasetplot'
  MCA_LOGPLOT=yesno("Plot spectrum logarithmically :",MCA_LOGPLOT)
  MCA_LINES=yesno("Connect spectrum points with lines :",MCA_LINES)
  MCA_DOTS=yesno("Plot spectrum with big dots :",MCA_DOTS)
  MCA_EBARS=yesno("Plot spectrum with errorbars :",MCA_EBARS)
  if (MCA_LOGPLOT) {MCA_SLOGPLOT="+ylog"} else {MCA_SLOGPLOT="-ylog"}
  if (MCA_LINES) {MCA_SLINES="+lines"} else {MCA_SLINES="-lines"}
  if (MCA_DOTS) {MCA_SDOTS="+dots"} else {MCA_SDOTS="-dots"}
  if (MCA_EBARS) {MCA_SEBARS="+ebars"} else {MCA_SEBARS="-ebars"}
  MCA_PLOTSTRING=sprintf("%s %s %s %s",MCA_SLOGPLOT,MCA_SLINES,MCA_SDOTS,MCA_SEBAR
#MCA_PLOTROI=yesno("Should a RoI be displayed in plot ",MCA_PLOTROI)
#if (MCA_PLOTROI) {
  #MCA_PLOTROIINUM=getval(sprintf
,

#=====
# # hook to standard macros #
#=====

```

```
def mcaon '

cdef("user_getcounts","", "mca_getcounts", "delete")
cdef("user_getcounts", "
    _mca_user_getcounts
", "mca_getcounts")

cdef("user_precount","", "mca_precount", "delete")
cdef("user_precount", "
    _mca_precount
", "mca_precount")

#cleanupstring=" Scan was aborted. Run mcasetup to make sure all
MCA settings are correct."
#cdef("_cleanup2","", "mca_cleanup2", "delete") #cdef("_cleanup2", "
#    _mca_cleanup #", "mca_cleanup2") MCA_ON=1 '

def mcaoff ' i=0 cdef("user_precount","", "mca_precount", "delete")
cdef("measure0","", "mca_measure0", "delete")
cdef("measure2","", "mca_measure2", "delete")
cdef("user_getcounts","", "mca_getcounts", "delete")
    for (j=0; j<MCA_ROINUMBER; j++){
        S[cnt_num(sprintf("roi%s%s", j, i))]=0
    }
    for(j=0; j<3; j++) {
        MCA_ROIBEG[j][i]=0
        MCA_ROIEND[j][i]=4095
        counter_par(cnt_num(sprintf("roi%s%s", j, i)), "disable", 4711)
    }
    for(j=0; j<MCA_ROINUMBER; j++) {
        counter_par(cnt_num(sprintf("roi%s%s", j, i)), "disable", 0)
    }
MCA_ON=0 MCA_SAVESCAN=0 '
```

```

def _mca_precount '
    MCA_TIME=COUNT_TIME
    mca_par("auto_run",1)
    mca_par("soft_preset",1)
    tcount(MCA_TIME)
    #p MCA_TIME
,

def _mca_user_getcounts'
    MCA_TOGGLE=0
    wait(4)
    mca_get(MCA_DUMMYDATA)
    MCA_DATA[0:4095][1]=array_op("transpose",MCA_DUMMYDATA)
    array_op("fill",MCA_DATA[0:4095][0],1)
    if (MCA_ENERGY) {
        if (MCA_RANGE==20) {
            MCA_EDATA[0:4095][1]=MCA_DATA[0:4095][1]
            MCA_EDATA[0:4095][0]=(MCA_A20+MCA_B20*MCA_DATA[0:4095][0])
        }
        if (MCA_RANGE==40) {
            MCA_EDATA[0:4095][1]=MCA_DATA[0:4095][1]
            MCA_EDATA[0:4095][0]=(MCA_A40+MCA_B40*MCA_DATA[0:4095][0])
        }
    }
    if (MCA_ENERGY==0) {mcaplot MCA_AQFIRSTCHAN MCA_AQLASTCHAN}
    if (MCA_ENERGY==1) {mcaplot MCA_ENERGYFIRST MCA_ENERGYLAST}
    i=0
    for (j=0;j<MCA_ROINUMBER;j++){
        S[cnt_num(sprintf("roi%s%s",j,i))]=array_op("sum",MCA_DATA[MCA_ROIBEG[j][i]:
    }
    if (MCA_SAVESCAN) mcasave
    MCA_TOGGLE=1
    #p MCA_TIME
,

```

```

# # ===== Region of interest
===== #

# setting up different roi's on each device def mcaroisetup' i=0
MCA_ROINUMBER=getval(sprintf("Number of RoIs on Roentec active"),MCA_ROINUMBER)
p MCA_ROINUMBER
for(j=0;j<MCA_ROINUMBER;j++) {
MCA_ROIBEG[j][i]=getval(sprintf("First channel on RoI%s of Roentec",j),MCA_ROIBEG[j][i])
MCA_ROIEND[j][i]=getval(sprintf("Last channel on RoI%s of roentec",j),MCA_ROIEND[j][i])
counter_par(cnt_num(sprintf("roi%s%s",j,i)),"disable",0)
}
,

# read roi settings # def mcareadroi'
for(j=0;j<MCA_ROINUMBER;j++){
if (MCA_DEVSTATUS=="connected" && counter_par(cnt_num(sprintf("roi%s%s",j,i)),"disable",0) > 0)
printf("RoI%s on Roentec is set from channel %s to %s\n",j,MCA_ROIBEG[j][i],MCA_ROIEND[j][i])
} else if (MCA_DEVSTATUS=="connected" && counter_par(cnt_num(sprintf("roi%s%s",j,i)),"disable",0) == 0)
printf("RoI%s on %s is NOT set. roi%s%s is disabled!\n",j,MCA_DEVNAME,j,i)
} else {
printf("RoI%s on %s is NOT set. ",j,MCA_DEVNAME)
printf("%s is unresponsive!\n",MCA_DEVNAME)
}
}
,

# # ===== save mca data
===== # def mcasave'
if (MCA_SAVESCAN==1) {
MCA_SCANDATAFILE=sprintf("%s_%s_%s.mca",DATAFILE,SCAN_N,NPTS)
_mca_save MCA_SCANDATAFILE
} else {
if (MCA_DATAFILE!=""){

```

```

MCA_AQDATAFILE=sprintf("%s_%s.mca",MCA_DATAFILE,MCA_AQCOUNT)
_mca_save MCA_AQDATAFILE
printf("Saved file is named: %s\n",MCA_AQDATAFILE)
MCA_AQCOUNT++
} else {
p " No roentec filename defined. Running mcasavesetup instead:"
mcasavesetup
p " Spectrum NOT saved. Try mcasave again!! "
}
}
,

# # implement if return von open ==-1 ??? #

def _mca_save '
dummy=$1
if (MCA_SAVESCAN) {
open(MCA_SCANDATAFILE)
on(MCA_SCANDATAFILE)
offt
printf("#\n")
printf("# Acquisition time: %s seconds\n",MCA_TIME)
printf("#\n")
for(i=0;i<100;i++){ #replace 28 with # of motors
if (motor_mne(i)!="?") {
printf("# %s %s \n",motor_mne(i),A[i])
#p i
} else {
break
}
}
printf("#\n")
array_dump(MCA_DATA)
ont
close(MCA_SCANDATAFILE)

```

```
} else {
    open(MCA_AQDATAFILE)
on(MCA_AQDATAFILE)
offt
printf("#\n")
printf("# Acquisition time: %s seconds\n",MCA_TIME)
printf("#\n")
for(i=0;i<100;i++){ #22 durch # of motors ersetzen
    if (motor_mne(i)!="?") {
        printf("# %s %s \n",motor_mne(i),A[i])
        p i
    } else {
        break
    }
}
printf("#\n")
#data_dump(42,0,4096,"all")
array_dump(MCA_DATA)
ont
close(MCA_AQDATAFILE)
}
,

# # define filename and scannumber for saving after mcaacq #

def mcasavesetup '
    MCA_DATAFILE=getval("Roentec filename ",MCA_DATAFILE)
    MCA_AQCOUNT=getval(sprintf("Next spectrum number for Roentec :"),MCA_AQCOUNT)
    p
    printf("Filename set to %s.\n",MCA_DATAFILE)
        printf("Next spectrum on Roentec is number %s.\n",i,MCA_AQCOUNT)
,

#=====
# # mca setup menu #
#=====
```

```

def mcamenu ' #if (MCA_DEVNUM==0) {_mca_init} menu("\n M o W a S
t - R O E N T E C S E T U P M E N U", "_mca_menu" ) '

def _mca_menu '{

menuprint(0,MCA_DEVSTATUS,"DEVICE",sprintf("%s %s",MCA_DEVNAME,0));print
  print
  print
  print
menuoptval(-35,"\n","Calculate Energy from Channel number",MCA_ENERGY?"ON":"OFF","C
menuvartogg("MCA_ENERGY")
menuaction("if (MCA_ENERGY) {_cal_energy_info}")
print
menuoptval(-35,"\n","Measuring range of the MCA is set to",MCA_RANGE,"ra")
menuvargetv("MCA_RANGE")
menuaction("if (MCA_ENERGY==1 && MCA_RANGE==20) {_cal_energy20_info; MCA_A=MCA_A20;

menuoptval(-35,"\n","Fitparatemer A Energy - Channel (Energy=A+B*channel)",MCA_A,"A
menuvargetv("MCA_A")
menuaction("if (MCA_RANGE==20) {MCA_A20=MCA_A};if (MCA_RANGE==40) {MCA_A40=MCA_A}")
menuoptval(-35,"\n","Fitparatemer B Energy - Channel (Energy=A+B*channel)",MCA_B,"B
menuvargetv("MCA_B")
menuaction("if (MCA_RANGE==20) {MCA_B20=MCA_B};if (MCA_RANGE==40) {MCA_B40=MCA_B}")

print
menuoptval(-35,"\n","Spectrum acquisition in scan",MCA_ON?"ON":"OFF","ac")
menuvartogg("MCA_ON")
menuaction("if (MCA_ON) {mcaon;MCA_SAVESCAN=1} else {mcaoff;MCA_SAVESCAN=0}")

print
menuoptval(-35,"\n","SAVE spectrum during scans",MCA_SAVESCAN?"YES":"NO","sc")
menuvartogg("MCA_SAVESCAN")

```

```
#if (MCA_ON==0 && MCA_SAVESCAN==1) {
# _mca_setupchk
#}
#menuaction("if (MCA_ON==0) {_mca_setupchk;MCA_SAVESCAN=0}")
#menuaction("if (MCA_SAVESCAN) {_save_scan_info}")

print
menuoptval(-35,"\n","Spectrum filename for mcaacq: ",MCA_DATAFILE,"fi")
menuvargetv("MCA_DATAFILE")

    menuoptval(-35,"\n",sprintf(" Next spectrum on Roentec is number "),MCA_AQCOUNT,"")
    menuvargetv("MCA_AQCOUNT")

print
}'

def _mca_setupchk'
    menuerror("Saving data while acquisition is off does not make sense")
' def _mca_setupchk2'
    menuerror("The last channel of RoI can never be lower than the first channel")
' def _mca_setupchk3'
    menuerror("The last channel of RoI can never bigger than 4095. Check your settings")
' def _save_scan_info'
    menuwarning("Filename for spectrum during scan: SPECDATAFILE_SCANNUMBER_POINTNUMBER")
' def _cal_energy20_info'
    #menuwarning("Range set to 20keV. Using: Energy=-540+5.08*Channel")
    menuwarning(sprintf("Range set to 20keV. Using: Energy=%s+%s*Channel",MCA_A20,MCA_A20))
' def _cal_energy40_info'
    #menuwarning("Range set to 40keV. Using: Energy=-975+10.1*Channel")
    menuwarning(sprintf("Range set to 40keV. Using: Energy=%s+%s*Channel",MCA_A40,MCA_A40))
' def _cal_energy_info'
    menuwarning("Energy calibration only possible for 20keV and 40keV range!! Please")
' def _cal_range_info'
    menuwarning("Wrong range specified (either 20keV or 40keV). Energy Calculation switch")
,
```

Appendix B

Implementation of the Hybrid-Input-Output algorithm

In this appendix the source code (IDL) for an application is given, which simulates a coherent diffraction experiment with an FFT of the sample, represented by a bitmap. This of course ignores real experimental conditions, where noise is present and the beam has a finite lateral coherence length, limiting the reconstructible sample size. Nevertheless the application can illustrate the convergence behavior of the algorithm (see figure ??). Note, that the orientation of the reconstructed object depends on the initial random phase in the iteration and can not be controlled.

The algorithm is implemented as described in [Fie78, MCKS99, MIJ⁺02, MIAH03].

```
pro OnOver, Event ; Get the image stored in the value of the
top-level-base.
    WIDGET_CONTROL, Event.top, GET_UVALUE=grayscaleimage, /NO_COPY

i=complex(0,1);

;; Find the slider widget, which is named iterate.
    witerate = WIDGET_INFO(Event.top, FIND_BY_UNAME='iterate');
    ; Make sure something was found.
    IF(witerate GT 0)THEN BEGIN
        ; Make the draw widget the current, active window.
        WIDGET_CONTROL, witerate, GET_VALUE=iterate
    endif
```

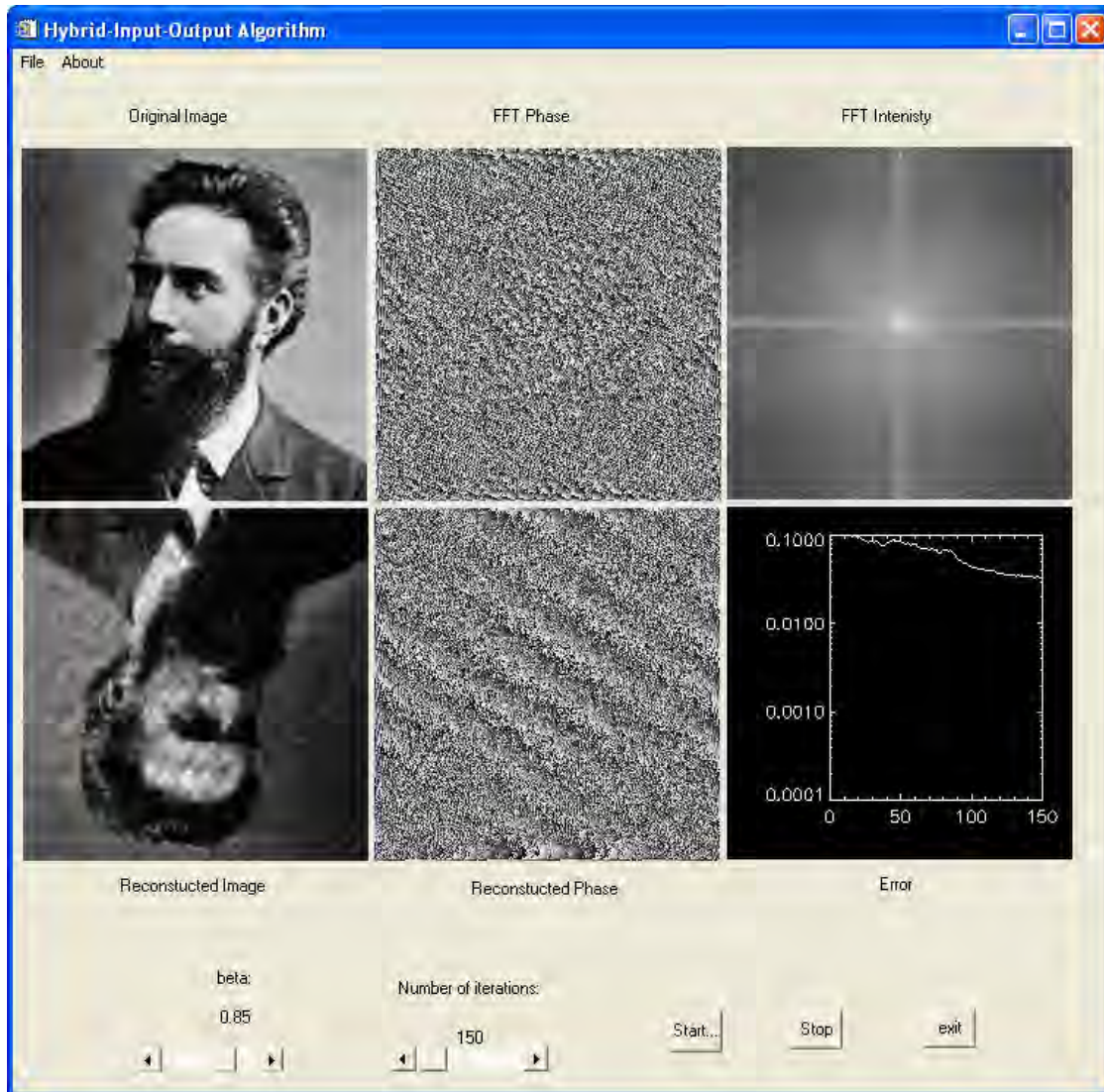


Figure B.1: Screenshot of the hybrid-input-output application. The original image is put on a 16 times larger support and fourier transformed. The squared modulus, which would correspond to the detected intensity in a coherent diffraction experiment, is then used as input for the hybrid-input-output algorithm.

```
;; Find the label widget, which is named lab_beta ; and get
userdefined beta value
witerate = WIDGET_INFO(Event.top, FIND_BY_UNAME='lab_beta');
; Make sure something was found.
IF(witerate GT 0)THEN BEGIN
    ; Make the draw widget the current, active window.
    WIDGET_CONTROL, witerate, GET_VALUE=beta
```

```

endif

; Initialize display. DEVICE, DECOMPOSED = 1

;get the widget ids

; Find the draw widget, which is named Image.
wDraw = WIDGET_INFO(Event.top, FIND_BY_UNAME='Image');
; Make sure something was found.
IF(wDraw GT 0)THEN BEGIN
    ; Make the draw widget the current, active window.
    WIDGET_CONTROL, wDraw, GET_VALUE=idImage
endif
; Find the draw widget, which is named Image.
wDraw = WIDGET_INFO(Event.top, FIND_BY_UNAME='ReconstImage');
; Make sure something was found.
IF(wDraw GT 0)THEN BEGIN
    ; Make the draw widget the current, active window.
    WIDGET_CONTROL, wDraw, GET_VALUE=idReconst
endif
; Find the draw widget, which is named Error.
wDraw = WIDGET_INFO(Event.top, FIND_BY_UNAME='Error');
; Make sure something was found.
IF(wDraw GT 0)THEN BEGIN
    ; Make the draw widget the current, active window.
    WIDGET_CONTROL, wDraw, GET_VALUE=idError
endif
; Find the draw widget, which is named Error.
wDraw = WIDGET_INFO(Event.top, FIND_BY_UNAME='FFTAmp1');
; Make sure something was found.
IF(wDraw GT 0)THEN BEGIN
    ; Make the draw widget the current, active window.
    WIDGET_CONTROL, wDraw, GET_VALUE=idFFTAmp1
endif
; Find the draw widget, which is named Error.
wDraw = WIDGET_INFO(Event.top, FIND_BY_UNAME='ReconstPhase');

```

```
    ; Make sure something was found.
    IF(wDraw GT 0)THEN BEGIN
        ; Make the draw widget the current, active window.
        WIDGET_CONTROL, wDraw, GET_VALUE=idRecPhase
    endif
    ; Find the draw widget, which is named Error.
    wDraw = WIDGET_INFO(Event.top, FIND_BY_UNAME='FFTPHase');
    ; Make sure something was found.
    IF(wDraw GT 0)THEN BEGIN
        ; Make the draw widget the current, active window.
        WIDGET_CONTROL, wDraw, GET_VALUE=idFFTPHase
    endif

; read out image size grayscale=SIZE(grayScaleImage)
xsize=grayscale[1] ysize=grayscale[2]

;define support size with sigma sigma=16 if (ysize GT xsize) OR
(ysize EQ xsize) then begin
    suppsize=fix(sqrt(sigma)*ysize)
endif else begin
    suppsize=fix(sqrt(sigma)*xsize)
endif
endelse

;build support IM_supp = MAKE_ARRAY(suppsize, suppsize, /complex,
VALUE = 0) WSET,idImage im = CONGRID(BYTSCL(ABS(IM_supp)^2),
!D.X_SIZE, !D.Y_SIZE) TVSCL, im ; set position of image xpos=5
ypos=7 ;put grayscale image on complex 0-support with phase 0
IM_supp[xpos,ypos]=grayscaleimage;amplitude image
;IM_supp[xpos,ypos]=grayscaleimage*exp(i*grayscaleimage);amplitude+phase
image ;IM_supp[xpos,ypos]=1*exp(i*grayscaleimage);phase image
;IM_supp[xpos,ypos]=0.01*grayscaleimage*exp(i*grayscaleimage);weak
amplitude+phase image

; Compute the two-dimensional FFT. fimage = FFT(IM_supp)
```

```

; assign amplitude an phase AMPfimage = ABS(fimage)^2 phasefimage
= ATAN(fimage, /PHASE)

shiftsize=fix((suppsize/2)-1)

AMPfimageShift=AMPfimage

dummy=AMPfimage[0:shiftsize,0:shiftsize]
AMPFimageShift[shiftsize+1,shiftsize+1]=dummy

dummy=AMPfimage[shiftsize+1:suppsize-1,shiftsize+1:suppsize-1]
AMPFimageShift[0,0]=dummy

dummy=AMPfimage[0:shiftsize,shiftsize+1:suppsize-1]
AMPFimageShift[shiftsize+1,0]=dummy

dummy=AMPfimage[shiftsize+1:suppsize-1,0:shiftsize]
AMPFimageShift[0,shiftsize+1]=dummy

WSET,idFFTAmp1 im = CONGRID(alog10(AMPfimageShift), !D.X_SIZE,
!D.Y_SIZE) TVSCL, im WSET,idFFTPhase im = CONGRID(phasefimage,
!D.X_SIZE, !D.Y_SIZE) TVSCL, im ; now initialising variables for
reconstruction ;beta=0.8 ;decreasing parameter ;iterate=200 ;
number of iterations ;defining variables for iteration error=
MAKE_ARRAY(2, iterate+1, /float, VALUE = 0);array to hold the
error during iteration real_it = MAKE_ARRAY(suppsize, suppsize,
/complex, VALUE = 0); image in real space during iteration
fourier_it = MAKE_ARRAY(suppsize, suppsize, /complex, VALUE = 0);
image in fourier space during iteration RITShift =
MAKE_ARRAY(suppsize, suppsize, /complex, VALUE = 0); usefor for
shifting images for display zero = MAKE_ARRAY(xsize, ysize,
/complex, VALUE = 0); useful for defining the support phaseinit=
MAKE_ARRAY(suppsize, suppsize, /float, VALUE = 1); initial phase
mask= MAKE_ARRAY(suppsize, suppsize, /float, VALUE = 1);

; some more initialisation fourier_AMP=sqrt(AMPFimage) ;the amp.

```

```
of diff.-pattern = root of intensity fourier_it =
fourier_AMP*exp(i*phaseinit); construct complex fourier image from
'diffraction pattern' real_it = FFT(fourier_it, /inverse) ; back
to real space for iteration

xmask=xpos+xsize-1 ymask=ypos+ysize-1

;now iterating for the reconstruction
FOR j = 0L, iterate DO BEGIN

    error[0,j]=j

    real_temp = real_it; save real image from last iteration

    fourier_it=FFT(real_it);

    wset, idRecPhase
    im = CONGRID(Atan(fourier_it, /phase), !D.X_SIZE, !D.Y_SIZE)
    TVscl, im

    ; reset fourier amplitude to initial one
    fourier_it=fourier_AMP*(fourier_it/ABS(fourier_it))

    ; back to real space
    real_it = FFT(fourier_it, /inverse); get g(k)'

    ; define support part of image and implementation of constraints

    IMreal_it=imaginary(real_it)
    temp=(abs(IMreal_it)-IMreal_it)/(2*IMreal_it+0.00000000001)
    mask[xpos:xmask,ypos:ymask]=abs(temp[xpos:xmask,ypos:ymask])

    ; let's look for the error
    Wset, idError
    error[1,j]=sqrt((total(total(abs(real_it*mask)^2),1))/(total(total(abs(real_it-
    PLOT, error[1,*],/ylog,yrange=[0.000001,0.1] ;,/xlog
```

```

;calculate new real image from support constraints
Rmask=abs(1-mask)
real_it=(mask*(real_temp-(beta*real_it)))+(Rmask*real_it)

;display new image
AMPL = BYTSCL(ABS(real_it)^2);amplitude
;AMPL = BYTSCL(Atan(real_it, /phase));phase
wset, idReconst
recim = CONGRID(AMPL[xpos:xmask,ypos:ymask], !D.X_SIZE, !D.Y_SIZE)
TVscl, recim

ENDFOR

end

pro OnExit, event WIDGET_CONTROL, Event.top, /DESTROY end ;

pro OnOpen, Event

    COMPILE_OPT hidden, strictarr

    catch,error_status
    if (error_status ne 0) then begin
        dummy = DIALOG_MESSAGE(!ERROR_STATE.msg, /ERROR, $
            TITLE='Import_Image Error')
        return
    endif

    void = DIALOG_READ_IMAGE(FILE=filename, QUERY=queryStr, IMAGE=image,RED=red,$
        GREEN=green, BLUE=blue, GET_PATH=gp)

    if (filename eq '') then return

```

```
tempStr = {    IMAGE: image, $
              R: red, $
              G: green, $
              B: blue, $
              QUERY: queryStr $
            }

;; Store the return variable into a var for the user
void = ROUTINE_NAMES('image', STORE=ROUTINE_NAMES(/LEVEL)-1, tempStr)

;store the image in the top level base widget user value
    WIDGET_CONTROL, Event.top, SET_UVALUE=image, /NO_COPY
; convert image to grayscale and display it red = REFORM(image[0,
*, *]) green = REFORM(image[1, *, *]) blue = REFORM(image[2, *,
*]) grayscaleImage = BYTE(0.299*FLOAT(red) + 0.587*FLOAT(green) +
0.114*FLOAT(blue))

; Find the draw widget, which is named Image.
wDraw = WIDGET_INFO(Event.top, FIND_BY_UNAME='Image');
; Make sure something was found.
IF(wDraw GT 0)THEN BEGIN
    ; Make the draw widget the current, active window.
    WIDGET_CONTROL, wDraw, GET_VALUE=idImage
endif
WSET,idImage im = CONGRID(grayscaleImage, !D.X_SIZE, !D.Y_SIZE)
TVSCL, im

WIDGET_CONTROL, Event.top, SET_UVALUE=grayscaleimage, /NO_COPY end
```

Appendix C

Simulation of the holograms of point scatterers

Here the source code (IDL) for the simulations shown in section 4.7 is given.

```
;model 2D colloidal suspension with colloid as point ; in wg beam
to see what happens in hologram ;chol 20.01.06

pro rand_holo common Parameters, Q, D, DC

;parameters for field calculation acctime = 1 ; accumulation time
for frame DY=1000 DX=1000 ; points in frame disx=10d-3
;framegröße in meter disy=10d-3 Energy=10.4D ; energy in keV
detdist = 1D ; detector distance in meter sampos = 1d-4 ; sample
position in meter from wg exit divergence = 2 ; width of WG-FF in
mrad width=detdist*divergence*1e-3 magnification = detdist/sampos
print,magnification, ' magnification'

;colloid definitions r0=2.8179d-15 ; classical electron radius
in meter Rc = 40d-9 ; diameter of colloid in meter rohel =
4.6531d30 ; electron density in e-/m^3 (Au=4.653d27) rohmass =
19.3D ; mass density in kg/m^3 ;parameters for random walk numem =
3; amount of colloids nsteps =5 ; number of hops in ramdom walk kb
= 1.3806d-23 ; boltzmann constant [J/K] T = 293.15D ;
temperature [kelvin] mu = 1.0019d-3 ; viscosity of water [Pa*s] Dc
= 1D/6D*(kb*T/(!DPI*mu*Rc)) ; Diffusion constant of colloid mass =
```

```
rohmass * 4/3 *!DPI * Rc^3 ; mass of colloid vmean
=sqrt(kb*T/mass) ;mean velocity of colloid hopdist=2*Dc/vmean
;calculate hop distance from values above ;nsteps =
fix(vmean/(acctime*hopdist)) print, hopdist, ' hopdist' print,
mass, ' mass' print, dc, ' dc'

;init structures Q = {$
  lambda : (12.39D/Energy)*10D^(-10D)      ,$ ; wavelength
  x : DINDGEN(numem)      ,$ ; x-Koordinaten der Quellpunkte
  indexstepx : DINDGEN(numem) ,$; indexkoord in x
  y : DINDGEN(numem)      ,$ ; y-Koordinaten der Quellpunkte
  indexstepy : DINDGEN(numem) ,$; indexkoord in y
  F : OD      ,$ ; contrast of individual colloid
  N : numem      ,$ ; number of emitters
  w : width      $; width of gaussian for convolution at detector
}
Q.x[0]=5d-8 ;coordinates of colloid 1 Q.y[0]=0 Q.x[1]=-5d-8
;coordinates of colloid 2 in meter Q.y[1]=-5d-8 Q.x[2]=-5d-8
;coordinates of colloid 3 in meter Q.y[2]=5d-8 ;Q.x[3]=3d-8
;coordinates of colloid 4 in meter ;Q.y[3]=3d-8

; frame for display D = {$
  z : detdist*magnification      ,$ ; effective distance detector sample
  x : DINDGEN(Dx)      ,$ ; x-Koordinaten der Quellpunkte
  y : DINDGEN(Dy)      ,$ ; y-Koordinaten der Quellpunkte
  E : DCOMPLEXARR(Dx,Dy)      ,$ ; anfängliches E-Feld at detector
  magnification: magnification      ,$; guess what ....
  IE : Dcomplexarr(Dx,Dy)      $
}

;initialize detector size for i=0L, DX-1 do begin
  D.x[i]=-(disx)/2+i*(disx/Dx)
  D.y[i]=-(disy)/2+i*(disy/Dy)
endfor
```

```

;big frame for saving field bigness=1.3 ; how big is big .... DC =
{$
  z : detdist*magnification  ,$ ; effective distance detector sample
  x : DINDGEN((bigness*Dx))      ,$ ; x-Koordinaten der Quellpunkte
  y : DINDGEN((bigness*Dy))      ,$ ; y-Koordinaten der Quellpunkte
  E : DCOMPLEXARR(bigness*Dx,bigness*Dy)  ,$ ; anfängliches E-Feld at detector
  PW : Dcomplexarr(bigness*Dx,bigness*Dy)  ,$ ;plane wave
  G : Dindgen(bigness*Dx,bigness*Dy)      $ ;gaussian
}

for i=0L, (bigness*DX)-1 do begin
  DC.x[i]=-(bigness*disx)/2+i*((disx)/Dx)
  DC.y[i]=-(bigness*disy)/2+i*((disy)/Dy)
endfor

temp=dindgen(Dx,Dy,nsteps+1) int=dindgen(DX,DY)

;define constrast for colloids
Q.F=-((rohel*r0/samos)*(4/3*!DPI*Rc^3)) print,q.f,' contrast' ;
calculate coherent interference at detector calc_field

for j=0, nsteps do begin print, 'starting random walk ....'
read_field rand_walk, 1e-8 ; random walk the colloid positions
with <R> in meter as argument temp[*,*,j]=D.IE ; store each hop
for later superposition
;temp[*,*,j]=(abs(D.IE[*,*])^2/max(abs(D.Ie)^2)) ; store each hop
for later superposition print, nsteps-j , ' hops left...' endfor

if nsteps+1 GT 1 then int=total(temp,3) else int=temp ;incoherent
superposition for colloids in each step

;add noise

int=abs(int)^2 int=int/max(int) temp=int

;for seriesfile=0L, 5 do begin acctime=50 FOR

```

```
j=0L,N_ELEMENTS(int)-1 DO
temp[j]=RANDOMN(seed,POISSON=(acctime)*1.0*int[j])

print,'... finished!!'

;init fitting ;estimates=DINDGEN(4) ;estimates[0]=300 ;height of
gaussian ;estimates[1]=0 ; center of gaussian ;estimates[2]=200
;width of gaussian ;estimates[3]=0 ;constant offset

;display and saving .... window,0,xsize=512,ysize=512,
title='Detector Intensity' tvscl, congrid(Int,!d.x_size,!d.y_size)
xkoord=float(q.indexstepx)/(n_elements(d.x))
ykoord=float(q.indexstepy)/(n_elements(d.y)) xyouts,
0.5-xkoord,0.5-ykoord,'*',color=250,alignment=0.5,/normal
WRITE_TIFF,'intensity4colls.tiff',CONGRID(BYTSCL((Int[250:750,250:750]),min=0),DX,DY)

window, 1,xsize=512,ysize=512, title='cut through frame'
intplot=total(temp[200:800,fix(n_elements(D.x)/2)-1:fix(n_elements(D.x)/2)+1],2)
plot, intplot,yrange=[0,max(intplot)*1.1]

;fitresult=gaussfit(D.x[200:800],intplot,coeff,nterms=4) ;plot,
fitresult,yrange=[0,max(intplot)*1.1],/noerase, color=250

;window, 2,xsize=512,ysize=512, title='devide by fit' ;plot,
intplot/fitresult, color=255 seriesfile=acctime ;save data
filename='i:\uni\rand_holo\data\cut4colls'+STRTRIM(string(seriesfile),2)+' .dat'
;filename='D:\uni\rand_holo\data\cut'+0'+ .dat'

OPENW,out,filename,/get_lun
for j=0L, n_elements(intplot)-1 do begin
printf,out,intplot[j]
endfor
close,out
free_lun,out

;endfor end
```

```

pro rand_walk , step common parameters

for i=0, Q.N-1 do begin

randnum=fix(randomu(seed)*8) case randnum of 0: Q.x[i]=Q.x[i]+step
1: Q.y[i]=Q.y[i]+step/2 1: Q.x[i]=Q.x[i]+step/2 2:
Q.y[i]=Q.y[i]+step 3: Q.y[i]=Q.y[i]+step/2 3: Q.x[i]=Q.x[i]-step/2
4: Q.x[i]=Q.x[i]-step 5: Q.y[i]=Q.y[i]-step/2 5:
Q.x[i]=Q.x[i]-step/2 6: Q.y[i]=Q.y[i]-step 7: Q.y[i]=Q.y[i]-step/2
7: Q.x[i]=Q.x[i]+step/2 endcase

endfor

end

; read in fields from file and ; do coherent interference of all
colloids pro read_field common Parameters

temp1=dcomplexarr(n_elements(DC.x),n_elements(DC.y))
temp2=dcomplexarr(n_elements(DC.x),n_elements(DC.y))
temp3=dindgen(n_elements(DC.x),n_elements(DC.y))

;read in field OPENR,in,'field',/get_lun,/xdr readu,in,temp1
readu,in,temp2 readu,in,temp3 close,in free_lun,in

; set values DC.E=temp1 DC.PW=temp2 DC.G=temp3

;shifting of fieldpattern corresponding to emitter position ;first
calculate center indices
dcxs=fix((n_elements(DC.x)-n_elements(D.x))/2)
dcxe=n_elements(DC.x)-fix((n_elements(DC.x)-n_elements(D.x))/2)-1
dcys=fix((n_elements(DC.y)-n_elements(D.y))/2)
dcye=n_elements(DC.y)-fix((n_elements(DC.y)-n_elements(D.y))/2)-1

;calculate step xstepsize=abs(D.x[0]-D.x[1])
ystepsize=abs(D.y[0]-D.y[1])

```

```
;add zoneplate pattern for each colloid at its position
D.E[*]=complex(0,0) for i=0L, Q.N-1 do begin ;calculate step in
index from step in meter
Q.indexstepx[i]=fix(Q.x[i]*D.magnification / xstepsize)
Q.indexstepy[i]=fix(Q.y[i]*D.magnification / ystepsize)

;add up all scatterers coherently ; with their respective position
D.E[*,*]+=DC.E[(dcxs+q.indexstepx[i]):(dcxe+q.indexstepx[i]),(dcys+q.indexstepy[i]):
endfor

;add plane wave with gaussian shaped amplitude ; gaussian position
stays put D.IE+=D.E+DC.PW[dcxs:dcxe,dcys:dcye]

end
```

```
PRO calc_field
COMMON Parameters
PRINT, 'Starting field calculation ...'
startzeit = SYSTIME(1)

Im = DCOMPLEX(0,1)
; Wellenzahl
k = 2D*!DPI/Q.lambda

; calculate all points on detector
For j=0L, n_elements(DC.y)-1 Do Begin

R1 = 0.5*((DC.x[*])^2+(DC.y[j])^2)/DC.z ;small angle approx.
;calculate field on detector
DC.E[* ,j] = Q.F * EXP(Im * k * R1)
;fill matrix to convolute gaussian later
DC.G[* ,j] = exp(-(DC.x[*]^2+DC.y[j]^2)/Q.w^2)
Endfor
```

```
DC.G=DC.G/max(DC.G)    ; normalize
DC.PW[*]=dc.g*exp(Im*!DPI) ;plane wave

; some cosmetics ...
endzeit = SYSTIME(1)
PRINT, endzeit-startzeit, ' sec needed for calculation'
PRINT, 'single particle field ready...'
```



```
;save data to use pattern again for several colloids
OPENW,out,'field',/get_lun,/xdr

writeu,out,DC.E
writeu,out,DC.PW
writeu,out,DC.G

close,out
free_lun,out
```



```
END
```

BIBLIOGRAPHY

Bibliography

- [ANM00] Jens Als-Nielsen and Des McMorrow. *Elements of modern x-ray physics*. Wiley, 2000.
- [BDD⁺02] J. H. H. Bongaerts, C. David, M. Drakopoulos, M. J. Zwanenburg, G. H. Wegdam, T. Lackner, H. Keymeulen, and J.F. van der Veen. Propagation of partially coherent focused x-ray beam within a planar x-ray waveguide. *Journal of Synchrotron Radiation*, 9:383–393, 2002.
- [BKvdV03] C. Bergemann, H. Keymeulen, and J. F. van der Veen. Focusing x-ray beam to nanometer dimensions. *Physical Review Letters*, 2003.
- [CBL⁺05] W. Chao, B.D.Harteneck, J. A. Liddle, E. H. Anderson, and D. T. Attwood. Soft x-ray microscopy at a spatial resolution better than 15nm. *Nature*, 435:1210–1213, 2005.
- [cyb] Oxford danfysik. <http://www.oxford-danfysik.com>.
- [DEH⁺04] R.B. Doak, Y. Ekinici, B. Holst, J. P. Toennies, T. Al-Kassab, and A. Heinrich. Filed ionization detection of superionic molecular beams. *Review of Scientific Instruments*, 75:405–414, 2004.
- [Egg02] Tobias Eggert. Der ketek silizium drift detektor - Grundlagen, Anwendungen, Funktionsprinzip. Ketek GmbH, 2002.
- [ELS⁺04] S. Eisebitt, J. Luning, W.F. Schlotter, M. Lorgen, O. Hellwig, W. Eberhardt, and J. Stohr. Lensless imaging of magnetic nanostructures by x-ray spectro-holography. *Nature*, 432(7019):885–8, 2004.
- [FBM04] P. Falus, M. A. Borthwick, and S. G. J. Mochrie. Fast ccd for x-ray correlation spectroscopy and time-resolved x-ray scattering and imaging. *Review of scientific Instruments*, 75(11), 2004.

- [FEI] FEI Company, Hillsboro, OR, USA. *Nova 600 NanoLab, Product data.* www.feicompany.com.
- [Fie78] J. Fienup. Reconstruction of an object from the modulus of its fourier transform. *Optics Letters*, 3(1):27, 1978.
- [Föl92] Otto Föllinger. *Regelungstechnik*. Hüthig, 1992.
- [FOKS06] C. Fuhse, C. Ollinger, S. Kalbfleisch, and T. Salditt. Coherent propagation of white x-rays in a planar waveguide. *Journal of synchrotron radiation*, 13:69–73, 2006.
- [FOOM96] J. Fujita, Y. Ohnishi, Y. Ochiai, and S. Matsui. Ultrahigh resolution of calixarene negative resist in electron beam lithography. *Applied Physics Letters*, 68:1297, 1996.
- [FS06] C. Fuhse and T. Salditt. Finite-difference field calculations for two dimensionally confined x-ray waveguides. *Applied Optics*, accepted, 2006.
- [Fuh06] Christian Fuhse. *X-ray waveguides and waveguide based lensless imaging*. PhD thesis, Georg-August-Universität, Göttingen, 2006.
- [Gab48] D. Gabor. A new microscopic principle. *Nature*, 161, 1948.
- [HAMX97] T. Hicks, P. Atherton, M. McConnell, and Y. Xu. *The Nanopositioning Book*. Queensgate Instruments, 1997.
- [Han] ID22 Beamline Handbook. Id22 beamline handbook. <http://www.esrf.fr/UsersAndScience/Experiments/Imaging/ID22/BeamlineHandbook/>.
- [HCRM05] O. Hignette, P. Cloetens, G. Roasting, and C. Morawe. Efficient sub 100nm focussing of hard x-rays. *Review of Scientific Instruments*, 76:063709, 2005.
- [HGD93] B.L. Henke, E.M. Gullikson, and J.C. Davis. X-ray interactions: photoabsorption, scattering, transmission, and reflection at e=50-30000 ev, z=1-92. *Atomic Data and Nuclear Data Tables*, 54(2):181–342, 1993.
- [HRC⁺01] O. Hignette, G. Roasting, P. Cloetens, A. Rommeveaux, and A. Freund. Submicron focussing of hard x-rays with reflecting surfaces at the esrf. *Proceedings of SPIE*, 4499:105–116, 2001.

- [Ins] Princeton Instruments. Princeton instruments.
<http://www.piacton.com>.
- [Jar05] Ansgar Jarre. *Hard x-ray waveguide optics*. PhD thesis, Georg-August-Universität Göttingen, 2005.
- [JFO⁺05] A. Jarre, C. Fuhse, C. Ollinger, J. Seeger, R. Tucoulou, and T. Salditt. Two-dimensional hard x-ray beam compression by combined focussing and waveguide optics. *Physical Review Letters*, 94:074801, 2005.
- [LCC⁺97a] S. Lagomarsino, A. Cedola, P. Cloetens, S. di Fonzo, W. Jark, G. Soullié, and C. Riekel. Phase contrast hard x-ray microscopy with submicron resolution. *Applied Physical Letters*, 71:2557–2559, 1997.
- [LCC⁺97b] S. Largomarsino, A. Cedola, P. Cloetens, S. di Fonzo, W. Jark, G. Soullié, and C. Riekel. Phase contrast hard x-ray microscopy with submicron resolution. *Applied Physical Letters*, 71(18):2557–2559, 1997.
- [Lei] Leica, Jena. *LEICA LION-LV1*.
- [Lin] SuSe Linux. Suse linux. <http://de.opensuse.org/>.
- [LK03] W. Lauterborn and T. Kurz. *Coherent Optics*. Springer, 2003.
- [LLT95] S. Lipson, H. Lipson, and D. Tannhauser. *Optik*. Springer, 1995.
- [LU62] E.M. Leith and J. Upatnieks. Reconstructed wavefronts and communication theory. *Journal of the optical society of america*, 52:1123–1130, 1962.
- [Mar74] D. Marcuse. *Theory of dielectric optical waveguides*. Academic Press, New York, 1974.
- [MCKS99] J. Miao, P. Charalambous, J. Kirz, and D. Sayre. Extending the methodology of x-ray crystallography to allow imaging of micrometre-sized non-crystalline specimens. *Nature*, 400:342, 1999.
- [MIAH03] J. Miao, T. Ishikawa, E. Anderson, and K. Hodgson. Phase retrieval of diffraction patterns from noncrystalline samples using the oversampling method. *Physical Review B*, 67:174104, 2003.

- [Mic86] Alan G. Michette. *Optical Systemas for soft x-rays*. Plenum Press, New York, 1986.
- [MIJ⁺02] J. Miao, T. Ishikawa, B. Johnson, E. Anderson, B. Lai, and K. Hodgson. High resolution 3d x-ray diffraction microscopy. *Physical Review Letters*, 89(8):088303, 2002.
- [MOF⁺04] M.C.Rheinstaedter, C. Ollinger, G. Fragneto, F. Demmel, and T.Salditt. Collective dynamics in phospholipid bilyaers investigated by inelastic neutron scattering: Exploring the dynamics of biological membranes with neutrons. *Physical Review Letters*, 93:108107, 2004.
- [OFJS05] C. Ollinger, C. Fuhse, A. Jarre, and T. Salditt. Two dimensional x-ray waveguides on a grating. *Physica B*, 357, 2005.
- [OFKS06] C. Ollinger, C. Fuhse, S. Kalbfleisch, and T. Salditt. Object localization with 10 nm accuracy by x-ray phase contrast projection imaging. *in preparation*, 2006.
- [OFS05] C. Ollinger, C. Fuhse, and T. Salditt. Application of the fox2d cu inf12p focusing optics on a white beam synchrotron beamline. *www.xenocs.com*, 2005.
- [PDB⁺02] F. Pfeiffer, C. David, M. Burghammer, C. Riekel, and T. Salditt. Two dimensional x-ray waveguides and point sources. *Science*, 297(5579):230–234, 2002.
- [Peu00] M. Peuker. *Elektronenstrahlithographie und Nanostrukturübertragung zur Herstellung von hochauflösenden diffraktiven Röntgenoptiken aus Nickel*. PhD thesis, Georg-August-Universität Göttingen, 2000.
- [PJB⁺05] M. Puolsen, F. Jensen, O. Bunk, R. Feidenhans'l, and D. W. Breiby. Silicon waveguides produced by wafer bonding. *Applied Physics Letters*, 87:261904, 2005.
- [PMS02] F. Pfeiffer, U. Mennicke, and T. Salditt. Waveguide-enhanced scattering from thin biomolecular films. *Journal of applied crystallography*, 35:163–167, 2002.

- [See04] Jens Seeger. Nanolithographische herstellung von 2d-wellenleitern für harte röntgenstrahlung. Master's thesis, Georg-August-University Göttingen, 2004.
- [SJe02] J. Susini, D. Joyeux, and F. Polack (eds.). X-ray microscopy. *Proceedings of the 7th International Conference on X-ray microscopy*, 2002.
- [SKP⁺05] C.G. Schroer, O. Kurapove, J. Patommel, P. Boye, J. Feldkamp, B. Lengeler, M. Burghammer, C. Riekel, L. Vincze, A. Van der Hart, and M. Küchler. Hard x-ray nanoprobe based on refractive x-ray lenses. *Applied Physics Letters*, 87:124103, 2005.
- [SKSL96] A. Snigirev, V. Kohn, I. Snigireva, and B. Lengler. A compound refractive lens for focusing high-energy x-rays. *Nature*, 385:49–51, 1996.
- [Sou] Sourceforge. Sourceforge. <http://sourceforge.net/>.
- [SS73] E. Spiller and A. Segmüller. Propagation of x-rays in waveguides. *Applied Physical Letters*, 24:60–61, 1973.
- [Wei02] Timm Weitkamp. *Imaging and Tomography with high Resolution using coherent hard Synchrotron Radiation*. PhD thesis, Universität Hamburg, 2002.
- [WPVR03] G. Williams, M. Pfeifer, I. Vartanyants, and I. Robinson. Three-dimensional imaging of microstructure in au nanocrystals. *Physical Review Letters*, 90(17):175501, 2003.
- [YPV95] Y.V.Kopylov, A. V. Popov, and A.V. Vinogradov. Application of the parabolic wave equation to x-ray diffraction optics. *Optics Communications*, 118(619), 1995.

Acknowledgements

In concluding this thesis, i would like to thank my PhD advisor, my colleagues and my parents for help and continuous support throughout the entire three years.

First of all, i thank my PhD advisor Prof. Tim Salditt for proposing this rewarding and interesting topic. I very much enjoyed the nice atmosphere at the institute, the exciting beamtimes and the confidence he had in me, while building the MoWaSt instrument.

All members of the 'waveguide team', namely Christian Fuhse, Ansgar Jarre, Sebastian Kalbfleisch, Jens Seeger and all group members whom i acknowledge for the excellent teamwork during the numerous beamtimes and in the institute. Special thanks to Christian Fuhse. From his analytical and computational skills this thesis profited enormously. Also, i like to thank Christian Fuhse, Ansgar Jarre and Hauke Schollmeyer for proofreading the thesis.

For a lot of help and advice in programming, i like to thank Tim-Oliver Husser.

I had the pleasure to work with Hans Düben, Thorsten Gronemann, Joachim Herbst, Peter Nieschalk and Jens Wegener. Without their technical assistance it would not have been possible to build the instrument and perform the experiments.

The members of the Institut für Materialphysik, namely Peter-Joachim Wilbrandt for advice in the focused ion beam technique and Talaát al-Kassab for providing the tungsten tips.

During the beamtimes at European Synchrotron Radiation Facility (ESRF), the Berliner Elektronen Synchrotron (BESSY) and the Hamburger Synchrotron-

strahlungslabor (HASYLAB) we were excellently supported by various people, namely Remi Tucoulou (ID22, ESRF), Norbert Schell (ROBL, ESRF), Anders Madsen and Andrei Fluerasu (ID10A, ESRF), Hermann Franz (HASYLAB) and Ullrich Prietsch, Wolfram Leitenberger and Yves Bodenthien (EDR, BESSY).

Anja Strobach möchte ich ganz herzlich dafür danken, dass sie, insbesondere in der Zeit des Zusammenschreibens, immer für mich da war.

Zum Abschluss geht mein Dank natürlich an meine Eltern. Sie haben mir das Studium ermöglicht und mich insbesondere in schwierigen Zeiten immer wieder aufgebaut.

List of Publications

- T. SALDITT, C. MÜNSTER, U. MENNICKE, C. OLLINGER and G. FRAGNETO
Thermal Fluctuations of Oriented Lipid Membranes by Nonspecular Neutron Reflectometry,
Langmuir 19, 7703 (2003).
- M. RHEINSTÄDTER, C. OLLINGER, G. FRAGNETO and T. SALDITT
Collective dynamics in phospholipid bilayers investigated by inelastic neutron scattering: Exploring the dynamics of biological membranes with neutrons,
Physica B 350, 136 (2004).
- M.C. RHEINSTÄDTER, C. OLLINGER, G. FRAGNETO, F. DEMMEL, T. SALDITT
Collective Dynamics of Lipid Membranes Studied by Inelastic Neutron Scattering
Physical Review Letters 93, 108107 (2004).
- C. FUHSE, A. JARRE, C. OLLINGER, J. SEEGER, T. SALDITT and R. TUCOULOU
Front-coupling of a prefocused x-ray beam into a monomodal planar waveguide,
Applied Physics Letters 85, 1907 (2004).
- A. JARRE, C. FUHSE, C. OLLINGER, J. SEEGER, R. TUCOULOU and T. SALDITT
Two-dimensional hard X-ray beam compression by combined focusing and waveguide optics,
Physical Review Letters 94, 074801 (2005).

- C. OLLINGER, C. FUHSE, A. JARRE and T. SALDITT
Two dimensional X-ray waveguides on a grating,
Physica B 94, 53 (2005).
- C. OLLINGER, D. CONSTANTIN, J. SEEGER and T. SALDITT
Lipid membranes on a surface grating studied by neutron reflectivity,
Europhysics Letters 71 (2), 311 (2005).
- D. CONSTANTIN, C. OLLINGER, M. VOGEL and T. SALDITT
Electric field unbinding of solid-supported lipid multilayers,
European Physical Journal E 18, 273 (2005).
- C. FUHSE, C. OLLINGER, S. KALBFLEISCH and T. SALDITT
Coherent propagation of white X-rays in a planar waveguide ,
Journal of Synchrotron Radiation 13, 69 (2006).
- C. OLLINGER, C. FUHSE, S. KALBFLEISCH and T. SALDITT
*Object localization with 10nm accuracy by x-ray phase contrast projection
imaging ,*
in preparation .
- C. FUHSE, C. OLLINGER, S. KALBFLEISCH and T. SALDITT
X-Ray Holography ,
in preparation.
- A. JARRE, J. SEEGER, C. OLLINGER, C. FUHSE, C. DAVID and T. SALDITT
X-ray Waveguide Nanostructures - Design, Fabrication and Characterization
in preparation
- N. SCHELL, F. EICHHORN, A. BJEUMIKHOV, H. PRINZ and C. OLLINGER
*Parabolic capillary optics with 50 μ m focus and large focal distance for syn-
chrotron radiation scattering*
in preparation
- C. OLLINGER and T. SALDITT
A waveguide based lensless x-ray microscope
in preparation

Lebenslauf

Name: CHRISTOPH GERMAN JOSEF OLLINGER

Stattsangehörigkeit: deutsch

Geboren in Dillingen (Saar), am 14. April 1976.

1982 - 1986 Grundschule Odilienschule, Dillingen

1986 - 1995 Albert-Schweitzer-Gymnasium, Dillingen

1995 - 1996 Zivildienst
(Regionalstelle für kirchliche Jugendarbeit, Dillingen)

1996 - 2003 Universität des Saarlandes, Saarbrücken
(*Diplom* in Physik)

2003 - 2006 Georg August Universität, Göttingen